# Interdimensional effects in systems of fermions

A Thesis Submitted to the
College of Graduate and Postdoctoral Studies
in Partial Fulfillment of the Requirements
for the degree of Doctor of Philosophy
in the Department of Physics and Engineering Physics
University of Saskatchewan
Saskatoon

By
Adam Zulkoskey

# Permission to Use

In presenting this thesis in partial fulfilment of the requirements for a Postgraduate degree from the University of Saskatchewan, I agree that the Libraries of this University may make it freely available for inspection. I further agree that permission for copying of this thesis in any manner, in whole or in part, for scholarly purposes may be granted by the professor or professors who supervised my thesis work or, in their absence, by the Head of the Department or the Dean of the College in which my thesis work was done. It is understood that any copying or publication or use of this thesis or parts thereof for financial gain shall not be allowed without my written permission. It is also understood that due recognition shall be given to me and to the University of Saskatchewan in any scholarly use which may be made of any material in my thesis.

Requests for permission to copy or to make other use of material in this thesis in whole or part should be addressed to:

Head of the Department of Physics and Engineering Physics
116 Science Place
University of Saskatchewan
Saskatoon, Saskatchewan
Canada
S7N 5E2

Or

Dean
College of Graduate and Postdoctoral Studies
University of Saskatchewan
116 Thorvaldson Building, 110 Science Place
Saskatoon, Saskatchewan S7N 5C9
Canada

# Abstract

Over the past decade, new materials have been theoretically predicted and experimentally verified which are favourable candidates in the field of spintronics. These materials include topological insulators, graphene, and heterostructure materials with large Rashba spin-orbit coupling along an interface. In all of these materials, the electron's spin is responsible for exotic behaviour along either a surface or an interface. Interdimensional models have previously been used to analyze systems which contain low-dimensional substructures which affect the propagation properties of particles. In the case of a thin interface which affects propagation properties through a change in effective mass, and two-dimensional quantum well, analytic models allow for the calculation of the density of states inside the low-dimensional substructure. The density of states describes the availability of charge carriers in a given material, and is a fundamental quantity used to derive many other thermodynamic quantities of interest. Our principal focus is to extend the use of interdimensional models to study materials favourable for spintronics, and calculate analytic density of states for particles inside the low-dimensional substructure. We have analyzed nonrelativistic interdimensional models with Rashba spin-orbit coupling along an interface. We have extended these interdimensional models with the addition of a change in effective mass as well as attractive potential terms for motion in the interface. Topological crystalline insulators host linearly dispersing topological surface states, and present a system to construct a first quasirelativistic interdimensional fermion model. We have calculated the density of states at the location of the interface analytically in all models except the Rashba spin-orbit coupling plus effective mass system, in which numerical techniques are used. We report that in all systems with an effective mass term in the interface, the density of states has three-dimensional behaviour for low-energies transitioning to two-dimensional behaviour for high energies. Interdimensional models with Rashba spin-orbit coupling along the interface host both free and bound states contributions to the density of states. Bound states contribute terms proportional to the free two-dimensional density of states and free states contribute terms proportional to the free three-dimensional density of states. We have used experimental values from Bi/Ag heterostructure systems for our Rashba spin-orbit coupling models and PbTe in our quasirel-

ativistic fermion model.

# Acknowledgements

I would like to express my sincere gratitude to my supervisors Rainer Dick and Kaori Tanaka. They have provided me with support and very helpful discussions during my research. I am very thankful to both of them for helping me become the student and researcher I am today. I would also like to thank my committee members Masoud Ghezelbash, Michael Bradley, Andrew Grosvenor, Jacek Szmigielski and Glen Hussey for their assistance. Finally I would like to thank my family and friends for their love and support, and especially my wife Joelle. She is the perfect partner in my academic journey, and gives me all of the motivation I need to succeed.

*For my love, Joelle.*

# Contents

# List of Figures

# List of Abbreviations

| | |
|---|---|
| RSOC | Rashba spin-orbit coupling |
| TMDC | Transition metal dichalcogenide |
| EE | Edelstein effect |
| IEE | Inverse Edelstein effect |
| SIA | Structure inversion asymmetry |
| BIA | Bulk inversion asymmetry |

# 1 Introduction

## 1.1 Topological Insulators

Condensed matter physics has received a significant amount of interest over the last decade due to the discovery of a new type of phase transition in materials that are topological in nature. Topological insulators exhibit topologically non-trivial gapless surface states that originate from gapped bulk states [1]. In the case of topological insulators, these gapless surface states occur due to a combination of spin-orbit coupling and time-reversal symmetry [1]. Pioneering work in this area was first conducted using two-dimensional materials such as graphene [1, 2] and HgTe/CdTe quantum well structures [3]. The particular area of interest for our research comes from three-dimensional materials that exhibit bulk fully gapped states, with topologically non-trivial, gapless surface states.

The three-dimensional topological insulator is described by the existence of four $Z_2$ topological invariants [4, 5, 6, 1]. In the Brillouin zone for the surface of a three-dimensional crystal structure there are four time-reversal invariant points [1]. If there are surface states present at these points then from Kramer's theorem these points must be doubly degenerate [1]. The Kramer's degenerate points form Dirac points where the bottom of the valence band touches the top of the conduction band [1]. Depending on how the four distinct Dirac points connect to each other, the system may be a trivial insulator or a three-dimensional topological insulator. If two time-reversal invariant momenta, occuring at the Dirac points, cross the Fermi energy an odd number of times, then the surface states are topologically protected and gapless with spin-filtered Dirac-like dispersion relations connecting the conduction band and the valence band. Therefore for an odd number of crossings of the Fermi energy, the edge states are examples of the quantum spin-Hall phase [1, 4]. If the edge states cross the

Fermi energy an even number of times, then the system is not topologically protected and is in the trivial insulating phase [4]. The distinction between these two cases is determined by the four $Z_2$ topological invariants of the system [1]. There are two types of three-dimensional topological insulators. The first that is characterized by the $Z_2$ topological invariant $\nu_0 = 0$ is a weak topological insulator. The weak topological insulator is a system that is created by stacking layers of two-dimensional quantum spin-Hall insulators. However, unlike the strictly two-dimensional case of the quantum spin-Hall insulator, i.e., a single-layer of the weak topological insulator, the helical edge states in the layered system are not protected by time-reversal symmetry [1]. The second type of three-dimensional topological insulator is termed a strong topological insulator and is associated with a $Z_2$ topological invariant $\nu_0 = 1$. This system is distinctly different from a two-dimensional topological insulating state. The $\nu_0$ value determines whether the Fermi surface encloses an even or odd number of Dirac points [1]. An even number of enclosed Dirac points is associated with a weak topological insulator, while an odd number of enclosed Dirac points is associated with a strong topological insulator. Reference [4] used a slab geometry to calculate the band structure of both weak and strong topological insulators in order to show the number of Dirac points present in each case. The edge states present in a strong topological insulator form a new type of topological metal [1, 4]. In this new metallic state, the edge states are not spin degenerate [1]. This can occur because the Dirac point partners, namely the Dirac points of opposite spin, reside on opposite surfaces [4]. The strong topological insulator is robust against weak disorder and thus cannot be localized. This is a consequence of the electron having the Berry phase of $\pi$ upon circling along the Fermi surface. Experimentally, the three-dimensional topological insulator has been realized in the semiconducting alloy $Bi_{1-x}Sb_x$ by exploring topological insulators using angle-resolved photoemission spectroscopy (ARPES) experiments [1, 7]. A second generation of three-dimensional topological insulators was discovered in the materials $Bi_2Sb_3$, $Bi_2Te_3$ and $Sb_2Te_3$ [1]. The discovery of these materials had been motivated by the search for $Bi_{1-x}Sb_x$ [1].

A different type of topological insulator termed a topological crystalline insulator is characterized by having crystal point symmetry and time-reversal symmetry which make the

edge states of the sample topologically protected [8]. These topological insulators are three-dimensional and are considered to be a counterpart to topological insulators without spin-orbit coupling [8]. Topological crystalline insulators cannot be smoothly connected to a trivial insulator when time-reversal and crystal symmetries exist. In order for the crystal symmetry to be protected, the crystal structure must be symmetric upon rotational symmetry on the surfaces that contain the edge states. In Ref. [8], crystal structures that have fourfold $C_4$ and sixfold $C_6$ rotational symmetry as well as time-reversal symmetry were studied. It is shown that a new $Z_2$ topological invariant defines the topological nature of a system with time-reversal invariant band structures with $C_4$ or $C_6$ rotational symmetry [8]. The surface states traverse the band gap and are four-fold degenerate [8]. Similarly to the strong topological insulator, a $Z_2$ topological invariant of $\nu_0 = 1$ characterizes the topological crystalline insulator with gapless surface states [8]. Shortly after the theoretical prediction of the topological crystalline insulator came the first theoretical prediction of a material that could exist as a topological crystalline insulator [9]. The material studied in Ref. [9] was SnTe. SnTe contains an even number of Dirac cones on its high symmetry crystal surfaces which lead to metallic-like surface states which are topologically protected from disorder by crystal symmetry. Reference [9] compares the two insulators SnTe and PbTe, showing that when crystal symmetry is present there exists a mirror Chern number that is topologically invariant and characterizes the topological crystalline insulator. It has been shown in Ref. [9] that because SnTe has an inverted band structure at its fundamental band gaps which are located at four equivalent $L$ points in the face-centered-cubic Brillouin zone, it is topologically non-trivial. PbTe on the other hand has a band structure that can be smoothly connected to a trivial insulator. This explains the band inversion in the material $Pb_{1-x}Sn_xTe$ where for increasing $x$, the conduction and valence bands become inverted at the $L$ points in the band structure.

In 2010, Svane *et al.* calculated the electronic band structures of the compounds PbS, PbSe and PbTe [10]. It has been found [10] that a pressure-induced gap closure between the lowest point of the conduction band and the highest point of the valence band leads to the presence of three-dimensional Dirac points with linear dispersion relations [10]. An

assumption made about these surface states is that they originate from massive Dirac bulk states. In 2013 this assumption was verified using the compound $Pb_{1-x}Sn_xTe$ [11] where the bulk states were indeed found to be massive Dirac states in the bulk. In 2014, samples of $Pb_{1-x}Sn_xTe(111)$ were grown as thin films and it has been shown that by increasing the ratio of Sn/Pb the films undergo a topological phase transition between a trivial insulator and a topological crystalline insulator [12]. They observed an even number of Dirac cones at distinct time-reversal invariant momenta, which is a requirement for the topological crystalline insulator [13]. At a critical value of $x$ in $Pb_{1-x}Sn_xTe$ the band gap present in PbTe closes and re-opens as the amount of Sn is increased [12]. At this critical point the conduction and valence bands at the band gaps invert, which leads to a change in the topological invariant mirror Chern number characterizing the phase transition from trivial insulator to topological crystalline insulator [12]. The $Pb_{1-x}Sn_xTe(111)$ thin films contain non-trivial surface states with a Dirac-like dispersion for a low Sn/Pb ratio [12]. It was also found that by lowering the thickness of the film, a gap opens between coupled topological states on opposite surfaces [12]. Experimental and theoretical work has also been conducted on the topological crystalline insulator $Pb_{1-x}Sn_xSe$. It has been found that the Dirac points of the surface states originate from massive Dirac bulk states [11], and that by breaking the crystal symmetry present at these Dirac points, the Dirac fermions develop a mass [14]. Surface states have been experimentally found in $Pb_{1-x}Sn_xSe(111)$ films at the $\overline{\Gamma}$ and $\overline{M}$ points in the surface Brillouin zone [15]. Extensive efforts are now under way to determine how the surface structure of the topological crystalline insulators $Pb_{1-x}Sn_xSe$ is affected by other external parameters besides x such as temperature [16, 17] and crystal structure [17, 18].

## 1.2 Two-dimensional electron gas with Rashba spin-orbit coupling

Recent efforts have been put forth in the area of spintronics, which utilizes the spin degree of freedom for information storage and processing [19, 20]. Material candidates in the field of spintronics feature large RSOC, which induce novel properties (such as the Edelstein effect [21]) on surfaces or interfaces [22] where spin and charge conversion properties are important

[22, 23]. The Edelstein effect describes the conversion of charge current to spin current in which electrons are confined to a two-dimensional state [21]. This differs from the spin Hall effect which also describes the conversion of charge to spin current, which moves along the boundary of the material in the direction perpendicular to the charge current [23]. Rashba spin-orbit coupling (RSOC) effects are the result of bulk inversion asymmetry (BIA), e.g., in the zinc blende structure [24], as well as structure inversion asymmetry (SIA) i.e. lack of inversion symmetry in the confining potential, in semiconductors [25]. The Rashba spin-orbit interaction first analyzed in Ref. [25] for a two-dimensional electron gas arises from the nonrelativistic approximation of the Dirac equation [26]. The Hamiltonian and dispersion relation for a two-dimensional electron gas including RSOC is given by [25]

$$\begin{aligned} H &= \frac{\boldsymbol{p}_{\parallel}^2}{2m_*} + \alpha(\boldsymbol{\sigma} \times \boldsymbol{p}_{\parallel}/\hbar) \cdot \hat{z}, \\ E_{\pm}(k_{\parallel}) &= \frac{\hbar^2 k_{\parallel}^2}{2m_*} \pm \alpha|\boldsymbol{k}_{\parallel}|, \end{aligned} \tag{1.1}$$

where $\alpha = e\hbar E_z(z)/4m_*^2c^2$ is the Rashba coefficient, $E_z(z)$ is a uni-directional electric field, $\boldsymbol{\sigma} = (\sigma_x, \sigma_y, \sigma_z)$ are the Pauli matrices, $\boldsymbol{k}_{\parallel}$ is the two-dimensional wave vector with $\hat{z}$ the direction perpendicular to the electron gas [25, 26]. For an isotropic dispersion relation $E(k_{\parallel})$, the number of states per unit energy is given by [27]

$$\varrho(E) = \frac{1}{2\pi} \sum_{n,\sigma} \frac{k_{\parallel}(E)}{|dE_{n\sigma}/dk_{\parallel}|}. \tag{1.2}$$

The spin-split density of states using Eq. (1.1) are given by [27]

$$\begin{aligned} \varrho(E_{\pm}) &= \frac{m_*}{2\pi\hbar^2}\left(1 \mp \frac{\beta}{\sqrt{\beta^2 + 2Em_*/\hbar^2}}\right), E \geq 0, \\ \varrho(E_{-}) &= \frac{m_*\beta}{\pi\hbar^2\sqrt{\beta^2 + 2m_*E/\hbar^2}}, E < 0, \end{aligned} \tag{1.3}$$

where $\beta = m_*\alpha/\hbar^2$. The spin-split energy branches in Eq. (1.1) are displayed in Fig. 1.1. The purely two-dimensional electron gas with RSOC analyzed in Ref. [25] contains spin-split minima in the dispersion relation at wave vectors $\boldsymbol{k}_{min}$ where $|\boldsymbol{k}_{min}| = k_{min} = \alpha m_*/\hbar^2$. The negative energy density of states in Eq. (1.3) contains a van Hove singularity at $E_-(\boldsymbol{k}_{min}) = -\alpha^2 m_*/2\hbar^2$, where $dE_-/d\boldsymbol{k}_{\parallel} = 0$.

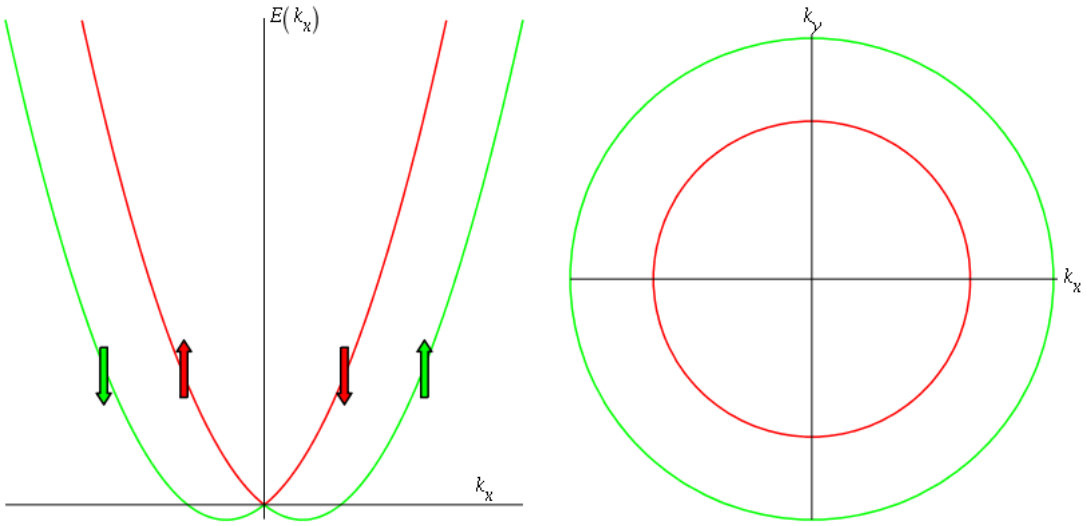


**Figure 1.1:** (Left) The spin-split bound dispersion relation for $k_y = 0$. The red(green) curve corresponds to $E_+(E_-)$ in Eq. (1.1) with a minimum energy of $E_{min} = -m_*\alpha^2/2\hbar^2$. (Right) The red(green) Fermi circles corresponding to $E_+(E_-)$ in Eq. (1.1). Up(down) arrows refer to +(-)y spin orientation

## 1.3 Edelstein and Inverse Edelstein effects on surfaces and interfaces

This section theoretically describes the Edelstein (EE) and inverse Edelstein (IEE) effect in two-dimensional systems with RSOC. However, the EE and IEE also exist on the surface of topological insulators and will be discussed in Sec. 1.4. The Edelstein effect [21] describes how an applied electric field $\boldsymbol{E}$ in the $x$-direction of a two-dimensional electron gas with SIA induces a net spin-polarization in the $y$-direction from electron motion. In the purely two-dimensional system with RSOC [25], Eq. (1.1) and Fig. 1.1 describe the spin-split energy branches for electrons with spin alignment $+y(-y)$ for $E_-(E_+)$, $k_x > 0$ and vice versa for $k_x < 0$ respectively. The effect of an applied electric field on electrons in a three-dimensional system is discussed in Ref. [28]. Newton's second law for a free electron in the presence of an electromagnetic field is given by,

$$\boldsymbol{F} = m\frac{d\boldsymbol{v}}{dt} = \hbar\frac{d\boldsymbol{k}}{dt} = -e\left(\boldsymbol{E} + \frac{1}{c}\boldsymbol{v}\times\boldsymbol{B}\right). \tag{1.4}$$

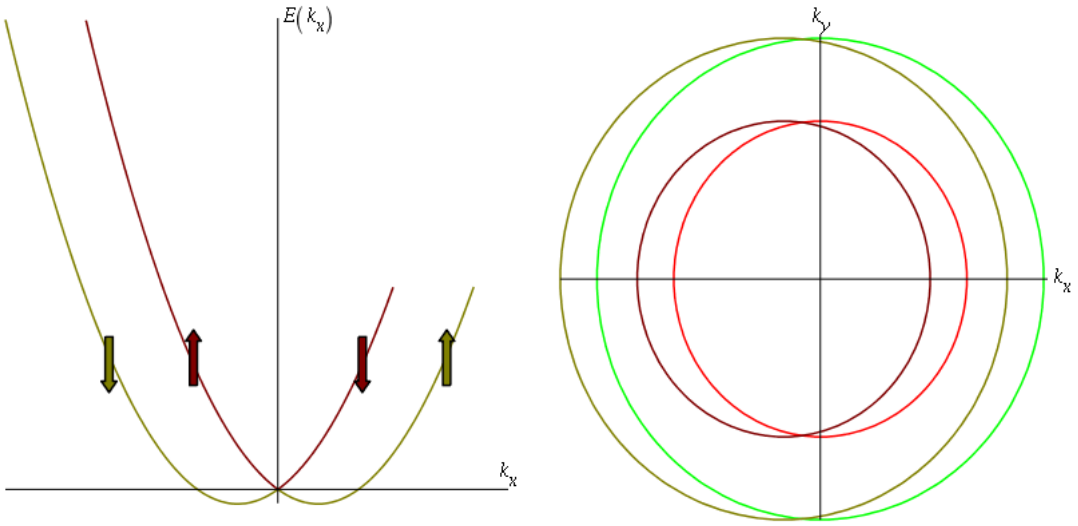


**Figure 1.2:** (Left) The spin-split bound state dispersion relation for $k_y = 0$ in the presence of an applied electric field $\boldsymbol{E} = \varepsilon\hat{x}$. The maroon(olive) curve corresponds to $E_+(E_-)$ in Eq. (1.1) with a minimum energy of $E_{min} = -m_*\alpha^2/2\hbar^2$ with adjusted populations of occupied states due to the EE. (Right) The red(green) Fermi circles corresponding to $E_+(E_-)$ in Eq. (1.1) and Fig. 1.1. The maroon(olive) Fermi circles correspond to the finite displacement due to the EE of the red(green) Fermi circles.

Using $\boldsymbol{B} = 0$ and ignoring the effects of collisions between electrons and either impurities or phonons, an electric field will shift the center of the Fermi sphere in $\boldsymbol{k}$ space by an amount $\delta\boldsymbol{k} = -e\boldsymbol{E}t/\hbar$ where $t$ is the that time the electric field has been active. This implies that every electron in the Fermi sphere has been shifted after time $t$ by an amount $\delta\boldsymbol{k}$. Introducing the effects of collisions with impurities or phonons restricts the size of the shift of the center of the Fermi sphere [28]. If the average time between collisions is $\tau$, a constant electric field will shift the Fermi sphere by an amount $\delta\boldsymbol{k} = -e\boldsymbol{E}\tau/\hbar$, leaving the electron gas in a steady state. In the two-dimensional electron gas with SIA, an applied electric field $\boldsymbol{E} = \varepsilon\hat{x}$, $\varepsilon > 0$ causes electrons to move in the $-x$-direction and populates states with $k_x < 0$ at the expense of states with $k_x > 0$. Figure 1.2 displays the spin-split energy branches in the presence of an electric field. In the steady-state, the center of the Fermi ciricle corresponding to the spin-split branches is shifted by $\delta k_x = -e\varepsilon\tau/\hbar$. The net effect of this changing population of occupied states is a net $-y$ spin polarization coming from the $E_-$ branch playing the major role [23].

The IEE is also possible in a two-dimensional electron gas with RSOC [23]. When a net

spin polarization is created in the two-dimensional system, e.g., through spin pumping [23], a charge current is induced [29]. In analogy with our discussion of the EE, when electrons with spin orientation $+y$ enter the two-dimensional system, the $E_+$ branch is overpopulated in the $k_x < 0$ region, while the $E_-$ branch is overpopulated in the $k_x > 0$ region. Due to the $E_-$ branch playing the major role [23], the net effect is a charge current in the $+x$-direction. The EE and IEE have been investigated in several systems with RSOC along a two-dimensional interface [23]. Materials which have been investigated include interfaces between metallic layers, e.g., in Bi/Ag interfaces [30, 31, 32], conducting interfaces between $LaAlO_3/SrTiO_3$ insulating oxide layers [33, 34, 35, 36, 37, 38, 39], and topological insulators [1, 40]. Three-dimensional topological insulators are made of heavy element compounds, e.g., $Bi_2Se_3$, where strong bulk spin-orbit interactions give rise to surface or edge states with RSOC. Heterostructures involving metal-oxide interfaces [41, 42] as well as graphene [2, 43, 44, 45] in which RSOC is enhanced by the proximity effect and transition metal dichalcogenides [22, 23], also present systems in which RSOC is prominent along an interface or a surface.

## 1.4 Materials hosting Edelstein and inverse Edelstein effects

The strength of the Edelstein effect (EE) and inverse Edelstein effect (IEE) is quantified by,

$$q_{EE} \equiv \left| \frac{\boldsymbol{J_S}}{\boldsymbol{J_C}} \right|, \quad \lambda_{IEE} \equiv \left| \frac{\boldsymbol{J_C}}{\boldsymbol{J_S}} \right|, \tag{1.5}$$

where $\boldsymbol{J}_S$ is the three-dimensional spin current density and $\boldsymbol{J_C}$ the two-dimensional charge current density [46, 47]. For Rashba interfaces, the IEE conversion parameter is given by $\lambda_{IEE} = \alpha\tau/\hbar$ where $\tau$ is the relaxation time of the nonequilibrium distribution of interface states [46, 23]. Therefore, materials with large RSOC along interfaces or surfaces are more favourable candidates for spintronics due to their high charge to spin current conversion properties [23]. The spin current density and charge current density in materials with RSOC

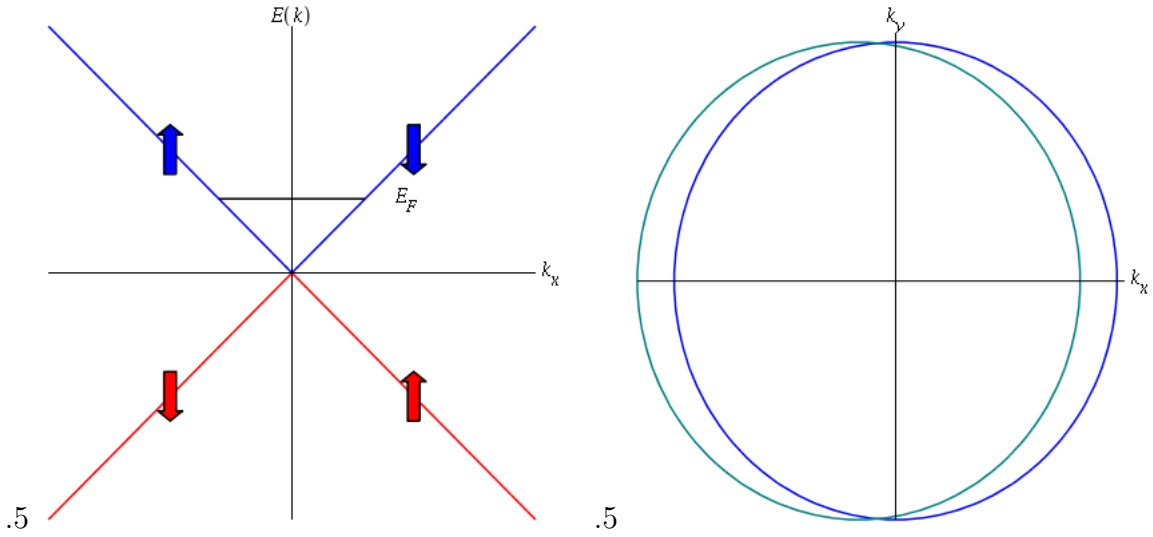


**Figure 1.3:** (Left) The surface state dispersion relation of a three-dimensional topological insulator with a defined Fermi level $E_F$. The upper blue lines represent the conduction band while the lower red lines represent the valence band. (Right) An applied electric field $\boldsymbol{E} = \varepsilon\hat{x}$ causes a finite shift in the Fermi circle of surface states, blue to light blue circles.

are related by

$$\boldsymbol{J}_S \propto \frac{\alpha}{e\hbar}(\hat{z} \times \boldsymbol{J}_C). \tag{1.6}$$

The EE was first observed in nonmagnetic layers in the Bi/Ag interface using a polarized positron beam, which was able to test the spin polarization of the surface electrons [30]. Using a charge current density of $\boldsymbol{J_C} = 15$ A/m, the spin polarization density of surface electrons was measured by increasing the thickness of the Bi layer on a Ag sample. The surface spin polarization was found to have a peak value when the Bi layer is about 0.3 nm thick [30], which is approximately monolayer [23], while decreasing as the Bi layer increased in thickness [30]. The IEE in the Bi/Ag interface was studied by Rojas-Sanchez et al. using a thin NiFe layer grown on the Bi/Ag sample [46]. The NiFe layer is used as a spin-pumping source, a process of injecting spin-polarized carriers from a ferromagnetic source into an adjacent layer [23], which results in a spin current created at the interface with the Bi/Ag sample [46]. The spin current density at the Bi/Ag interface was found to induce an associated charge current density due to the IEE, which was measured to have values of $\lambda_{IEE}$ ranging from 0.2 nm to 0.33 nm [46]. The two-dimensional conducting electron gas that exists between the

insulating oxides $SrTiO_3$ and $LaAlO_3$ [33] is another system which has been experimentally investigated for the EE and IEE [23]. Using a thin NiFe layer as a spin pumping source, Song et al. measured the voltage across the $SrTiO_3/LaAlO_3$ interface created due to the IEE at room temperature [48]. Using this inverse Edelstein voltage, a spin to charge conversion efficiency of $\lambda_{IEE} = 6.4$ nm has been reported [48, 49, 23]. Applying an electric field at the $SrTiO_3/LaAlO_3$ interface has been shown to create a large spin-orbit torque in an adjacent CoFeB layer attributed to the EE [50]. Purely two-dimensional materials present yet another group of systems which exhibit charge to spin conversion properties [23]. The low value for spin-orbit coupling strength present in graphene can be enhanced with the proximity effect with materials with large spin orbit coupling [23]. Heterostructures composed of graphene and yttrium iron garnet increase the spin orbit coupling in graphene and therefore enhance the charge to spin conversion properties [51, 52]. Transition metal dichalcogenides (TMDC) such as $WTe_2$ and $MoS_2$ possess large intrinsic spin-orbit coupling [53]. Recent experiments involving heterostructures of TMDCs and ferromagnetic layers such as NiFe have revealed the generation of large spin orbit torques attributed to the EE [22, 23].

As mentioned in Sec. 1.1, the conducting surface states of topological insulators exhibit a perpendicular orientation between spin and momentum [8]. The spin-momentum locking of the surface states presents topological insulators as a possible material to be used in the field of spintronics [23, 54]. One example which has been studied for its potential applications to spintronics is the three-dimensional topological insulator $Bi_2Sb_3$ [55, 54]. The Edelstein effect has been observed in $Bi_2Se_3$ using $Co_{40}Fe_{40}B_{20}$ as the adjacent magnetic layer. The IEE conversion parameter is given by $\lambda_{IEE} = v_F\tau$ for topological insulators, where $v_F$ is the Fermi velocity. $Bi_2Sb_3$ has been shown to produce spin-orbit torques which are attributed to its topological surface states [56], indicating that topological insulators with large spin-orbit coupling can be useful for spintronics. The Fermi level dependence of charge to spin conversion properties has been studied in $(Bi_{1-x}Sb_x)_2Te_3$ thin films in Cu/NiFe trilayer heterostructures [55]. By adjusting the value of x (Sb content), the Fermi level is located above the Dirac point for $0 < x < 0.84$ and below the Dirac point for $0.84 < x < 1$ for the topological surface

states [55]. Figure 1.3 shows the dispersion relation for the topological surface states with the Fermi level ($E_F$) located in the conduction band, above the Dirac point. Applying an electric field in $+x$ direction to the surface of $(Bi_{1-x}Sb_x)_2Te_3$ for $0 < x < 0.84$ results in a change of electron populations above the Dirac point [47]. In responce to the applied electric field, electrons populate states with $k_x < 0$ at the expense of states with $k_x > 0$ resulting in a shift of the Fermi circle $\delta k_x$, depicted in Fig. (1.3) [47]. The shifted Fermi circle implies larger population of electrons with $+y$ spin orientation and results in a net spin density [47]. The spin accumulation at the surface of the topological insulator is expressed as [47]

$$\langle S_0 \rangle = \frac{\hbar}{2} k_F \delta k_x = \frac{e k_F E_x \tau}{2} = \frac{\mu k_F^2 \hbar E_x}{2 v_F}, \tag{1.7}$$

where $k_F$ is the Fermi wavenumber, $E_x$ is the applied electric field and $\mu$ is the mobility of the topological surface states [47]. Varying the concentration of Sb, the EE conversion parameter varies from 0.4nm to 1.1nm as $x$ varies from 0 to 1. The recently discovered topological insulator $\alpha$-Sn has also been studied for its charge to spin conversion properties [57]. Using Ag as the spin pumping source in Ag/$\alpha$-Sn heterostructures the IEE conversion parameter has been reported to be $\approx$2.1nm at room temperature [57].

# 2 Theoretical Background

## 2.1 Interdimensional quantum well and thin interface systems

Materials containing surfaces or interfaces in three-dimensional systems which affect the propagation properties of particles (or quasiparticles), can be described using low-dimensional quantum mechanics. Analytic models can be constructed to include extra substructure terms, which affect propagation properties of nonrelativistic electrons through a change in effective mass [58], or confinement in the form of a quantum well [59]. In both cases the Hamiltonian is constructed as a linear superposition of a free three-dimensional electron gas, with a low-dimensional substructure contribution describing the effect of a surface or interface. The density of states inside the low-dimensional structure, which allows for the calculation of, e.g., number of charge carriers and thermal conductivity, can be calculated analytically for these types of Hamiltonians and is therefore of great interest for materials science. The models discussed in this thesis will build upon the quantum well [59] and thin interface with a change in effective mass [58] systems, to include the effects of RSOC along an interface or surface. Therefore we present the results of the density of states at the location of the low-dimensional structure (and particle density for the quantum well system) as an introduction to interdimensional models and as future reference.

### 2.1.1 Interdimensional quantum well system

Consider a three-dimensional free electron gas with a two-dimensional interface of thickness $L_\perp$ which affects progagtion properties through a confining potential

$$V(z) = -V_0\Theta(z_0 + L_\perp/2 - z)\Theta(z - z_0 + L_\perp/2), \tag{2.1}$$

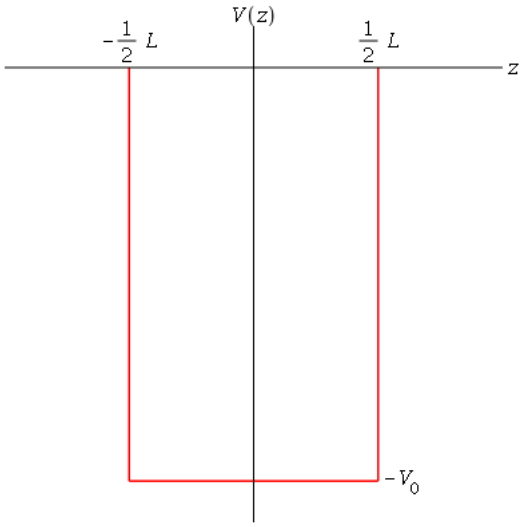


**Figure 2.1:** Plot of $V(z) = -V_0$ which exists over the interface thickness $L_\perp$ centered about $z = z_0$.

where $V_0 > 0$ and $\Theta(z)$ represents the Heaviside function whose properties can be found in Ref. [60]. The thickness of the interface is centered about the point $z = z_0$, and is assumed to extend infinitely in the $x$ and $y$ directions. Figure 2.1 displays the attractive potential and Fig. 2.2 qualitatively displays the interface inside the surrounding bulk. By taking the limit that $L_\perp$ becomes infinitely small, we can describe the interdimensional system by the Hamiltonian [59],

$$H = \frac{\boldsymbol{p}^2}{2m} - V_0 L_\perp \delta(z - z_0). \tag{2.2}$$

The quantum well exhibits confining properties through the binding energy $B = \hbar^2\kappa^2/2m$, with an inverse penetration depth $\kappa = mV_0L_\perp/\hbar^2$. The corresponding density of states which enumerates states per energy and per volume at the location of the quantum well structure ($z = z_0$) is given by

$$\varrho(E, z_0) = \kappa\varrho_{d=2}(E + (\hbar^2\kappa^2/2m)) + \varrho_{d=3}(E)\left[1 - \frac{\hbar\kappa}{\sqrt{2mE}} \arctan\left(\frac{\sqrt{2mE}}{\hbar\kappa}\right)\right], \tag{2.3}$$

where

$$\varrho_d(E) = 2\Theta(E)\sqrt{\frac{m}{2\pi}}^d \frac{\sqrt{E}^{d-2}}{\Gamma(d/2)\hbar^d} \tag{2.4}$$

is the density of states for nonrelativistic particles of mass $m$ in $d$ spatial dimensions. Integrating the density of states $\varrho(E, z_0)$ yields the relation between Fermi energy and particle

density inside the quantum well [59]:

$$n(z_0)\Big|_{-B<E_F<0} = \frac{\kappa m}{\pi\hbar^2}\left(E_F + \frac{\hbar^2\kappa^2}{2m}\right) = \kappa n_2\Big|_{E_{2,F}=K_{2,F}},$$

$$\begin{aligned} n(z_0)\Big|_{E_F>0} =& \frac{\kappa}{2\pi^2\hbar^2}\left[\hbar\kappa\sqrt{2mE_F} - (\hbar^2\kappa^2 + 2mE_F)\arctan\left(\frac{\sqrt{2mE_F}}{\hbar\kappa}\right)\right] \\ &+ \frac{\kappa m}{\pi\hbar^2}\left(E_F + \frac{\hbar^2\kappa^2}{2m}\right) + \frac{1}{3\pi^2}\left(\frac{\sqrt{2mE_F}}{\hbar}\right)^3, \end{aligned} \tag{2.5}$$

where

$$n_d = \frac{2}{\hbar^d\Gamma((d+2)/2)}\sqrt{\frac{mE_F}{2\pi}}^d, \tag{2.6}$$

is the density of particles in $d$ dimensions, and $K_{2,F} = E_F + \hbar^2\kappa^2/2m$ is the kinetic energy along the quantum well. The analytic results for the density of states and electron density inside the quantum well smoothly transition from two-dimensional to three-dimensional behavior as the inverse penetration depth $\kappa$ approaches zero. Both results demonstrate that bound states exist for $E \geq -B$, and that electrons confined to the quantum well contribute a two-dimensional density term, made dimensionally correct through the factor $\kappa$, reflecting the three-dimensional nature of the system.

### 2.1.2 Interdimensional thin interface with effective mass $m_*$

The nonrelativistic system in which electrons move in the presence of a two-dimensional interface of thickness $L_\perp$ with an effective mass $m_*$ is described by the Hamiltonian

$$H = \frac{\boldsymbol{p}^2}{2m} + |z_0\rangle\langle z_0|\frac{\boldsymbol{p}_\parallel^2}{2\mu} \tag{2.7}$$

where $\mu = m_*/L_\perp$. It will be common practice in this thesis to work with interdimensional Hamiltonians in the second quantized theory, therefore, we give the corresponding second quantized Hamiltonian corresponding to Eq. (2.7),

$$H = \int d^2\boldsymbol{x}_\parallel \int dz \frac{\hbar^2}{2m}\boldsymbol{\nabla}\psi^\dagger(\boldsymbol{x}_\parallel, z)\cdot\boldsymbol{\nabla}\psi(\boldsymbol{x}_\parallel, z) + \int d^2\boldsymbol{x}_\parallel \frac{\hbar^2}{2\mu}\boldsymbol{\nabla}_\parallel\psi^\dagger(\boldsymbol{x}_\parallel, z_0)\cdot\boldsymbol{\nabla}_\parallel\psi(\boldsymbol{x}_\parallel, z_0). \tag{2.8}$$

Equation (2.8) remains valid over a finite interface thickness provided that the wavenumber component orthogonal to the interface is small compared to the inverse width, $|k_\perp L_\perp| \ll 1$

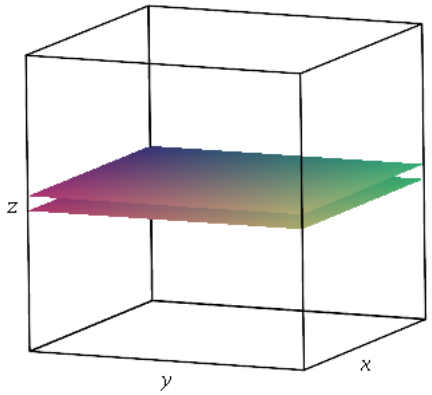


**Figure 2.2:** Geometric representation of the interface used in Sec. 2.1. The upper and lower planes represent the upper and lower edges of the interface of thickness $L_\perp$ which is centered about $z = z_0$. The three-dimensional system extends infinitely in all directions.

[58]. This condition can also be expressed in terms of the de Broglie wavelength. The relation between the components of the wave vector $\boldsymbol{k}$ and the de Broglie wavelength $\lambda$ for periodic boundary conditions is given by

$$k_i = \frac{2\pi}{\lambda} \cos\theta_i, \tag{2.9}$$

where $\cos\theta_i$ is the directional cosine of $\boldsymbol{k}$. Multiplying the wavevector component equation by the interface thickness $L_\perp$ and isolating for the de Broglie wavelength yields the condition

$$\lambda = \frac{2\pi L_\perp}{k_\perp L_\perp} \cos\theta_\perp \gg 2\pi L_\perp |\cos\theta_\perp|, \tag{2.10}$$

where we have used $|k_\perp L_\perp| \ll 1$. Under this approximation the wavefunction can be treated as constant in the direction of interface thickness, $z$. The density of states at the location of

the interface is given by

$$\begin{aligned}\varrho(E,z_0) &= \frac{m\Theta(E)\Theta(\hbar^2-8mE\ell^2)}{2\pi^2\hbar^2\ell\sqrt{\hbar^2-8mE\ell^2}} \\ &\times\left[2\hbar\arctan\left(\frac{\ell\sqrt{8mE}}{\hbar+\sqrt{\hbar^2-8mE\ell^2}}\right)-\frac{\pi}{2}\left(\hbar-\sqrt{\hbar^2-8mE\ell^2}\right)\right] \\ &+\frac{m\Theta(8mE\ell^2-\hbar^2)}{2\pi^2\hbar^2\ell} \\ &\times\left[\frac{\hbar}{\sqrt{8mE\ell^2-\hbar^2}}ln\left(\frac{\ell\sqrt{8mE}-\sqrt{8mE\ell^2-\hbar^2}}{\hbar}\right)+\frac{\pi}{2}\right],\end{aligned} \tag{2.11}$$

where $\ell \equiv m/2\mu = L_\perp m/2m_*$. The density of states reduces to the two-dimensional density of states for large energies [58], if the states probe length scales smaller than $\ell$. The three-dimensional limit is found in the small energy limit, when the states probe length scales larger than $\ell$. Mathematically this can be stated as, given $8mE\ell^2 \gg \hbar^2$,

$$\varrho(E,z_0) \to \Theta(E)\frac{m}{4\pi\hbar^2\ell} = \frac{1}{4\ell}\varrho_{(d=2)}(E). \tag{2.12}$$

Given the case $8mE\ell^2 \ll \hbar^2$,

$$\varrho(E,z_0) \to \Theta(E)\frac{\sqrt{2m^3}}{\pi^2\hbar^3}\sqrt{E} = \varrho_{(d=3)}(E). \tag{2.13}$$

## 2.2 Methodology for calculating density of states using wavefunctions and Green operator

In this section we will discuss the methods used to calculate the density of states in interfaces or along surfaces in the interdimensional models discussed in this thesis.

### 2.2.1 Relation between nonrelativistic fermionic Green operator and density of states

We can easily extend the well-known relation [26],

$$\varrho(E,\boldsymbol{x}) = -\frac{1}{\pi}\Im\langle\boldsymbol{x}|\mathcal{G}(E)|\boldsymbol{x}\rangle = \frac{2m}{\pi\hbar^2}\Im\langle\boldsymbol{x}|G(E)|\boldsymbol{x}\rangle, \tag{2.14}$$

between the local density of states $\varrho(E, \boldsymbol{x})$ and the energy-dependent Green operator,

$$\mathcal{G}(E) = \frac{1}{E - H + i\epsilon} = -\frac{2m}{\hbar^2} G(E). \tag{2.15}$$

Introducing unity in the form of eigenstates $|n, \nu\rangle$ of the Hamiltonian and using the Sokhotsky-Plemelj relation yields

$$\begin{aligned} \mathcal{G}(E) &= \sum\!\!\!\!\!\!\int_{n,\nu} \frac{|n,\nu\rangle\langle n,\nu|}{E - E_n + i\epsilon}, \\ &= \mathcal{P} \sum\!\!\!\!\!\!\int_{n,\nu} \frac{|n,\nu\rangle\langle n,\nu|}{E - E_n} - i\pi \sum\!\!\!\!\!\!\int_{n,\nu} \delta(E - E_n)|n,\nu\rangle\langle n,\nu|. \end{aligned} \tag{2.16}$$

The connection between the energy-dependent Green function and the density of states for fermions represented by a two-component spinor is given by

$$\begin{aligned} \varrho(E, \boldsymbol{x}) &= \sum\!\!\!\!\!\!\int_{n,\nu} dE_n d\nu(E_n) \delta(E - E_n) |\langle \boldsymbol{x}|n,\nu\rangle|^2 \\ &= \frac{2m}{\pi\hbar^2} \operatorname{Tr}[\Im\langle \boldsymbol{x}|G(E)|\boldsymbol{x}\rangle], \end{aligned} \tag{2.17}$$

The summation over $\nu$ in Eq. (2.17) includes both orbital degeneracy indices and spins.

### 2.2.2 Relation between the relativistic fermionic Green operator and density of states

We want to generalize the relation between the Green function matrix element and the density of states for relativistic fermions. The relativistic fermionic Green operator is, using the convention $\eta_{00} = -1$ for the Minkowski metric, given by

$$\begin{aligned} S &= \frac{\hbar}{mc + \gamma \cdot p} \\ &= \frac{\hbar(mc - \gamma \cdot p)}{p^2 + m^2c^2 - i\epsilon}. \end{aligned} \tag{2.18}$$

This yields the momentum-space Green function using plane wave states with wave vectors $k = (k^0, \boldsymbol{k})$,

$$\langle k|S|k'\rangle = \frac{(mc/\hbar - \gamma \cdot k)\delta(k - k')}{k^2 + m^2c^2/\hbar^2 - i\epsilon}. \tag{2.19}$$

We can rewrite the relativistic fermionic Green operator $S$ in terms of the Dirac Hamiltonian $H = \gamma^0 c(mc + \boldsymbol{\gamma} \cdot \boldsymbol{p})$ and $E = cp^0$ in the form,

$$S = -\gamma^0 \frac{1}{E - H + i\epsilon}. \tag{2.20}$$

We can make the transition to the energy-dependent Green operator $S(E)$ with classical variable $E = \hbar c k^0$ using $|k\rangle = |\boldsymbol{k}\rangle \otimes |k^0\rangle$ and

$$\langle k^0|S|k'^0\rangle = S(E)\delta(k^0 - k'^0). \tag{2.21}$$

The complete set of positive and negative energy eigenstates are with $E(\boldsymbol{k}) = \hbar c\sqrt{\boldsymbol{k}^2 + (mc/\hbar)^2}$ and $H|\boldsymbol{k}, \pm, s\rangle = \pm E(\boldsymbol{k})|\boldsymbol{k}, \pm, s\rangle$ given by

$$\begin{aligned}\langle \boldsymbol{x}|\boldsymbol{k}, +, s\rangle &= \frac{\exp(i\boldsymbol{k}\cdot\boldsymbol{x})}{4\pi\sqrt{\pi E(\boldsymbol{k})}}u(\boldsymbol{k}, s),\\ \langle \boldsymbol{x}|\boldsymbol{k}, -, s\rangle &= \frac{\exp(i\boldsymbol{k}\cdot\boldsymbol{x})}{4\pi\sqrt{\pi E(\boldsymbol{k})}}v(-\boldsymbol{k}, s).\end{aligned} \tag{2.22}$$

Use of the completeness relation,

$$1 = \sum_{s\in(\uparrow,\downarrow)}\int d^3\boldsymbol{k}(|\boldsymbol{k}, +, s\rangle\langle\boldsymbol{k}, +, s| + |\boldsymbol{k}, -, s\rangle\langle\boldsymbol{k}, -, s|), \tag{2.23}$$

and the Sokhotsky-Plemelj relation then yields

$$\begin{aligned}\Im S(E) &= \pi\hbar c\gamma^0\sum_{s\in(\uparrow,\downarrow)}\int d^3\boldsymbol{k}(\delta(E - E(\boldsymbol{k}))|\boldsymbol{k}, +, s\rangle\langle\boldsymbol{k}, +, s|\\ &\quad -\delta(E + E(\boldsymbol{k}))|\boldsymbol{k}, -, s\rangle\langle\boldsymbol{k}, -, s|).\end{aligned} \tag{2.24}$$

Equation (2.24) yields the relation between the relativistic fermionic Green function and the density of states,

$$\mathrm{Tr}(\Im\langle\boldsymbol{x}|S(E)|\boldsymbol{x}\rangle) = \frac{\pi\hbar mc^3}{E}[\varrho(E) - \overline{\varrho}(\overline{E})], \tag{2.25}$$

where $\overline{E} = -E$. We can test the validity of Eq. (2.25) in the free (anti-)particle case where the density of states in $d$ spatial dimensions for fermions is given by

$$\begin{aligned}\hat{\varrho}(E) &= \varrho(E) + \overline{\varrho}(\overline{E})\\ &= \frac{4\Theta(E^2 - m^2c^4)}{(2\hbar c\sqrt{\pi})^d\Gamma(d/2)}|E|\sqrt{E^2 - m^2c^4}^{d-2}.\end{aligned} \tag{2.26}$$

The time-dependent relativistic fermionic Green function in $\boldsymbol{x}$ representation is related to the relativistic scalar Green function $G(\boldsymbol{x}, t)$ by

$$S(\boldsymbol{x}, t) = (i\gamma^\mu\partial_\mu + (mc/\hbar))\,G(\boldsymbol{x}, t). \tag{2.27}$$

The $\boldsymbol{x}$ representation $\langle \boldsymbol{x}|S(E)|\boldsymbol{x}'\rangle = S(\boldsymbol{x}-\boldsymbol{x}',\omega)$ of the energy-dependent relativistic fermionic Green function is related to $G(\boldsymbol{x}-\boldsymbol{x}',\omega)$ by

$$\mathrm{Tr}(S(\boldsymbol{x},\omega)) = 4(mc/\hbar)G(\boldsymbol{x},\omega), \tag{2.28}$$

Using the expression for $G(\boldsymbol{x},\omega)$ in $d$ spatial dimensions found in Appendix I of Ref. [26] yields

$$\begin{aligned}
\mathrm{Tr}(S(\boldsymbol{x},\omega)) &= \frac{4mc}{\hbar}\frac{\Theta(mc^2-\hbar|\omega|)}{(2\pi)^{d/2}}\left(\frac{\sqrt{m^2c^4-\hbar^2\omega^2}}{\hbar cr}\right)^{\frac{d-2}{2}} \\
&\quad\times K_{\frac{d-2}{2}}\left(\sqrt{m^2c^4-\hbar^2\omega^2}\,\frac{r}{\hbar c}\right) \\
&\quad + i\frac{2\pi mc}{\hbar}\frac{\Theta(\hbar|\omega|-mc^2)}{(2\pi)^{d/2}}\left(\frac{\sqrt{\hbar^2\omega^2-m^2c^4}}{\hbar cr}\right)^{\frac{d-2}{2}} \\
&\quad\times H^{(1)}_{\frac{d-2}{2}}\left(\sqrt{\hbar^2\omega^2-m^2c^4}\,\frac{r}{\hbar c}\right)
\end{aligned} \tag{2.29}$$

We follow the definitions and conventions defined in Ref. [60] for the modified Bessel function, $K_\nu(z)$, and the Hankel function of first kind, $H^{(1)}_\nu(z)$, respectively. In particular, the modified Bessel function is real for a real argument, while the real part of the Hankel function of first kind satisfies [60]

$$\lim_{z\to 0}\Re H^{(1)}_\nu(z) = \frac{(z/2)^\nu}{\Gamma(\nu+1)}. \tag{2.30}$$

Application of the limiting value for the Hankel function of first kind into Eq. (2.29) for $r = |\boldsymbol{x}-\boldsymbol{x}'|$ yields

$$\begin{aligned}
\mathrm{Tr}(\Im\langle \boldsymbol{x}|S(E)|\boldsymbol{x}'\rangle) &= \frac{4\pi\hbar mc^3\Theta(E^2-m^2c^4)}{(2\hbar c\sqrt{\pi})^d\Gamma(d/2)} \\
&\quad\times\sqrt{E^2-m^2c^4}^{\,d-2},
\end{aligned} \tag{2.31}$$

which is in full agreement with Eq. (2.25) and Eq. (2.26).

### 2.2.3 Density of states for interfaces with $\boldsymbol{k}_\parallel$-dependent bound state wavenumbers

Consider an interface such that the dispersion relation takes the form

$$E = E(|\boldsymbol{k}_\parallel|,\kappa_n) \equiv E_n(|\boldsymbol{k}_\parallel|), \tag{2.32}$$

for bound states $|\boldsymbol{k}_\parallel, \kappa_n\rangle$ with $E < \hbar^2\boldsymbol{k}_\parallel^2/2m$, and

$$E = E(|\boldsymbol{k}_\parallel|, k_\perp), \tag{2.33}$$

for the unbound states $|\boldsymbol{k}_\parallel, k_\perp\rangle$ with $E < \hbar^2\boldsymbol{k}_\parallel^2/2m$. From Ref. [58], the energy-dependent density of states is given by (with factors of 2 for spin)

$$\begin{aligned}\varrho(E,\boldsymbol{x}) =& 2\int d^2\boldsymbol{k}_\parallel \Bigg( \sum_n \delta(E - E_n(|\boldsymbol{k}_\parallel|))|\langle \boldsymbol{x}|\boldsymbol{k}_\parallel, \kappa_n\rangle|^2 \\ &+ \Theta(E - \hbar^2\boldsymbol{k}_\parallel^2/2m)\frac{\partial k_\perp(E,\boldsymbol{k}_\parallel)}{\partial E}|\langle \boldsymbol{x}|\boldsymbol{k}_\parallel, k_\perp\rangle|^2\Big|_{k_\perp = k_\perp(E,\boldsymbol{k}_\parallel)}\Bigg) \\ =& 2\int_0^{2\pi} d\varphi k_\parallel \frac{\partial k_\parallel(E,\kappa_n)}{\partial E}|\langle \boldsymbol{x}|\boldsymbol{k}_\parallel, \kappa_n\rangle|^2\Big|_{|\boldsymbol{k}_\parallel| = k_\parallel(E,\kappa_n)} \\ &+ 2\int d^2\boldsymbol{k}_\parallel \Theta(E - \hbar^2\boldsymbol{k}_\parallel^2/2m)\frac{\partial k_\perp(E,\boldsymbol{k}_\parallel)}{\partial E}|\langle \boldsymbol{x}|\boldsymbol{k}_\parallel, k_\perp\rangle|^2\Big|_{k_\perp = k_\perp(E,\boldsymbol{k}_\parallel)}.\end{aligned} \tag{2.34}$$

Equation (2.34) yields consistent results for the density of states $\varrho(E, z_0)$ to those found in Ref. [59] using the Green function method. In the case of a two-component spinor wavefunction, the factor of 2 in Eq. (2.34) is replaced by a sum over eigenspinors:

$$\begin{aligned}\varrho(E,\boldsymbol{x}) =& \sum_\pm \int_0^{2\pi} d\varphi k_\parallel \frac{\partial k_\parallel(E,\kappa_\pm)}{\partial E}|\langle \boldsymbol{x}|\boldsymbol{k}_\parallel, \kappa_\pm\rangle|^2\Big|_{|\boldsymbol{k}_\parallel| = k_\parallel(E,\kappa_\pm)} \\ &+ \sum_\pm \int d^2\boldsymbol{k}_\parallel \Theta(E - \hbar^2\boldsymbol{k}_\parallel^2/2m)\frac{\partial k_\perp(E,\boldsymbol{k}_\parallel)}{\partial E}|\langle \boldsymbol{x}|\boldsymbol{k}_\parallel, k_\perp\rangle_\pm|^2\Big|_{k_\perp = k_\perp(E,\boldsymbol{k}_\parallel)}.\end{aligned} \tag{2.35}$$

# 3 Formulation of Interdimensional Systems for Fermions

## 3.1 Formulation of interdimensional nonrelativistic systems with RSOC

In this section we will present the interdimensional Hamiltonian for various systems featuring RSOC along an interface at $z = z_0$. We will present the associated wavefunctions and Green function equation which can be used in conjunction with Eqs. (2.35, 2.17) to calculate the interdimensional density of states.

### 3.1.1 Formulation of interdimensional system with pure RSOC interface

Motivated by materials which exhibit novel features on interfaces or surfaces as a result of RSOC, as well as heterostructures where RSOC in the interface is enhanced by the neighboring substrate [23, 22], we construct a Hamiltonian as a superposition of a three-dimensional free electron gas and a two-dimensional interface featuring RSOC at $z = z_0$. Reference [25] studies a two-dimensional electron gas subject to a perturbation Hamiltonian operator of the form

$$H_{SO} = \alpha \left[\boldsymbol{\sigma} \times \boldsymbol{k}_{\parallel}\right] \cdot \hat{z} \tag{3.1}$$

where $\alpha$ is the (spin-orbit) coupling constant, $\boldsymbol{\sigma}$ are the Pauli matrices, $\boldsymbol{k}_{\parallel}$ is the two-dimensional wave vector and $\hat{z}$ is the unit vector in the direction perpendicular to the two-dimensional electron gas. Equation (3.1) is known as a Rashba spin-orbit coupling term. A logical first step in analyzing the effects of RSOC in an interdimensional model is to create

a system in which RSOC is the sole term in the interface term of the Hamiltonian. This preliminary model will serve as a starting point for comparison when we include additional terms in the interface. The construction of the Hamiltonian for electrons subject to spin-orbit coupling in the interface is as follows: We assume that the wavenumber component orthogonal to the interface is small compared to the inverse of the interface thickness $L_\perp$, i.e., $|k_\perp L_\perp| \ll 1$. This implies that the wavefunction in the direction orthogonal to the interface can be approximated as constant. This approximation yields a second quantized Hamiltonian

$$H = \int d^3\boldsymbol{x} \frac{\hbar^2}{2m} \boldsymbol{\nabla}\psi^\dagger(\boldsymbol{x}) \cdot \boldsymbol{\nabla}\psi(\boldsymbol{x}) - \int d^2\boldsymbol{x}_\parallel i\alpha L_\perp \psi^\dagger(\boldsymbol{x}_\parallel, z_0) \left(\boldsymbol{\sigma}_\parallel \times \boldsymbol{\nabla}_\parallel\right) \cdot \hat{z}\psi(\boldsymbol{x}_\parallel, z_0), \tag{3.2}$$

where $\boldsymbol{x} = (\boldsymbol{x}_\parallel, z)$ and $\boldsymbol{\sigma}_\parallel = (\sigma_x, \sigma_y)$. The eigenvalues and eigenfunctions of Eq. (3.2) are separated into states which are bound to the interface ($E < \hbar^2 k_\parallel^2/2m, \kappa > 0$),

$$\begin{aligned}\psi_{\boldsymbol{k}_\parallel,\kappa,+}(\boldsymbol{x}_\parallel, z) &= \langle \boldsymbol{x}_\parallel, z|\boldsymbol{k}_\parallel, \kappa, +\rangle \\ &= \frac{\exp(i\boldsymbol{k}_\parallel \cdot \boldsymbol{x}_\parallel)}{2\pi} \sqrt{\frac{\kappa}{2|\boldsymbol{k}_\parallel|}} \begin{pmatrix} \sqrt{k_+} \\ \mp\sqrt{k_-} \end{pmatrix} \exp(-\kappa|z - z_0|),\end{aligned}$$

$$E = \frac{\hbar^2}{2m}(\boldsymbol{k}_\parallel^2 - \kappa^2) = \frac{\hbar^2 k_\parallel^2}{2m}\left(1 - \frac{m^2\alpha^2 L_\perp^2}{\hbar^4}\right), \tag{3.3}$$

and two sets of orthogonal transversally free states ($k_\perp \geq 0$, $E = \hbar^2(\boldsymbol{k}_\parallel^2 + k_\perp^2)$) written as even (+) and odd (−) parity eigenstates,

$$\begin{aligned}\psi_{\boldsymbol{k}_\parallel,k_\perp,+}(\boldsymbol{x}_\parallel, z) =& \langle \boldsymbol{x}_\parallel, z|\boldsymbol{k}_\parallel, k_\perp, +\rangle \\ =& \frac{\exp(i\boldsymbol{k}_\parallel \cdot \boldsymbol{x}_\parallel)}{2\sqrt{\pi^3}\sqrt{1 + (m\alpha L_\perp|\boldsymbol{k}_\parallel|/\hbar^2 k_\perp)^2}} \Bigg( \cos(k_\perp(z - z_0)) \\ &+ \frac{m\alpha L_\perp}{\hbar^2 k_\perp} \begin{pmatrix} 0 & k_+ \\ k_- & 0 \end{pmatrix} \sin(k_\perp|z - z_0|) \Bigg) \begin{pmatrix} \cos\xi \\ e^{i\chi}\sin\xi \end{pmatrix},\end{aligned} \tag{3.4}$$

$$\begin{aligned}\psi_{\boldsymbol{k}_\parallel,k_\perp,-}(\boldsymbol{x}_\parallel, z) &= \langle \boldsymbol{x}_\parallel, z|\boldsymbol{k}_\parallel, k_\perp, -\rangle \\ &= \frac{\exp(i\boldsymbol{k}_\parallel \cdot \boldsymbol{x}_\parallel)}{2\pi} \frac{1}{\sqrt{\pi}} \sin(k_\perp(z - z_0)) \begin{pmatrix} \cos\xi \\ e^{i\chi}\sin\xi \end{pmatrix},\end{aligned} \tag{3.5}$$

where $\kappa = |\alpha| m L_\perp |\boldsymbol{k}_\parallel|/\hbar^2$ and $k_\pm = k_x \pm i k_y$. We also restrict the value of $\eta$ to satisfy $\eta^2 \leq 1$ to ensure that a ground state energy exists. Without this restriction, $E \to -\infty$ as $|\boldsymbol{k}_\parallel| \to \infty$ where $E$ is the energy in Eq. (3.3). The time-independent Schrödinger equation that corresponds to Eq. (3.2) is calculated using the Heisenberg equation of motion,

$$i\hbar \frac{\partial \psi(\boldsymbol{x}, t)}{\partial t} = -\left[H, \psi(\boldsymbol{x}, t)\right]. \tag{3.6}$$

The time dependence of the field $\psi(\boldsymbol{x}, t)$ can be separated using $\psi(\boldsymbol{x}, t) = \psi(\boldsymbol{x}) \exp(-iEt/\hbar)$. Insertion of Eq. (3.2) into the Heisenberg equation yields

$$\left[\frac{2mE}{\hbar^2} + \boldsymbol{\nabla}^2 - i\delta(z - z_0)\frac{2m\alpha L_\perp}{\hbar^2}\left(\partial_x \sigma_y - \partial_y \sigma_x\right)\right]\psi(\boldsymbol{x}) = 0, \tag{3.7}$$

where $\psi(\boldsymbol{x}) = \binom{\psi_\uparrow(\boldsymbol{x})}{\psi_\downarrow(\boldsymbol{x})}$. The corresponding equation for the Green function is

$$\left[\frac{2mE}{\hbar^2} + \boldsymbol{\nabla}^2 - i\delta(z - z_0)\frac{2m\alpha L_\perp}{\hbar^2}\left(\partial_x \sigma_y - \partial_y \sigma_x\right)\right]\langle \boldsymbol{x}|G(E)|\boldsymbol{x'}\rangle = -\delta^3(\boldsymbol{x} - \boldsymbol{x'}). \tag{3.8}$$

The energy-dependent Green function in the $\boldsymbol{x}$ representation is found in Appendix A in the form of a Hankel transform,

$$\langle \boldsymbol{x}|G(E)|\boldsymbol{x'}\rangle = \frac{1}{2\pi}\int_0^\infty dk_\parallel k_\parallel J_0(k_\parallel |\boldsymbol{x} - \boldsymbol{x}'_\parallel|)\langle z|G(E, \boldsymbol{k}_\parallel)|z'\rangle. \tag{3.9}$$

### 3.1.2 Formulation of interdimensional system with RSOC plus change in effective mass interface

In this section we extend the work done in Sec. 3.1.1 to include a kinetic term in the interface with an effective mass $m_*$ in the nonrelativistic interdimensional Hamiltonian. This extension describes a system with RSOC in which electrons move with an effective mass $m_*$ compared to the bare mass $m$ for motion in the surrounding bulk. The interface between metallic layers Ag/Bi [30, 31] presents a system with RSOC and a different effective mass for motion in Ag compared to Bi. Extending the pure RSOC model in this way creates a more realistic model, and allows for results to be compared to the pure RSOC model as well as the thin interface with effective mass model discussed in Sec. 2.1.2. Applying the formulation in Secs. 2.1.2

and 3.1.1 yields a second quantized Hamiltonian,

$$H = \int d^3\boldsymbol{x} \frac{\hbar^2}{2m} \nabla\psi^\dagger(\boldsymbol{x}) \cdot \boldsymbol{\nabla}\psi(\boldsymbol{x}) \\ + \int d^2\boldsymbol{x}_\parallel \left( \frac{\hbar^2}{2\mu} \boldsymbol{\nabla}_\parallel \psi^\dagger(\boldsymbol{x}_\parallel, z_0) \cdot \boldsymbol{\nabla}_\parallel \psi(\boldsymbol{x}_\parallel, z_0) - i\alpha L_\perp \psi^\dagger(\boldsymbol{x}_\parallel, z_0) \left(\boldsymbol{\sigma}_\parallel \times \boldsymbol{\nabla}_\parallel\right) \cdot \hat{z}\psi(\boldsymbol{x}_\parallel, z_0) \right), \tag{3.10}$$

where $\boldsymbol{x} = (\boldsymbol{x}_\parallel, z)$, $\boldsymbol{\sigma}_\parallel = (\sigma_x, \sigma_y)$ and $\mu = m^*/L_\perp$. The eigenvalues and eigenfunctions of Eq. (3.10) are separated into states which are bound to the interface ($E < \hbar^2 k_\parallel^2/2m, \kappa > 0$),

$$\psi_{\boldsymbol{k}_\parallel,\kappa,+}(\boldsymbol{x}_\parallel, z) = \langle \boldsymbol{x}_\parallel, z | \boldsymbol{k}_\parallel, \kappa, + \rangle = \frac{\exp(i\boldsymbol{k}_\parallel \cdot \boldsymbol{x}_\parallel)}{2\pi} \sqrt{\frac{\kappa}{2|\boldsymbol{k}_\parallel|}} \begin{pmatrix} \sqrt{k_y + ik_x} \\ \mp\sqrt{k_y - ik_x} \end{pmatrix} \exp(-\kappa|z - z_0|), \tag{3.11}$$

where

$$E = \frac{\hbar^2}{2m}(\boldsymbol{k}_\parallel^2 - \kappa^2) = \frac{\hbar^2 k_\parallel^2}{2m} \left( 1 - \left( - \frac{m|\boldsymbol{k}_\parallel|}{2\mu} + \frac{m|\alpha|L_\perp}{\hbar^2} \right)^2 \right) \tag{3.12}$$

and

$$\kappa = -\frac{m\boldsymbol{k}_\parallel^2}{2\mu} + \frac{m|\alpha|L_\perp|\boldsymbol{k}_\parallel|}{\hbar^2}, \tag{3.13}$$

and two sets of orthogonal transversally free states ($k_\perp \geq 0$, $E = \hbar^2(\boldsymbol{k}_\parallel^2 + k_\perp^2)$) written as even (+) and odd (−) parity eigenstates,

$$\psi_{\boldsymbol{k}_\parallel,k_\perp,+}(\boldsymbol{x}_\parallel, z) = \langle \boldsymbol{x}_\parallel, z | \boldsymbol{k}_\parallel, k_\perp, + \rangle = \frac{\exp(i\boldsymbol{k}_\parallel \cdot \boldsymbol{x}_\parallel)}{2\sqrt{\pi^3}\sqrt{1 + (m\alpha L_\perp/\hbar^2 k_\perp)^2 \Phi^\dagger \cdot \boldsymbol{N}^2 \cdot \Phi}} \\ \times \left( \cos(k_\perp(z - z_0)) + \frac{m\alpha L_\perp}{\hbar^2 k_\perp} \boldsymbol{N} \sin(k_\perp|z - z_0|) \right) \Phi, \tag{3.14}$$

$$\psi_{\boldsymbol{k}_\parallel,k_\perp,-}(\boldsymbol{x}_\parallel, z) = \langle \boldsymbol{x}_\parallel, z | \boldsymbol{k}_\parallel, k_\perp, - \rangle = \frac{\exp(i\boldsymbol{k}_\parallel \cdot \boldsymbol{x}_\parallel)}{2\pi} \frac{1}{\sqrt{\pi}} \sin(k_\perp(z - z_0))\Phi, \tag{3.15}$$

where

$$\boldsymbol{N} = \begin{pmatrix} A\boldsymbol{k}_\parallel^2 & ik_- \\ -ik_+ & A\boldsymbol{k}_\parallel^2 \end{pmatrix}, \tag{3.16}$$

with $A = \hbar^2/(2\mu\alpha L_\perp)$ and $\Phi$ is a normalized 2-spinor. The eigenspinors of $\boldsymbol{N}$ are given by

$$\varphi_\pm(\boldsymbol{k}_\parallel) = \frac{1}{\sqrt{2}}\begin{pmatrix} 1 \\ \pm i k_+/|\boldsymbol{k}_\parallel| \end{pmatrix}. \tag{3.17}$$

Using the eigenspinors of $\boldsymbol{N}$ as the basis spinors yields the even-parity eigenstates

$$\psi_{\boldsymbol{k}_\parallel,k_\perp,+}(\boldsymbol{x}_\parallel, z)_\pm = \langle \boldsymbol{x}_\parallel, z|\boldsymbol{k}_\parallel, k_\perp, +\rangle_\pm = \frac{\exp(i\boldsymbol{k}_\parallel \cdot \boldsymbol{x}_\parallel)}{2\sqrt{\pi^3}\sqrt{1 + (m\alpha L_\perp/\hbar^2 k_\perp)^2 (A\boldsymbol{k}_\parallel^2 \pm |\boldsymbol{k}_\parallel|)^2}}$$
$$\times \left( \cos(k_\perp(z - z_0)) + \frac{m\alpha L_\perp}{\hbar^2 k_\perp}(A\boldsymbol{k}_\parallel^2 \pm |\boldsymbol{k}_\parallel|) \sin(k_\perp|z - z_0|) \right) \varphi_\mp(\boldsymbol{k}_\parallel). \tag{3.18}$$

The time-independent Schrödinger equation that corresponds to Eq. (3.10) is calculated using the Heisenberg equation of motion,

$$i\hbar \frac{\partial \psi(\boldsymbol{x}, t)}{\partial t} = -\left[H, \psi(\boldsymbol{x}, t)\right]. \tag{3.19}$$

The time dependence of the field $\psi(\boldsymbol{x}, t)$ can be separated using $\psi(\boldsymbol{x}, t) = \psi(\boldsymbol{x}) \exp(-iEt/\hbar)$. Insertion of Eq. (3.10) into the Heisenberg equation yields

$$\left[ \frac{2mE}{\hbar^2} + \boldsymbol{\nabla}^2 + \delta(z - z_0) \left( \frac{m}{\mu} \boldsymbol{\nabla}_\parallel^2 - i \frac{2m\alpha L_\perp}{\hbar^2} \left( \partial_x \sigma_y - \partial_y \sigma_x \right) \right) \right] \psi(\boldsymbol{x}) = 0, \tag{3.20}$$

where $\psi(\boldsymbol{x}) = \binom{\psi_\uparrow(\boldsymbol{x})}{\psi_\downarrow(\boldsymbol{x})}$. The corresponding equation for the Green function is

$$\left[ \frac{2mE}{\hbar^2} + \boldsymbol{\nabla}^2 + \delta(z - z_0) \left( \frac{m}{\mu} \boldsymbol{\nabla}_\parallel^2 - i \frac{2m\alpha L_\perp}{\hbar^2} \left( \partial_x \sigma_y - \partial_y \sigma_x \right) \right) \right] \langle \boldsymbol{x}|G(E)|\boldsymbol{x'}\rangle = -\delta^3(\boldsymbol{x} - \boldsymbol{x'}). \tag{3.21}$$

The energy-dependent Green function in the $\boldsymbol{x}$ representation is found in Appendix A in the form of a Hankel transform,

$$\langle \boldsymbol{x}|G(E)|\boldsymbol{x'}\rangle = \frac{1}{2\pi} \int_0^\infty dk_\parallel k_\parallel J_0(k_\parallel|\boldsymbol{x} - \boldsymbol{x}'_\parallel|) \langle z|G(E, \boldsymbol{k}_\parallel)|z'\rangle. \tag{3.22}$$

### 3.1.3 Formulation of interdimensional system with RSOC plus attractive potential interface

In this section we extend the work done in Sec. 3.1.1 to include an attractive potential to describe electrons experiencing RSOC which are confined to an interface. The introduction

of an attractive potential allows for an analysis of the Edelstein effect (and inverse Edelstein effect) [21], which was not possible in the models introduced in Secs. 3.1.1 and 3.1.2 due to the existence of only one bound state solution. Given that the existence of the Edelstein effect (and inverse Edelstein effect) serves as motivation for the investigation of Rashba interfaces [23], it is logical to analyze this interdimensional system. We construct the Hamiltonian as a superposition of a three-dimensional free electron gas and a two-dimensional interface located at $z = z_0$ featuring RSOC and an attractive potential. We extend the work done in Ref. [58] to include a RSOC term [25] and attractive potential $V(z) = -V_0\delta(z - z_0)$, $V_0 > 0$ in the interface term of the Hamiltonian. This yields a second quantized Hamiltonian,

$$H = \int d^3\boldsymbol{x}\frac{\hbar^2}{2m}\boldsymbol{\nabla}\psi^\dagger(\boldsymbol{x})\cdot\boldsymbol{\nabla}\psi(\boldsymbol{x}) - \int d^2\boldsymbol{x}_\parallel\Bigg(i\alpha L_\perp\psi^\dagger(\boldsymbol{x}_\parallel,z_0)\left(\boldsymbol{\sigma}_\parallel\times\boldsymbol{\nabla}_\parallel\right)\cdot\hat{z}\psi(\boldsymbol{x}_\parallel,z_0) + V_0\psi^\dagger(\boldsymbol{x}_\parallel,z_0)\cdot\psi(\boldsymbol{x}_\parallel,z_0)\Bigg), \tag{3.23}$$

where $\boldsymbol{x} = (\boldsymbol{x}_\parallel, z)$ and $\boldsymbol{\sigma}_\parallel = (\sigma_x, \sigma_y)$. The eigenvalues and eigenfunctions of Eq. (3.23) are separated into states which are bound to the interface ($E < \hbar^2k_\parallel^2/2m, \kappa > 0$),

$$\begin{aligned}\psi_{\boldsymbol{k}_\parallel,\kappa_\pm,+}(\boldsymbol{x}_\parallel,z) &= \langle\boldsymbol{x}_\parallel,z|\boldsymbol{k}_\parallel,\kappa_\pm,+\rangle \\ &= \frac{\exp(i\boldsymbol{k}_\parallel\cdot\boldsymbol{x}_\parallel)}{2\pi}\sqrt{\kappa_\pm}\exp(-\kappa_\pm|z-z_0|)\varphi_\pm(\boldsymbol{k}_\parallel)\Big|_{\kappa_\pm=(mL_\perp/\hbar^2)(V_0\pm\alpha k_\parallel)},\end{aligned} \tag{3.24}$$

$$E_\pm = \frac{\hbar^2}{2m}(\boldsymbol{k}_\parallel^2 - \kappa_\pm^2) = \frac{\hbar^2k_\parallel^2}{2m} - \frac{mL_\perp^2}{2\hbar^2}(V_0\pm\alpha k_\parallel)^2, \tag{3.25}$$

and two sets of orthogonal transversally free states ($k_\perp \geq 0$, $E = \hbar^2(\boldsymbol{k}_\parallel^2 + k_\perp^2)$) written as even (+) and odd (−) parity eigenstates,

$$\begin{aligned}\psi_{\boldsymbol{k}_\parallel,k_\perp,+}(\boldsymbol{x}_\parallel,z)_\pm =& \langle\boldsymbol{x}_\parallel,z|\boldsymbol{k}_\parallel,k_\perp,+\rangle_\pm \\ =& \frac{\exp(i\boldsymbol{k}_\parallel\cdot\boldsymbol{x}_\parallel)}{2\sqrt{\pi^3}\sqrt{1+(mL_\perp/\hbar^2k_\perp)^2(V_0\pm\alpha k_\parallel)^2}}\Bigg(\cos(k_\perp(z-z_0)) \\ &- \frac{mL_\perp}{\hbar^2k_\perp}(V_0\pm\alpha k_\parallel)\sin(k_\perp|z-z_0|)\Bigg)\varphi_\pm(\boldsymbol{k}_\parallel),\end{aligned} \tag{3.26}$$

$$\begin{aligned}\psi_{\boldsymbol{k}_\parallel,k_\perp,-}(\boldsymbol{x}_\parallel,z) &= \langle\boldsymbol{x}_\parallel,z|\boldsymbol{k}_\parallel,k_\perp,-\rangle \\ &= \frac{\exp(i\boldsymbol{k}_\parallel\cdot\boldsymbol{x}_\parallel)}{2\pi}\frac{1}{\sqrt{\pi}}\sin(k_\perp(z-z_0))\begin{pmatrix}\cos\xi\\ e^{i\chi}\sin\xi\end{pmatrix},\end{aligned} \tag{3.27}$$

$$\varphi_{\pm}(\boldsymbol{k}_{\parallel}) = \frac{1}{\sqrt{2}}\begin{pmatrix} 1 \\ \pm i k_{+}/k_{\parallel} \end{pmatrix}, \tag{3.28}$$

where $k_{\pm} = k_x \pm i k_y$. $\kappa_{-} > 0$ requires that $V_0/\alpha > k_{\parallel}$, which corresponds to $E_{-} < \hbar^2 V_0^2/2m\alpha^2$. We also require that $(m\alpha L_{\perp}/\hbar^2)^2 \leq 1$ to ensure that a ground state energy exists. Without this restriction, $E_{\pm} \to -\infty$ as $|\boldsymbol{k}_{\parallel}| \to \infty$, where $E_{\pm}$ is the energy in Eq. (3.25). The time-independent Schrödinger equation that corresponds to Eq. (3.23) is calculated using the Heisenberg equation of motion,

$$i\hbar \frac{\partial \psi(\boldsymbol{x}, t)}{\partial t} = -\left[H, \psi(\boldsymbol{x}, t)\right]. \tag{3.29}$$

The time dependence of the field $\psi(\boldsymbol{x}, t)$ can be separated using $\psi(\boldsymbol{x}, t) = \psi(\boldsymbol{x}) \exp(-iEt/\hbar)$. Insertion of Eq. (3.23) into the Heisenberg equation yields

$$\left[\frac{2mE}{\hbar^2} + \boldsymbol{\nabla}^2 + \delta(z - z_0)\left( - V_0 - i\frac{2m\alpha L_{\perp}}{\hbar^2}\left(\partial_x \sigma_y - \partial_y \sigma_x\right)\right)\right]\psi(\boldsymbol{x}) = 0, \tag{3.30}$$

where $\psi(\boldsymbol{x}) = \binom{\psi_{\uparrow}(\boldsymbol{x})}{\psi_{\downarrow}(\boldsymbol{x})}$. The corresponding equation for the Green function is

$$\left[\frac{2mE}{\hbar^2} + \boldsymbol{\nabla}^2 + \delta(z - z_0)\left( - V_0 - i\frac{2m\alpha L_{\perp}}{\hbar^2}\left(\partial_x \sigma_y - \partial_y \sigma_x\right)\right)\right]\langle \boldsymbol{x}|G(E)|\boldsymbol{x'}\rangle = -\delta^3(\boldsymbol{x} - \boldsymbol{x'}). \tag{3.31}$$

The energy-dependent Green function in the $\boldsymbol{x}$ representation is found in Appendix A in the form of a Hankel transform,

$$\langle \boldsymbol{x}|G(E)|\boldsymbol{x'}\rangle = \frac{1}{2\pi}\int_0^{\infty} dk_{\parallel} k_{\parallel} J_0(k_{\parallel}|\boldsymbol{x} - \boldsymbol{x}'_{\parallel}|)\langle z|G(E, \boldsymbol{k}_{\parallel})|z'\rangle. \tag{3.32}$$

## 3.2 Formulation of interdimensional system of quasirelativistic fermions with effective mass interface

As discussed in Sec. 1.1, three-dimensional topological insulators are a material candidate in the field of spintronics due to the spin-momentum locking of their surface states [1]. In order to investigate the surface states of topological insulators with linearly dispersing surface states, we introduce an interdimensional model of quasirelativistic fermions with an interface which affects propagation properties. This model does not include a spin-orbit coupling

term in the interface, and therefore is most directly applicable to topological crystalline insulators whose surface states are not a result of spin-orbit coupling [8]. Similar to early work in interdimensional models [58], this model serves as a beginning step in order to model interdimensional systems with spin-orbit coupling. Our work in this section is a natural progression of the work done in Ref. [58] for interdimensional effects in nonrelativistic systems of electrons, and Ref. [61] for interdimensional effects in systems of bosons with quasirelativistic dispersion relations. In order to study how the presence of an interface inside a three-dimensional bulk affects the local density of states for a relativistic fermion, we create an interdimensional Hamiltonian that includes extra spatial derivative terms and a change in bulk gap parameter $\Delta m$, due to motion inisde the interface located at $z = z_0$. Operating under the assumption that $\lambda_\perp \gg \ell$; where $\lambda_\perp$ represents the component of the de Broglie wavelength perpendicular to the interface and $\ell$ represents the interface thickness, the fermionic wave function $\Psi(x)$ is approximately constant in the direction perpendicular to the interface. This yields the form for the interdimensional Hamiltonian,

$$\begin{aligned} H &= \int d^3\boldsymbol{x}\overline{\Psi}(\boldsymbol{x},t)\left(mc^2 - i\hbar c\boldsymbol{\gamma}\cdot\boldsymbol{\nabla}\right)\Psi(\boldsymbol{x},t) \\ &\quad +\ell\int d^2\boldsymbol{x}_\parallel\overline{\Psi}(\boldsymbol{x}_\parallel,z_0,t)\left(\Delta mc^2 - i\hbar c\boldsymbol{\gamma}_\parallel\cdot\boldsymbol{\nabla}_\parallel\right)\Psi(\boldsymbol{x}_\parallel,z_0,t). \end{aligned} \tag{3.33}$$

Here the field $\Psi(x)$ is a 4-component Dirac spinor, and we use the Dirac basis for the gamma matrices $\gamma^\mu$, both of which are defined in Ref. [26]. The three-dimensional position vector has been broken into components parallel to the interface, $\boldsymbol{x}_\parallel$, and perpendicular to the interface, $z$. Using the anti-commutation relations for the fields $\Psi(x)$ and $\Psi^\dagger(x)$ defined in Ref. [26], we use the Heisenberg equation of motion,

$$i\hbar\frac{\partial\Psi}{\partial t} = -\left[H,\Psi\right],$$

where the Hamiltonian is defined in Eq. (3.33). Evaluating the Heisenberg equation yields the interdimensional equation of motion for the field $\Psi(x)$ given by

$$\left[i\hbar\gamma^0\partial_0 + i\hbar\boldsymbol{\gamma}\cdot\boldsymbol{\nabla} - mc + \ell\delta(z-z_0)\left(i\hbar\boldsymbol{\gamma}_\parallel\cdot\boldsymbol{\nabla}_\parallel - \Delta mc\right)\right]\Psi(\boldsymbol{x},t) = 0. \tag{3.34}$$

The corresponding interdimensional Green function matrix element $\langle x|S|x'\rangle$ therefore satisfies

$$\left[i\hbar\gamma^\mu\partial_\mu - mc + \ell\delta(z-z_0)\left(i\hbar\boldsymbol{\gamma}_\parallel\cdot\boldsymbol{\nabla}_\parallel - \Delta mc\right)\right]\langle x|S|x'\rangle = -\hbar\delta(x-x'). \tag{3.35}$$

The Fourier transform for the Green function matrix element is given by

$$\begin{aligned}\langle x|S|x'\rangle &= \langle x^0, \boldsymbol{x}_\parallel, z|S|x'^0, \boldsymbol{x}'_\parallel, z'\rangle \\ &= \frac{1}{\sqrt{2\pi}^7}\int dk^0 \int dk'^0 \int d^2\boldsymbol{k}_\parallel \int d^2\boldsymbol{k}'_\parallel \int dz \langle k^0, \boldsymbol{k}_\parallel, k_\perp|S|k'^0, \boldsymbol{k}'_\parallel, z'\rangle \\ &\quad \times \exp\left[i\left(\boldsymbol{k}_\parallel\cdot\boldsymbol{x}_\parallel - \boldsymbol{k}'_\parallel\cdot\boldsymbol{x}'_\parallel + k^0x^0 - k'^0x'^0 + k_\perp z\right)\right]. \end{aligned} \tag{3.36}$$

The fermionic Green function $\langle x|S|x'\rangle$ is related to the energy-dependent fermionic Green function through [see (Eq. 2.21)]

$$\langle k^0, \boldsymbol{x}|S|k'^0, \boldsymbol{x}'\rangle = \langle \boldsymbol{x}|S(E)|\boldsymbol{x}'\rangle \delta(k^0 - k'^0)|_{E=\hbar c k^0} \tag{3.37}$$

and

$$\langle x|S|x'\rangle = \frac{1}{2\pi}\int dk^0 \int dk'^0 \langle k^0, \boldsymbol{x}|S|k'^0, \boldsymbol{x}'\rangle \exp[i(k'^0x'^0 - k^0x^0)]. \tag{3.38}$$

The equivalent equation of motion to (Eq. 3.35) for $\langle \boldsymbol{x}|S(E)|\boldsymbol{x}'\rangle$ is given by

$$\left[\gamma^0\frac{E}{c} + i\hbar\boldsymbol{\gamma}\cdot\boldsymbol{\nabla} - mc + \ell\delta(z-z_0)\left(i\hbar\boldsymbol{\gamma}_\parallel\cdot\boldsymbol{\nabla}_\parallel - \Delta mc\right)\right]\langle \boldsymbol{x}|S(E)|\boldsymbol{x}'\rangle = -\hbar\delta(\boldsymbol{x}-\boldsymbol{x}'). \tag{3.39}$$

# 4 Results and Discussion

## 4.1 Interdimensional system with pure RSOC interface

### 4.1.1 Results of interdimensional system with pure RSOC interface

The energy-dependent Green function in the $\boldsymbol{x}$ representation is found in Appendix A in the form of a Hankel transform,

$$\langle \boldsymbol{x}|G(E)|\boldsymbol{x'}\rangle = \frac{1}{2\pi}\int_0^\infty dk_\parallel k_\parallel J_0(k_\parallel|\boldsymbol{x}-\boldsymbol{x'}_\parallel|)\langle z|G(E,\boldsymbol{k}_\parallel)|z'\rangle, \tag{4.1}$$

where

$$\begin{aligned}\langle z|G(E,\boldsymbol{k}_\parallel)|z'\rangle = &\frac{i\hbar\Theta(\gamma)}{2\sqrt{\gamma}}\exp\left(i\sqrt{\gamma}|z-z'|/\hbar\right)\overleftrightarrow{1} + \frac{\hbar\Theta(\beta)}{2\sqrt{\beta}}\exp\left(-\sqrt{\beta}|z-z'|/\hbar\right)\overleftrightarrow{1}\\ &+\left[\frac{i\hbar\Theta(\gamma)}{2\sqrt{\gamma}}\exp\left(i\sqrt{\gamma}|z-z_0|/\hbar\right) + \frac{\hbar\Theta(\beta)}{2\sqrt{\beta}}\exp\left(-\sqrt{\beta}|z-z_0|/\hbar\right)\right]Q(E,\boldsymbol{k}_\parallel,z')\end{aligned} \tag{4.2}$$

with $Q(E,\boldsymbol{k}_\parallel,z')$ defind in Appendix A and $\gamma = 2mE-\hbar^2\boldsymbol{k}_\parallel^2$, $\beta = \hbar^2\boldsymbol{k}_\parallel^2 - 2mE$. Applying $z = z' = z_0$ and taking the trace yields

$$\begin{aligned}\mathrm{Tr}\langle z_0|G(E,\boldsymbol{k}_\parallel)|z_0\rangle = &2\Bigg(\frac{i\hbar\Theta(2mE-\hbar^2\boldsymbol{k}_\parallel^2)\sqrt{2mE-\hbar^2\boldsymbol{k}_\parallel^2}}{2(2mE-\hbar^2\boldsymbol{k}_\parallel^2+\hbar^2\eta^2\boldsymbol{k}_\parallel^2)}\\ &+\frac{\hbar\Theta(\hbar^2\boldsymbol{k}_\parallel^2-2mE)\sqrt{\hbar^2\boldsymbol{k}_\parallel^2-2mE}}{2(\hbar^2\boldsymbol{k}_\parallel^2-2mE-\hbar^2\eta^2\boldsymbol{k}_\parallel^2-i\epsilon)}\Bigg).\end{aligned} \tag{4.3}$$

Equations (2.17), (4.1) and (4.3) imply that the density of states inside the interface at

$z = z_0$ is given by

$$\begin{aligned}\varrho(E, z_0) =& \frac{m}{\pi^2\hbar}\Theta(E)\int_0^{\sqrt{\frac{2mE}{\hbar^2}}} dk_\parallel k_\parallel \frac{\sqrt{2mE - \hbar^2 k_\parallel^2}}{2mE - \hbar^2 k_\parallel^2 + \hbar^2\eta^2 k_\parallel^2} \\ &+ \frac{m}{2\pi\hbar}\int_0^\infty dk_\parallel k_\parallel \Big[\delta\Big(\sqrt{\hbar^2 k_\parallel^2 - 2mE} - \hbar\eta k_\parallel\Big) + \delta\Big(\sqrt{\hbar^2 k_\parallel^2 - 2mE} + \hbar\eta k_\parallel\Big)\Big].\end{aligned} \tag{4.4}$$

Evaluating the integrals yields

$$\begin{aligned}\varrho(E, z_0) =& \frac{m}{\pi^2\hbar^2 L_\perp}\left(\frac{\Theta(E)}{(1-\eta^2)^{3/2}}\sqrt{\frac{2mEL_\perp^2}{\hbar^2}}\left(\sqrt{1-\eta^2} - \eta\arctan\left(\frac{\sqrt{1-\eta^2}}{\eta}\right)\right)\right. \\ &\left. + \frac{\pi\eta}{2|1-\eta^2|}\sqrt{\frac{2mEL_\perp^2}{\hbar^2(1-\eta^2)}}\Theta\left(\frac{2mE}{1-\eta^2}\right)\right), \\ =& \frac{\varrho_{d=3}(E)}{(1-\eta^2)^{3/2}}\left(\sqrt{1-\eta^2} - \eta\arctan\left(\frac{\sqrt{1-\eta^2}}{\eta}\right)\right) + \varrho_{d=2}(E/(1-\eta^2))\frac{\kappa}{2|1-\eta^2|},\end{aligned} \tag{4.5}$$

where $\kappa = \eta k_\parallel = \eta\sqrt{2mE/\hbar^2(1-\eta^2)}$ and $K_2 = E/(1-\eta^2)$ is the kinetic energy of particles whose wavefunctions are exponentially suppressed perpendicular to the interface. Integration of $\varrho(E, z_0)$ yields the relationship between particle density and Fermi Energy inside the interface,

$$\begin{aligned}n(z_0) =& \frac{1}{3\pi^2\sqrt{1-\eta^2}}\left(\frac{\sqrt{2mE_F}}{\hbar}\right)^3\left[1 - \frac{\eta}{1-\eta^2}\arctan\left(\frac{\sqrt{1-\eta^2}}{\eta}\right)\right] \\ &+ \frac{m\eta E_F}{3\pi\hbar^2|1-\eta^2|}\sqrt{\frac{2mE_F}{\hbar^2(1-\eta^2)}}, \\ =& \frac{n_3}{\sqrt{1-\eta^2}}\left[1 - \frac{\eta}{1-\eta^2}\arctan\left(\frac{\sqrt{1-\eta^2}}{\eta}\right)\right] + \frac{\kappa_F n_2}{3|1-\eta^2|},\end{aligned} \tag{4.6}$$

where $n_2$ and $n_3$ are the free particle density in two and three dimensions, and $\kappa_F = \eta\sqrt{2mE_F/\hbar^2(1-\eta^2)}$.

### 4.1.2 Analysis of free state and bound state density of states and electron density

Equation (4.5) indicates that electrons bound to the interface contribute a term proportional to the free two-dimensional density of states $\varrho_{d=2}(K_2)$, which is made dimensionally correct

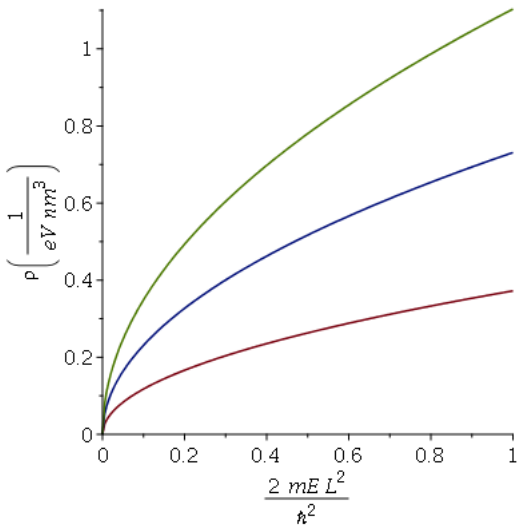


**Figure 4.1:** The relationship between density of states and energy. The $y$ axis represents the nonrelativistic density of states inside the interface at $z = z_0$ using $L_\perp = 0.3$ nm, $\alpha = 0.56 \times 10^{-1}$ eV nm and is plotted in units of $m/(\pi^2\hbar^2 L_\perp) = 4.43$ (eV nm$^3$)$^{-1}$. The green curve corresponds to the total density of states, while the blue(red) curve corresponds to the free(bound) state contribution respectively. The $x$ axis ranges from 0 to 1 according to $0 \leq 2mEL_\perp^2/\hbar^2 \leq 1$.

by the factor $\kappa$ as our system is three-dimensional and enumerates states per energy and per volume. In contrast to the bound states in the quantum well structure in Eq. (2.2), the bound states in the interface with RSOC are described by an inverse penetration depth which explicitly depends on the wavenumber for motion parallel to the interface. The requirement for bound states solutions ($\kappa > 0$) is therefore met for any value of $|\boldsymbol{k}_\parallel|$. The density of states and electron density inside the interface at $z = z_0$ are plotted in Figs. 4.1 and 4.2. Our results for the density of states (Eq. (4.5)) and the electron density (Eq. (4.6)) indicate that positive energy solutions are a linear combination of two-dimensional ($\eta^2 < 1$ bound states) and three-dimensional terms (free states). Increasing the RSOC strength increases the number of available states per unit energy. In the limit $\eta = 0, \kappa = 0$ in Eq. (4.5), the density of states and electron density in the interface approach the free three-dimensional value. The dispersion relation of the bound states in terms of $\eta$ is given by

$$E = \frac{\hbar^2}{2m}(k_\parallel^2 - \kappa^2) = \frac{\hbar^2 k_\parallel^2}{2m}(1 - \eta^2). \tag{4.7}$$

For $\eta^2 = 1$ the density of states in the interface has a van Hove singularity [62]. Inserting the bound state dispersion relation into Eq. (1.2) shows that when $\eta^2 = 1$, $|dE/dk_\parallel| =$

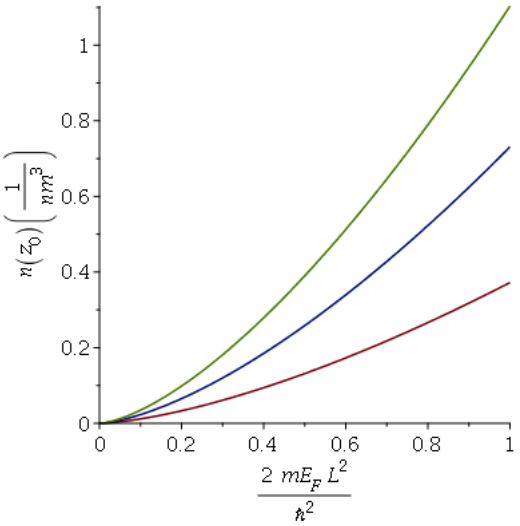


**Figure 4.2:** The relationship between electron density and Fermi energy. The $y$ axis represents the nonrelativistic electron density inside the interface at $z = z_0$ using $L_\perp = 0.3$ nm, $\alpha = 0.56 \times 10^{-1}$ eV nm and is plotted in units of $1/(3\pi^2 L_\perp^3) = 1.25$ nm$^{-3}$. The green curve corresponds to the total electron density, while the blue(red) curve corresponds to the free(bound) state contribution respectively. The $x$ axis ranges from 0 to 1 according to $0 \leq 2mE_F L_\perp^2/\hbar^2 \leq 1$.

$(\hbar^2 k_\parallel/m)(1-\eta^2) = 0$, confirming that $\eta^2 = 1$ yields a van Hove singularity in the density of states. The purely two-dimensional electron gas with RSOC analyzed in Ref. [25] contains spin-split minima in the dispersion relation at wave vectors $\boldsymbol{k}_{min}$ where $|\boldsymbol{k}_{min}| = k_{min} = \alpha m_*/\hbar^2$. The negative-energy density of states in Eq. (4.17) contains a van Hove singularity at $E_-(\boldsymbol{k}_{min}) = -\alpha^2 m_*/2\hbar^2$. Comparing this result with Eq. (4.7) shows that the van Hove singularity in the system with RSOC interface occurs when $\eta^2 = 1$ and does not depend on a particular value of $|\boldsymbol{k}_\parallel|$. However, in both the purely two-dimensional electron gas with RSOC and the current model under investigation, the van Hove singularities occur at the minimum allowed energy in the respective system. The RSOC strength ($\alpha$), can take a large range of values depending on the material. As an example, the Rashba coupling strength at the $LaAlO_3/SrTiO_3$ interface is $\approx 0.5 \times 10^{-11}$ eV m [39], while the strength for the topological insulator $Bi_2Se_3$ is $\approx 4 \times 10^{-10}$ eV m [63], a full two orders of magnitude larger. The RSOC strength in our model must satisfy $\alpha \leq \hbar^2/mL_\perp \leq 7.62 \times 10^{-11}$ eV m$^2/L_\perp$. Using $L_\perp = 0.3$ nm for the interface thickness consistent with Ref.[30], the RSOC strength must satisfy $\alpha \leq 2.54 \times 10^{-10}$ eV m in order for a ground state energy of the bound

states to exist. Figures 4.1,4.2 display the density of states and particle density respectively for $\alpha = 0.056$ eV nm and $L_\perp = 0.3$ nm. These parameters describe the RSOC strength of the surface Bi(111) and thickness of Bismuth layer deposited on a Ag substrate in Ref. [30].

## 4.2 Interdimensional system with RSOC plus effective mass interface

### 4.2.1 Results for interdimensional system with RSOC plus effective mass interface

Surfaces of materials as well as interfaces in heterostructures composed of metals, e.g. Bi/Ag interface, present physical systems in which electrons move with a different effective mass along the low-dimensional structure compared to bulk motion. In this section we will derive results for the density of states at the location of the low-dimensional structure using both the Green function method and wavefunction method. This will be the first situation in which analyzing the problem using the wavefunction method (described in Sec. 2.2.3) is helpful in understanding the origin of a divergence which occurs in the free state density of states. Referencing Appendix A, the energy-dependent Green function in the $\boldsymbol{x}$ representation is found in the form of a Hankel transform,

$$\langle \boldsymbol{x}|G(E)|\boldsymbol{x'}\rangle = \frac{1}{2\pi}\int_0^\infty dk_\parallel k_\parallel J_0(k_\parallel|\boldsymbol{x}-\boldsymbol{x}'_\parallel|)\langle z|G(E,\boldsymbol{k}_\parallel)|z'\rangle, \tag{4.8}$$

where

$$\begin{aligned}\langle z|G(E,\boldsymbol{k}_\parallel)|z'\rangle = {} & \frac{i\hbar\Theta(\gamma)}{2\sqrt{\gamma}}\exp\left(i\sqrt{\gamma}|z-z'|/\hbar\right)\overleftrightarrow{1} + \frac{\hbar\Theta(\beta)}{2\sqrt{\beta}}\exp\left(-\sqrt{\beta}|z-z'|/\hbar\right)\overleftrightarrow{1} \\ & + \left[\frac{i\hbar\Theta(\gamma)}{2\sqrt{\gamma}}\exp\left(i\sqrt{\gamma}|z-z_0|/\hbar\right) + \frac{\hbar\Theta(\beta)}{2\sqrt{\beta}}\exp\left(-\sqrt{\beta}|z-z_0|/\hbar\right)\right]Q(E,\boldsymbol{k}_\parallel,z')\end{aligned} \tag{4.9}$$

with $Q(E,\boldsymbol{k}_\parallel,z')$ defined in Appendix A and $\gamma = 2mE - \hbar^2\boldsymbol{k}_\parallel^2$, $\beta = \hbar^2\boldsymbol{k}_\parallel^2 - 2mE$. Applying $z = z' = z_0$ and taking the trace yields

$$\begin{aligned}\mathrm{Tr}[\langle z_0|G(E,\boldsymbol{k}_\parallel)|z_0\rangle] =& \frac{4i\hbar\sqrt{\gamma}\Theta(\gamma)\Big[4\gamma + \hbar^2\boldsymbol{k}_\parallel^2\Big[\Big(\frac{m}{\mu}\Big)^2\boldsymbol{k}_\parallel^2 + \Big(\frac{2\alpha m L_\perp}{\hbar^2}\Big)^2\Big]\Big]}{\Big(4\gamma + \hbar^2\boldsymbol{k}_\parallel^2\Big[\Big(\frac{m}{\mu}\Big)^2\boldsymbol{k}_\parallel^2 + \Big(\frac{2\alpha m L_\perp}{\hbar^2}\Big)^2\Big]\Big)^2 - 4\hbar^4\boldsymbol{k}_\parallel^6\Big(\frac{m}{\mu}\Big)^2\Big(\frac{2\alpha m L_\perp}{\hbar^2}\Big)^2} \\ &+ \frac{4\hbar\Theta(\beta)\Big(\Big(\frac{m\hbar}{2\mu}\Big)\boldsymbol{k}_\parallel^2 + \sqrt{\beta}\Big)}{4\beta + \hbar^2\boldsymbol{k}_\parallel^2\Big[\Big(\frac{m}{\mu}\Big)^2\boldsymbol{k}_\parallel^2 - \Big(\frac{2\alpha m L_\perp}{\hbar^2}\Big)^2\Big] + 4\hbar\boldsymbol{k}_\parallel^2\sqrt{\beta}\Big(\frac{m}{\mu}\Big) - i\epsilon}.\end{aligned} \tag{4.10}$$

Equations (2.17), (4.8) and (4.10) imply that the density of states inside the interface at $z = z_0$ is given by

$$\begin{aligned}\varrho(E,z_0) =& \frac{m}{\pi^2\hbar}\int_0^{\sqrt{\frac{2mE}{\hbar^2}}} dk_\parallel k_\parallel \frac{4\sqrt{\gamma}\Theta(\gamma)\Big[4\gamma + \hbar^2 k_\parallel^2\Big[\Big(\frac{m}{\mu}\Big)^2 k_\parallel^2 + \Big(\frac{2\alpha m L_\perp}{\hbar^2}\Big)^2\Big]\Big]}{\Big(4\gamma + \hbar^2 k_\parallel^2\Big[\Big(\frac{m}{\mu}\Big)^2 k_\parallel^2 + \Big(\frac{2\alpha m L_\perp}{\hbar^2}\Big)^2\Big]\Big)^2 - 4\hbar^4 k_\parallel^6\Big(\frac{m}{\mu}\Big)^2\Big(\frac{2\alpha m L_\perp}{\hbar^2}\Big)^2} \\ &+ \frac{m}{2\pi^2\hbar}\int_0^\infty dk_\parallel k_\parallel \Theta(\beta)\Im\left[\frac{\sqrt{\beta} + \hbar\kappa_+}{\beta - \hbar^2\kappa_+^2 - i\epsilon} + \frac{\sqrt{\beta} + \hbar\kappa_-}{\beta - \hbar^2\kappa_-^2 - i\epsilon}\right],\end{aligned} \tag{4.11}$$

where $\kappa_\pm = -\ell k_\parallel^2 \pm \eta k_\parallel$ and $\ell \equiv m/2\mu$, $\eta = m\alpha L_\perp/\hbar^2$. The $\gamma$- and $\beta$-dependent terms in Eq. (4.11) represent the free and bound state contributions to the density of states, respectively. For clarity we will analyze the free and bound state contributions separately in the following sections.

### 4.2.2 Analysis of free state contribution to the density of states in Eq. (4.11)

Using the substitutions $\ell \equiv m/2\mu$, $\eta = m\alpha L_\perp/\hbar^2$ and $y = k_\parallel^2\ell^2$ in Eq. (4.11) yields

$$\varrho(E,z_0) = \frac{m}{2\pi^2\hbar^2\ell}\int_0^{\frac{2mE\ell^2}{\hbar^2}} dy \frac{\sqrt{2mE\ell^2/\hbar^2 - y}\Big[2mE\ell^2/\hbar^2 + y\Big(\eta^2 - 1\Big) + y^2\Big]}{\Big[2mE\ell^2/\hbar^2 + y\Big(\eta^2 - 1\Big) + y^2\Big]^2 - 4y^3\eta^2}. \tag{4.12}$$

Numerical integration of Eq. (4.12) given the inequality $0 \leq 2mE\ell^2/\hbar^2 \leq 1$ yields the interdimensional density of states in the interface at $z = z_0$ from free states and is plotted in Fig. 4.3. Figure 4.3 shows that the density of states inside the interface contains a singularity

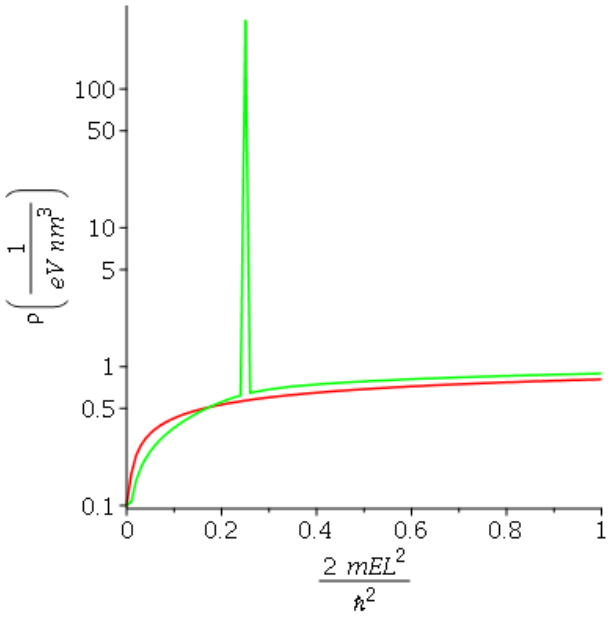


**Figure 4.3:** The density of states inside the interface at $z = z_0$ in units of $m/(2\pi^2\hbar^2\ell)$ for $\ell = 40$ nm in a logarithmic scale. The red curve represents the density of states for $\eta = 0$ while the green line is the density of states for $\eta = 0.5$. The peak value in the density of states with RSOC present corresponds to $2mE\ell^2/\hbar^2 = \eta^2 = y$ in the numerical integration. The $x$ axis ranges from 0 to 1 according to $0 \leq 2mE\ell^2/\hbar^2 \leq 1$.

when $2mE\ell^2/\hbar^2 = \eta^2 = k_\parallel^2\ell^2$. The origin of the singularity can most easily be seen by calculating the density of states using Eq. (2.34), along with the free state wavefunction corresponding to Eq. (3.20),

$$\psi_{\boldsymbol{k}_\parallel,k_\perp,+}(\boldsymbol{x}_\parallel,z)_\pm = \langle \boldsymbol{x}_\parallel, z|\boldsymbol{k}_\parallel,k_\perp,+\rangle_\pm = \frac{\exp(i\boldsymbol{k}_\parallel\cdot\boldsymbol{x}_\parallel)}{2\sqrt{\pi^3}\sqrt{1+(m\alpha L_\perp/\hbar^2k_\perp)^2(A\boldsymbol{k}_\parallel^2 \pm |\boldsymbol{k}_\parallel|)^2}}$$
$$\times\left(\cos(k_\perp(z-z_0)) + \frac{m\alpha L_\perp}{\hbar^2k_\perp}(A\boldsymbol{k}_\parallel^2 \pm |\boldsymbol{k}_\parallel|)\sin(k_\perp|z-z_0|)\right)\varphi_\mp(\boldsymbol{k}_\parallel). \tag{4.13}$$

At the location of the interface at $z = z_0$ the free state contribution to the density of states can be shown to yield the identical result to Eq. (4.11) by replacing the factor of 2 for spin in Eq. (2.34) with a sum over eigenspinors:

$$\varrho(E,\boldsymbol{x}) = \int d^2\boldsymbol{k}_\parallel \Theta(E-(\hbar^2\boldsymbol{k}_\parallel^2/2m))\frac{\partial k_\perp(E,\boldsymbol{k}_\parallel)}{\partial E}\sum_\pm |\langle\boldsymbol{x}|\boldsymbol{k}_\parallel,k_\perp,+\rangle_\pm|^2\Big|_{k_\perp=k_\perp(E,\boldsymbol{k}_\parallel)}. \tag{4.14}$$

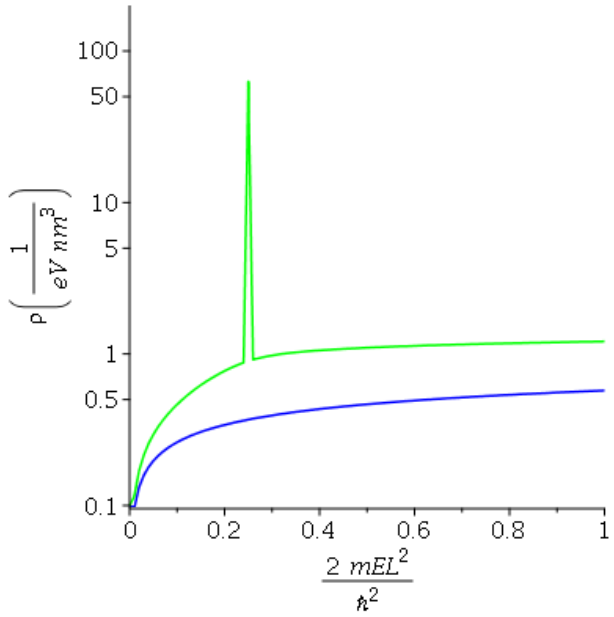


**Figure 4.4:** The density of states inside the interface at $z = z_0$ in units of $m/(2\pi^2\hbar^2\ell)$ for $\ell = 40$ nm in a logarithmic scale. The green line represents the $E_-$ contribution to the density of states, while the blue line is the $E_+$ contribution to the density of states for $\eta = 0.5$. The peak value in the $E_-$ contribution to the density of states with spin-orbit coupling present corresponds to $2mE\ell^2/\hbar^2 = \eta^2 = y$ in the numerical integration, Eq. (4.19). The $x$ axis ranges from 0 to 1 according to $0 \leq 2mE\ell^2/\hbar^2 \leq 1$.

Insertion of Eq. (4.13) into Eq. (4.14) yields

$$\varrho(E, z_0) = \frac{m}{2\pi^2\hbar^2}\int_0^{\sqrt{2mE}/\hbar} dk_\parallel k_\parallel \left( \frac{\sqrt{2mE/\hbar^2 - k_\parallel^2}}{2mE/\hbar^2 - k_\parallel^2 + (m\alpha L_\perp/\hbar^2)^2(Ak_\parallel^2 + k_\parallel)^2} + \frac{\sqrt{2mE/\hbar^2 - k_\parallel^2}}{2mE/\hbar^2 - k_\parallel^2 + (m\alpha L_\perp/\hbar^2)^2(Ak_\parallel^2 - k_\parallel)^2} \right). \tag{4.15}$$

For the strictly two-dimensional electron gas with Rashba spin-orbit coupling and kinetic energy with effective mass $m_*$, the dispersion relation is given by [25, 27]

$$E_\pm(k_\parallel) = \frac{\hbar^2 k_\parallel^2}{2m_*} \pm \alpha k_\parallel. \tag{4.16}$$

The corresponding density of states in this system is given by [27]

$$\begin{aligned} \varrho(E_\pm(k_\parallel)) &= \frac{m_*}{2\pi\hbar^2}\left(1 \mp \frac{\beta}{\sqrt{\beta^2 + 2Em_*/\hbar^2}}\right), E \geq 0, \\ \varrho(E_-(k_\parallel)) &= \frac{m_*\beta}{\pi\hbar^2\sqrt{\beta^2 + 2m_*E/\hbar^2}}, E < 0, \end{aligned} \tag{4.17}$$

where $\beta = m_*\alpha/\hbar^2$. Of particular interest is the existence of a van Hove singularity in $\varrho(E_-(k_\parallel))$. The free state density of states can be written in terms of the two-dimensional dispersion relation,

$$\varrho(E,z_0) = \frac{m}{2\pi^2\hbar^2}\int_0^{\sqrt{2mE}/\hbar} dk_\parallel k_\parallel \left( \frac{\sqrt{2mE/\hbar^2 - k_\parallel^2}}{2mE/\hbar^2 - k_\parallel^2 + (mL_\perp/\hbar^2)^2(E_+(k_\parallel))^2} + \frac{\sqrt{2mE/\hbar^2 - k_\parallel^2}}{2mE/\hbar^2 - k_\parallel^2 + (mL_\perp/\hbar^2)^2(E_-(k_\parallel))^2} \right). \tag{4.18}$$

The term which includes $E_-(k_\parallel)$ in Eq. (4.18) also yields a singularity for the same condition as in Eq. (4.11). The free state density of states at the location of the interface is plotted in Figure 4.4 where we have separated the terms depending on $E_+ = E_+(k_\parallel)$ and $E_- = E_-(k_\parallel)$. The dimensionless integral numerically evaluated is

$$\varrho(E,z_0) = \frac{m}{2\pi^2\hbar^2\ell}\int_0^{2mE\ell^2/\hbar^2} dy \left( \frac{\sqrt{2mE\ell^2/\hbar^2 - y}}{2mE\ell^2/\hbar^2 - y + (y + \eta\sqrt{y})^2} + \frac{\sqrt{2mE\ell^2/\hbar^2 - y}}{2mE\ell^2/\hbar^2 - y + (y - \eta\sqrt{y})^2} \right). \tag{4.19}$$

The origin of the singularity comes from the factor $\partial k_\perp/\partial E \sim 1/k_\perp$ in Eq. (4.14), due to the divergence at $k_\perp = 0$. This shows that the singularity has a van Hove type origin. However, the divergence does not generically generate a singularity in $\varrho(E,z_0)$ because the sum over wavefunctions squared in Eq. (4.14) vanishes sufficiently fast for $k_\perp = 0$. A special situation occurs when $Ak_\parallel^2 - k_\parallel = 0$ in the $|\langle \boldsymbol{x}_\parallel, z|\boldsymbol{k}_\parallel, k_\perp = 0, +\rangle_-|^2$ term in Eq. (4.14). When this occurs, the sum over wavefunctions squared no longer vanishes for $k_\perp = 0$, and therefore cannot compensate for the divergence from the $\partial k_\perp/\partial E$ factor. This results in a van Hove type singularity for the condition $Ak_\parallel = A\sqrt{2mE/\hbar^2} = 1$. Inserting $A = \hbar^2/(2\mu\alpha L_\perp)$ into the condition shows that the van Hove type singularity occurs for $k_\parallel^2\ell^2 = 2mE\ell^2/\hbar^2 = \eta^2$, which is the previously noted condition for the singularity. Figure 4.3 shows that the free state density of states inside the interface behaves like the interdimensional system studied in Ref. [58] with the addition of the van Hove type singularity. The density of states in Figs. 4.3,4.4 are displayed for general parameter values of $\eta = 0.5$ and $\eta = 0.2$ respectively.

### 4.2.3 Analysis of bound state contribution to the density of states in Eq. (4.11)

In order to analyze the bound state contribution, we will compare the calculation for the density of states using Eqs. (2.17,2.34). We can calculate the bound state contribution to the density of states inside the interface ($E < \hbar^2 k_\parallel^2/2m, \kappa > 0$) by using the bound state wavefunction corresponding to Eq. (3.20),

$$\psi_{\boldsymbol{k}_\parallel,\kappa,+}(\boldsymbol{x}_\parallel, z) = \langle \boldsymbol{x}_\parallel, z|\boldsymbol{k}_\parallel, \kappa, +\rangle = \frac{\exp(i\boldsymbol{k}_\parallel \cdot \boldsymbol{x}_\parallel)}{2\pi}\sqrt{\frac{\kappa}{2|\boldsymbol{k}_\parallel|}}\begin{pmatrix}\sqrt{k_y + ik_x}\\ \mp\sqrt{k_y - ik_x}\end{pmatrix}\exp(-\kappa|z - z_0|), \tag{4.20}$$

where

$$E = \frac{\hbar^2}{2m}(\boldsymbol{k}_\parallel^2 - \kappa^2) = \frac{\hbar^2 k_\parallel^2}{2m}\left(1 - \left(-\frac{m|\boldsymbol{k}_\parallel|}{2\mu} + \frac{m|\alpha|L_\perp}{\hbar^2}\right)^2\right) \tag{4.21}$$

and

$$\kappa = -\frac{m\boldsymbol{k}_\parallel^2}{2\mu} + \frac{m|\alpha|L_\perp|\boldsymbol{k}_\parallel|}{\hbar^2}. \tag{4.22}$$

Equation (4.22) limits the range of values that $|\boldsymbol{k}_\parallel| = k_\parallel$ can requiring that $\kappa > 0$. Using $\eta = m|\alpha|L_\perp/\hbar^2$, $\ell = m/2\mu$ for brevity, $k_\parallel$ must satisfy $\eta/\ell > k_\parallel$ in order for a bound state to exist. In order for a ground state energy to exist, we require that

$$1 - \left(-\frac{m|\boldsymbol{k}_\parallel|}{2\mu} + \frac{m|\alpha|L_\perp}{\hbar^2}\right)^2 \geq 0, \tag{4.23}$$

otherwise $E \to -\infty$ as $|\boldsymbol{k}_\parallel| \to \infty$. The bound state contribution to the density of states can be calculated using

$$\varrho(E, \boldsymbol{x}) = \sum_\pm \int_0^{2\pi} d\varphi k_\parallel \frac{\partial k_\parallel(E, \kappa_\pm)}{\partial E}|\langle \boldsymbol{x}|\boldsymbol{k}_\parallel, \kappa_\pm\rangle|^2\Big|_{\boldsymbol{k}_\parallel = k_\parallel(E,\kappa_\pm)}, \tag{4.24}$$

where we have substituted a sum over eigenspinors (with corresponding eigenvalues $\kappa_\pm = -\ell k_\parallel^2 \pm \eta k_\parallel$) for the factor of 2 for spin in Eq. (2.34). However, the eigenspinor which corresponds to $\kappa_-$ cannot be included in the calculation of the density of states because $\kappa_- < 0$ which does not correspond to a bound state solution. Inserting Eq. (4.20) into

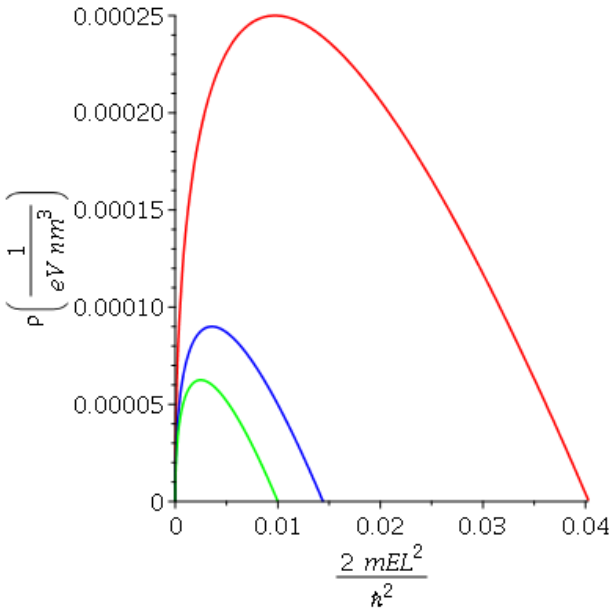


**Figure 4.5:** The density of states inside the interface at $z = z_0$ corresponding to Eq. (4.25) in units of $m/(\pi\hbar^2\ell)$ for $\ell = 40$ nm. The red, blue and green curves correspond to $\eta = 0.2$, $\eta = 0.12$ and $\eta = 0.1$ respectively. The $x$ axis range for each curve adheres to $0 \leq 2mE\ell^2/\hbar^2 \leq \eta^2$.

Eq. (4.24) and using $z = z_0$ yields the bound state contribution to the density of states at the location of the interface,

$$\begin{aligned}\varrho(E, z_0) &= \frac{mk_\parallel(\eta - k_\parallel\ell)\Theta(\eta/\ell - k_\parallel)\Theta(\hbar^2k_\parallel^2)}{2\pi\hbar^2|1 - \eta^2 - 2\ell^2k_\parallel^2 + 3k_\parallel\ell\eta|}\Big|_{k_\parallel = k_\parallel(E)} \\ &= \frac{\varrho_{d=2}(K_2)\kappa(k_\parallel(E))}{2|1 - \eta^2 - 2\ell^2k_\parallel^2 + 3k_\parallel\ell\eta|},\end{aligned} \tag{4.25}$$

where $K_2$ is the kinetic energy of electrons whose wavefunction is exponentially suppressed to motion perpendicular to the interface. Unlike the situation with a pure RSOC interface, a solution for $k_\parallel(E)$ is not straightforward due to the fourth order polynomial in $k_\parallel$ that results from the bound state dispersion relation

$$E = \frac{\hbar^2k_\parallel^2}{2m} - \frac{\hbar^2}{2m}(-\ell k_\parallel^2 + \eta k_\parallel)^2. \tag{4.26}$$

Using the Green function method we can arrive at the same expression as Eq. (4.25). The bound state contribution to the density of states inside the interface using the Green function

method yields

$$\varrho(E,z_0)=\frac{m}{2\pi^2\hbar^2}\int_0^\infty dk_\parallel(\hbar k_\parallel)\Theta(\beta)\Im\left[\frac{\sqrt{\beta}+\hbar\kappa_+}{\beta-\hbar^2\kappa_+^2-i\epsilon}+\frac{\sqrt{\beta}+\hbar\kappa_-}{\beta-\hbar^2\kappa_-^2-i\epsilon}\right], \tag{4.27}$$

where $\kappa_\pm=-\ell k_\parallel^2\pm\eta k_\parallel$, $\ell=m/2\mu$ and $\eta=m\alpha L_\perp/\hbar^2$. We can evaluate the integral using the Sokhotsky-Plemelj relation and the identity,

$$\delta(f(k_\parallel))=\sum_i\frac{1}{|f'(k_{\parallel_i})|}\delta(k_\parallel-k_{\parallel_i}). \tag{4.28}$$

Omitting the contribution to the density of states inside the interface from the term which depends on $\kappa_-$ yields again the result in Eq. (4.25). The summation in Eq. (4.28) is over values of $k_\parallel$ such that $\hbar^2k_\parallel^2-2mE-\hbar^2(-\ell k_\parallel^2+\eta k_\parallel)^2=0$. Appendix C details the approximation to arrive at a solution for $k_\parallel(E)$ given by

$$\begin{aligned}k_\parallel(E)=&\sqrt{\left[\frac{1-\eta^2-\sqrt{(1-\eta^2)^2-4g(E,\ell)}}{2\ell^2}\right]\left[1+\frac{\eta^2}{2}\frac{1-\eta^2-\sqrt{(1-\eta^2)^2-4g(E,\ell)}}{(1-\eta^2)^2-4g(E,\ell)}\right]}\\&-\frac{\eta}{\ell}\frac{1-\eta^2-\sqrt{(1-\eta^2)^2-4g(E,\ell)}}{2\sqrt{(1-\eta^2)^2-4g(E,\ell)}},\end{aligned} \tag{4.29}$$

where $g(E,\ell)=2mE\ell^2/\hbar^2$. The bound state density of states is plotted in Fig. 4.5 for three different values of $\eta$ and $\ell=40$ nm. As can be seen in Fig. 4.5, the bound state density of states increases for larger values of $\eta=m\alpha L_\perp/\hbar^2$. For a constant interface thickness $L_\perp$, this indicates that for an interface with larger RSOC coefficient $\alpha$ there are more states available per unit energy. Evaluating $\partial\varrho(E,z_0)/\partial E=0$ numerically for each curve in Fig. 4.5 shows that the peak value for the density of states occurs at $E=\eta^2/4$. Like the pure RSOC system, the bound state density of states in this system are proportional to the free two-dimensional density of states multiplied by an energy dependent bound state wavenumber. The nonrelativistic system with effect mass interface discussed in Ref. [58] does not contain a bound state contribution to the density of states, and therefore we do not have results to compare with from this sytem. In the limit $L_\perp\to0$, the bound states density of states vanishes as expected. The bound state contribution to the density of states comes to zero at the maximum value $k_\parallel=\eta/\ell$. As we have seen, the free state density of states contains a van Hove singularity at this value of $k_\parallel$. In our discussion of bound state and free state density of states in the following section, we will see a second example of this behaviour.

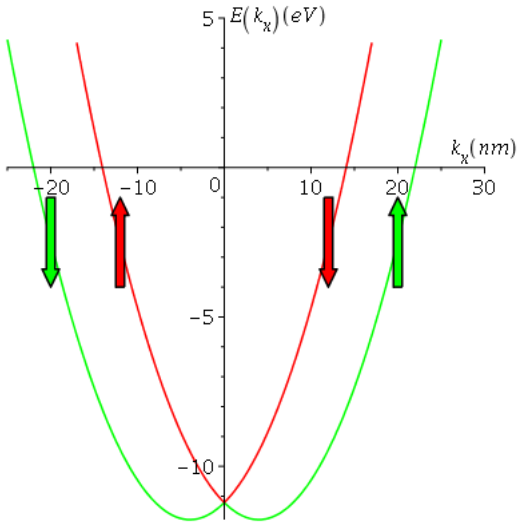


**Figure 4.6:** The spin-split bound state dispersion relation for $\alpha = 0.056$ eV nm, $V_0 = 4.36$ eV and $L_\perp = 0.3$ nm for $k_y = 0$. The red(green) curve corresponds to $E_-(E_+)$ in Eq. (3.25) with a minimum energy of $E_{min} = -mV_0^2L_\perp^2/2\hbar^2(1-\eta^2)$ where $\eta = m\alpha L_\perp/\hbar^2$.

## 4.3 Interdimensional system with RSOC plus attractive potential interface

### 4.3.1 Bound state dispersion relation and enhanced Edelstein effect

Extending the two-dimensional model for an electron gas subject to RSOC, [25], to a three-dimensional model in which electrons are bound to a two-dimensional interface or surface with RSOC through a confining potential affects the well known Edelstein effect (and inverse Edelstein effect) [21] through the restriction $\kappa_- > 0$. Consider a two-dimensional system with RSOC in the $(x, y)$-plane. As discussed in Sec. 1.3, the Edelstein effect [21] describes how an applied electric field $\varepsilon(x)$ along a surface or interface induces a net spin-polarization in the $y$-direction from electrons moving along the surface or interface. In the purely two-dimensional system with RSOC [25], Eq. (1.1) and Fig. 1.1 describes the spin-split energy branches for electrons with spin alignment $-y(+y)$ for $E_+(E_-)$, $k_x > 0$ and vice versa for $k_x < 0$ respectively.

An applied electric field along the $+x$-direction causes electrons to move in the $-x$-direction and populates states with $k_x < 0$ at the expense of states with $k_x > 0$. The net effect of this changing population of occupied states is a net $-y$ spin polarization coming from the $E_-$ branch playing the major role [23]. There is no restriction on the energy that these states can have in the purely two-dimensional model. Eq. (3.25) describes the spin-split energy branches of the three-dimensional model under investigation, and is displayed in Fig. 4.6. Please note that in the three-dimensional model, the inner(outer) curve in Fig. 4.6 corresponds to the $E_-(E_+)$ branch which is opposite to Fig. 1.1. The requirement $\kappa_- > 0$ implies $k_\parallel < V_0/\alpha$ in order for a bound state solution to exist. This restricts the energy $E_-$ in Eq. (3.25) to a maximum value of $E_- = \hbar^2 V_0^2/2m\alpha^2$, displayed by the blue horizontal line in Fig. 4.7. Applying an electric field $\varepsilon(x)$ along the interface in the three-dimensional model results in a net spin-polarization in the $-y$-direction due to the Edelstein effect. Most importantly, however, is that states belonging to $E_-$ can only be populated up to a maximum energy of $\hbar^2 V_0^2/2m\alpha^2$. The contribution to the net spin polarization from the increase in $+y$ spin alignment in the $k_x < 0$ region of the $E_-$ branch therefore has a maximum value. Figure 4.7 displays the bound state dispersion for the spin-split energy branches when the Fermi energy $E_F$ is at the maximum allowed energy in the $E_-$ branch. Figure 4.8 displays the effect of applying an electric field along the $+x$-direction. Electrons move along the $-x$-direction and populate states with $k_x < 0$. Due to the constraint in the $E_-$ branch, up-spin electrons cannot be depopulated from states with $k_x > 0$ because the corresponding up-spin states with $k_x < 0$ are already at the maximum allowed energy and thus fully occupied. The $E_+$ branch has no restriction on energy owing to $\kappa_+ > 0\ \forall k_\parallel$. This implies that down-spin electron states with $k_x > 0$ can be depopulated in order to populate states with $k_x < 0$. This results in a larger net spin polarization in the $-y$-direction than in the purely two-dimensional model, and results in an enhanced Edelstein effect. For comparison with the purely two-dimensional model, Fig. 4.9 shows the effect of an applied electric field along the $+x$-direction on the Fermi circles corresponding to the spin-split branches. Interestingly, the shape of the Fermi surfaces in the $(k_x, k_y)$-plane is elliptical. The Fermi surface corresponding to the $E_+$ branch (green circle) inflates in the $k_x < 0$ (olive curve) without any change to the $k_x > 0$ portion of the Fermi surface. This inflation of states corresponds to the shrinking of the

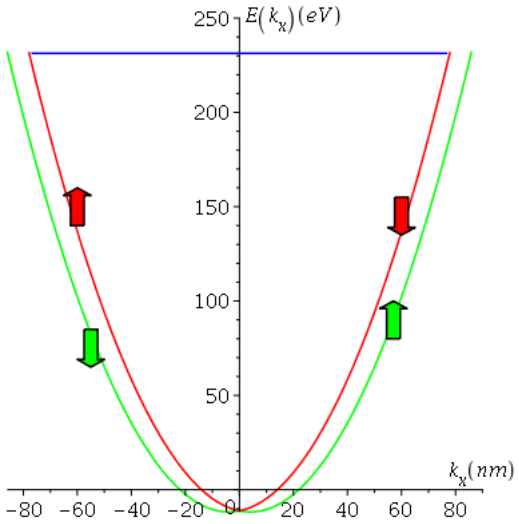


**Figure 4.7:** The spin-split bound state dispersion relation for $\alpha = 0.056$ eV nm, $V_0 = 4.36$ eV and $L_\perp = 0.3$ nm for $k_y = 0$. The red(green) curve corresponds to $E_-(E_+)$ in Eq. (3.25). Due to the requirement $\kappa_- > 0$ the $E_-$ energy branch is restricted to a maximum energy of $\hbar^2 V_0^2/2m\alpha^2$, indicated by the blue line.

Fermi surface from the $E_-$ branch (red circle) as states are depopulated for $k_x > 0$ (maroon curve) with no change in the surface for $k_x < 0$. The inverse Edelstein effect is also enhanced in the three-dimensional model under consideration. Injection of spin-up electrons through spin-pumping [23] in the situation displayed in Fig. 4.7 indicates that electrons entering the interface must occupy states in the $k_x > 0$ region of the $E_+$ branch. Inflating the Fermi surface corresponding to the $E_+$ branch yields a larger net current in the $+x$-direction than in the purely two-dimensional model discussed in Sec. 1.3.

### 4.3.2 Calculation of bound state density of states at $z = z_0$

The energy-dependent Green function in the $\boldsymbol{x}$ representation is found in Appendix A in the form of Hankel transform,

$$\langle \boldsymbol{x}|G(E)|\boldsymbol{x'}\rangle = \frac{1}{2\pi}\int_0^\infty dk_\parallel k_\parallel J_0(k_\parallel|\boldsymbol{x}-\boldsymbol{x}'_\parallel|)\langle z|G(E,\boldsymbol{k}_\parallel)|z'\rangle, \tag{4.30}$$

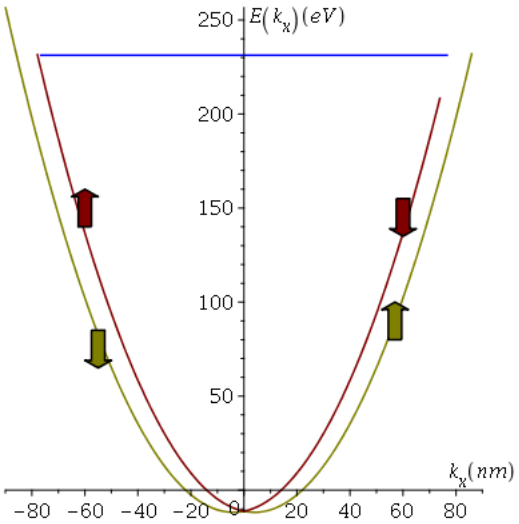


**Figure 4.8:** The spin-split bound state dispersion relation for $\alpha = 0.056$ eV nm, $V_0 = 4.36$ eV and $L_\perp = 0.3$ nm for $k_y = 0$ with an applied electric field $\boldsymbol{E} = \varepsilon\hat{x}$. The maroon(olive) curve corresponds to $E_-(E_+)$ in Eq. (3.25) with $k_x < 0$ states populated at the expence of $k_x > 0$ states. Due to the requirement $\kappa_- > 0$ the $E_-$ energy branch is restricted to a maximum energy of $\hbar^2 V_0^2/2m\alpha^2$, indicated by the blue line, which prevents $+y$-spin states from being adjusted due to the electric field.

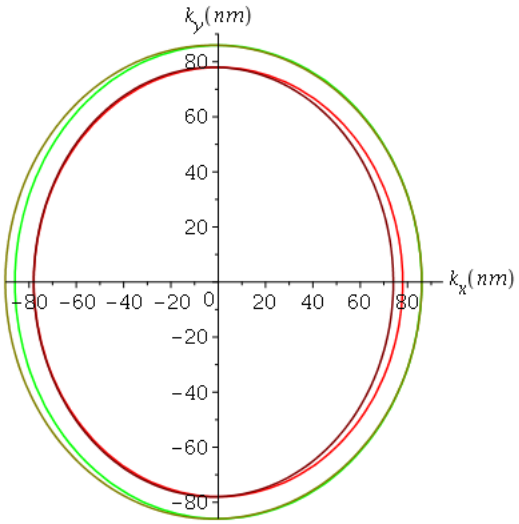


**Figure 4.9:** Shifting of the Fermi circles in the presence of an applied electric field $\boldsymbol{E} = \varepsilon\hat{x}$. $k_x > 0$ states are depopulated from the $E_-$ branch (red to maroon) and populated in the $E_+$ branch for $k_x < 0$ (green to olive) due to the enhanced EE.

where

$$\langle z|G(E,\boldsymbol{k}_\parallel)|z'\rangle = \frac{i\hbar\Theta(\gamma)}{2\sqrt{\gamma}}\exp\left(i\sqrt{\gamma}|z-z'|/\hbar\right)\overleftrightarrow{1} + \frac{\hbar\Theta(\beta)}{2\sqrt{\beta}}\exp\left(-\sqrt{\beta}|z-z'|/\hbar\right)\overleftrightarrow{1}$$
$$+\left[\frac{i\hbar\Theta(\gamma)}{2\sqrt{\gamma}}\exp\left(i\sqrt{\gamma}|z-z_0|/\hbar\right) + \frac{\hbar\Theta(\beta)}{2\sqrt{\beta}}\exp\left(-\sqrt{\beta}|z-z_0|/\hbar\right)\right]Q(E,\boldsymbol{k}_\parallel,z') \quad (4.31)$$

with $Q(E,\boldsymbol{k}_\parallel,z')$ defind in Appendix A and $\gamma = 2mE - \hbar^2\boldsymbol{k}_\parallel^2$, $\beta = \hbar^2\boldsymbol{k}_\parallel^2 - 2mE$. However, in our discussion of the results for bound and free state density of states, we will specifically use the wavefunction method. The bound state contribution to the density of states at the location of the interface can be calculated using

$$\varrho(E,\boldsymbol{x}) = \sum_{\pm}\int_0^{2\pi} d\varphi k_\parallel \left|\frac{\partial k_\parallel(E,\kappa_\pm)}{\partial E}\right| |\langle \boldsymbol{x}|\boldsymbol{k}_\parallel,\kappa_\pm\rangle|^2\Big|_{\boldsymbol{k}_\parallel = k_\parallel(E,\kappa_\pm)}. \quad (4.32)$$

Equation (3.25) is quadratic in $k_\parallel$ yielding two possible solutions for the $E_+$ and $E_-$ energy branches. Figure 4.6 shows the spin-split dispersion relation for $k_y = 0$. To calculate the bound state density of states we must find solutions to Eq. (3.25) for $E_+$ and $E_-$ separately. Figure 4.10 shows the spin split dispersion relation in terms of $k_\parallel = |\boldsymbol{k}_\parallel|$ with a minimum energy of $E_{min} = -mV_0^2L_\perp^2/2\hbar^2(1-\eta^2)$ where $\eta = m\alpha L_\perp/\hbar^2$. The two solutions to

$$E_- = \frac{\hbar^2}{2m}(\boldsymbol{k}_\parallel^2 - \kappa_-^2) = \frac{\hbar^2k_\parallel^2}{2m} - \frac{mL_\perp^2}{2\hbar^2}(V_0 - \alpha k_\parallel)^2$$
$$0 = \left(\frac{\hbar^2}{2m} - \frac{m\alpha^2L_\perp^2}{2\hbar^2}\right)k_\parallel^2 + \frac{mV_0\alpha L_\perp^2}{\hbar^2}k_\parallel - \left(\frac{mV_0^2L_\perp^2}{2\hbar^2} + E\right), \quad (4.33)$$

are

$$k_\parallel(E_-) = \frac{-mV_0\alpha L_\perp^2/\hbar^2 \pm \sqrt{f(E,\eta,V_0)}}{(\hbar^2/m)(1-\eta^2)}, \quad (4.34)$$

where $f(E,\eta,V_0) = V_0^2L_\perp^2 + (2E\hbar^2/m)(1-\eta^2)$. Requiring positive solutions to $k_\parallel(E_-)$ eliminates the negative sign choice in the $\pm$ term and restricts the energy to $E \geq -mV_0^2L_\perp^2/2\hbar^2$. Therefore for $E_-$ we have

$$k_\parallel(E_-) = \frac{-mV_0\alpha L_\perp^2/\hbar^2 + \sqrt{f(E,\eta,V_0)}}{(\hbar^2/m)(1-\eta^2)}. \quad (4.35)$$

The solutions to

$$E_+ = \frac{\hbar^2}{2m}(\boldsymbol{k}_\parallel^2 - \kappa_+^2) = \frac{\hbar^2k_\parallel^2}{2m} - \frac{mL_\perp^2}{2\hbar^2}(V_0 + \alpha k_\parallel)^2$$
$$0 = \left(\frac{\hbar^2}{2m} - \frac{m\alpha^2L_\perp^2}{2\hbar^2}\right)k_\parallel^2 - \frac{mV_0\alpha L_\perp^2}{\hbar^2}k_\parallel - \left(\frac{mV_0^2L_\perp^2}{2\hbar^2} + E\right), \quad (4.36)$$

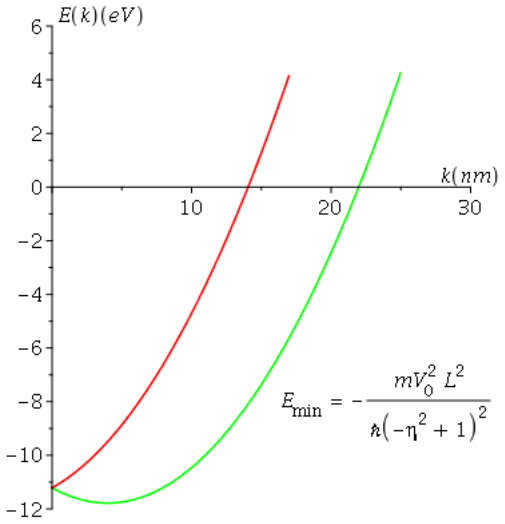


**Figure 4.10:** The spin-split bound state dispersion relation for $\alpha = 0.056$ eV nm, $V_0 = 4.36$ eV and $L_\perp = 0.3$ nm in terms of $k \equiv k_\parallel = |\boldsymbol{k}_\parallel|$. The red(green) curve corresponds to $E_-(E_+)$ in Eq. (3.25) with a minimum energy of $E_{min} = -mV_0^2 L_\perp^2/2\hbar^2(1-\eta^2)$ where $\eta = m\alpha L_\perp/\hbar^2$.

are

$$k_\parallel(E_+) = \frac{mV_0\alpha L_\perp^2/\hbar^2 \pm \sqrt{f(E,\eta,V_0)}}{(\hbar^2/m)(1-(m\alpha L_\perp/\hbar^2)^2)}. \tag{4.37}$$

In this case, both signs of the $\pm$ term in $k_\parallel(E_+)$ adhere to $k_\parallel \geq 0$ with an appropriate restriction on the energy range. The two solutions can be expressed as

$$\begin{aligned} k_\parallel(E_+)_+ &= \frac{mV_0\alpha L_\perp^2/\hbar^2 + \sqrt{f(E,\eta,V_0)}}{(\hbar^2/m)(1-\eta^2)}\Theta(E-E_{min}) \\ , k_\parallel(E_+)_- &= \frac{mV_0\alpha L_\perp^2/\hbar^2 - \sqrt{f(E,\eta,V_0)}}{(\hbar^2/m)(1-\eta^2)}\Theta(E-E_{min})\Theta(-mV_0^2L_\perp^2/2\hbar^2 - E). \end{aligned} \tag{4.38}$$

The bound state density of states is calculated using Eqs. (4.34,4.38) in Eq. (4.32) for three different energy ranges at the location $z = z_0$. In the energy range $E_{min} \leq E \leq -mV_0^2L_\perp^2/2\hbar^2$ both solutions $k_\parallel(E_+)_+$ and $k_\parallel(E_+)_-$ contribute to the density of states. Application of Eq. (4.32) yields

$$\begin{aligned} \varrho(E,z_0) =& \frac{1}{2\pi}k_\parallel(E_+)_+\left|\frac{\partial k_\parallel(E_+)_+}{\partial E}\right|(V_0 + \alpha k_\parallel(E_+)_+) \\ &+ \frac{1}{2\pi}k_\parallel(E_+)_-\left|\frac{\partial k_\parallel(E_+)_-}{\partial E}\right|(V_0 + \alpha k_\parallel(E_+)_-) \\ =& \frac{m^3L_\perp\alpha(V_0^2L_\perp^2 + f(E,\eta,V_0))}{\pi\hbar^6\sqrt{f(E,\eta,V_0)}(1-\eta^2)^2}. \end{aligned} \tag{4.39}$$

The bound state density of states in the energy range $-mV_0^2L_\perp^2/2\hbar^2 \leq E \leq \hbar^2V_0^2/2m\alpha^2$ is displayed in Fig.4.12 and is given by

$$\begin{aligned}
&\varrho(E,z_0) = \varrho(E_-,z_0) + \varrho(E_+,z_0) \\
=&\frac{1}{2\pi}k_\parallel(E_-)\left|\frac{\partial k_\parallel(E_-)}{\partial E}\right|(V_0 - \alpha k_\parallel(E_-)) + \frac{1}{2\pi}k_\parallel(E_+)_+\left|\frac{\partial k_\parallel(E_+)_+}{\partial E}\right|(V_0 + \alpha k_\parallel(E_+)_+) \\
=&\frac{mL_\perp}{2\pi\hbar^2}\left[\left(\frac{-mV_0\alpha L_\perp^2/\hbar^2 + \sqrt{f(E,\eta,V_0)}}{(\sqrt{f(E,\eta,V_0)})(\hbar^2/m)(1-(m\alpha L_\perp/\hbar^2)^2)}\right)\right. \\
&\left.\times\left(V_0 - \alpha\frac{-mV_0\alpha L_\perp^2/\hbar^2 + \sqrt{f(E,\eta,V_0)}}{(\hbar^2/m)(1-(m\alpha L_\perp/\hbar^2)^2)}\right)\right] \\
&+\frac{mL_\perp}{2\pi\hbar^2}\left[\left(\frac{mV_0\alpha L_\perp^2/\hbar^2 + \sqrt{f(E,\eta,V_0)}}{(\sqrt{f(E,\eta,V_0)})(\hbar^2/m)(1-(m\alpha L_\perp/\hbar^2)^2)}\right)\right. \\
&\left.\times\left(V_0 + \alpha\frac{mV_0\alpha L_\perp^2/\hbar^2 + \sqrt{f(E,\eta,V_0)}}{(\hbar^2/m)(1-(m\alpha L_\perp/\hbar^2)^2)}\right)\right] \\
=&\frac{m}{\pi\hbar^2L_\perp}\left[\frac{mV_0L_\perp^2}{\hbar^2(1-(m\alpha L_\perp/\hbar^2)^2)}\right] \\
=&\frac{\varrho_{d=2}(K_2)\beta}{L_\perp(1-\eta^2)^2},
\end{aligned} \tag{4.40}$$

where $\beta = mV_0L_\perp^2/\hbar^2$ and $\eta = m\alpha L_\perp/\hbar^2$ are dimensionless constants for a given $V_0$, $\alpha$ and $L_\perp$. $K_2 = E + mV_0^2L_\perp^2/2\hbar^2$ is the kinetic energy of electrons whose wavefunctions are exponentially confined perpendicular to the interface, which has an upper limit of $\hbar^2V_0^2/2m\alpha^2$. The $E_-$ contribution to the bound state density of states comes to zero at the maximum value $k_\parallel = V_0/\alpha$. In Sec. 4.2.3 this value for $k_\parallel$ corresponded to a van Hove type singularity in the free state density of states. For the energy range $E > \hbar^2V_0^2/2m\alpha^2$, the density of states is given solely by the contribution from the $E_+$ branch, i.e. $\varrho(E,z_0) = \varrho(E_+,z_0)$.

### 4.3.3 Analysis of bound state density of states at $z = z_0$

Equation (4.39) shows that the density of states for $E_{min} \leq E \leq -mV_0^2L_\perp^2/2\hbar^2$ contains a van Hove singularity at $E = E_{min}$. This singularity occurs at the bottom of the $E_+$ energy branch, which is consistent with the van Hove singularity which occurs in the pure two-dimensional model discussed in Ref. [25] at $E = -m_*\alpha^2/2\hbar^2$. The inclusion of the attractive potential also changes the type of divergence in the density of states for $\eta^2 = 1$. In the pure

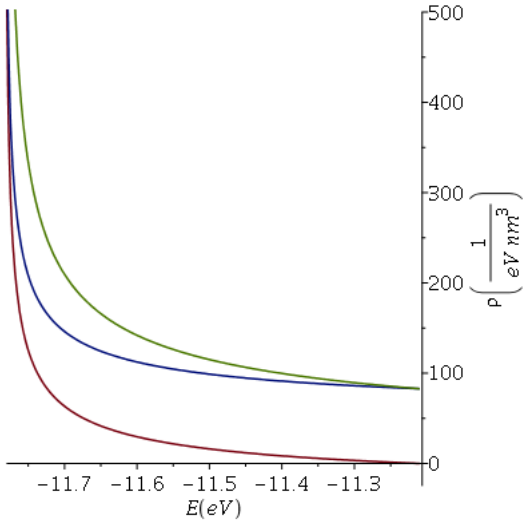


**Figure 4.11:** The spin-split and total bound state density of states at $z = z_0$ for $\alpha = 0.056$ eV nm, $V_0 = 4.36$ eV, $L_\perp = 0.3$ nm and $E_{min} \leq E \leq -mV_0^2L_\perp^2/2\hbar^2$. The green curve represents the total bound state density of states, while the blue(red) curve corresponds to the $k_\parallel(E_+)_+(k_\parallel(E_+)_-)$ contributions in Eq. (4.39).

RSOC model, $\eta^2 = 1$ corresponded to a van Hove singularity. In the current model $\eta^2 = 1$ still induces a divergence, but does not have a van Hove singularity origin. Figure 4.11 shows the density of states in the energy range $E_{min} \leq E \leq -mV_0^2L_\perp^2/2\hbar^2$. The spin-split energy branches have opposite behaviour in this region with the sum maintaining a constant value proportional to the free two-dimensional density of states properly scaled by the interface thickness $L_\perp$ reflecting that the system is three-dimensional. The density of states in this region is proportional to $V_0$ and inversely $1-\eta^2$, which implies that the divergence for $\eta^2 = 1$ transitions between energy ranges. Figure 4.12 also displays the total density of states for the energy range $E > \hbar^2V_0^2/2m\alpha^2$, where the contribution from $\varrho(E_-, z_0)$ equals zero as this corresponds to a $k_\parallel(E_-)$ value that does not preserve $\kappa_- > 0$. We expect that this value of $k_\parallel$ will result in a van Hove type singularity in the free state density of states. $\varrho(E_+, z_0)$ also diverges for $\eta^2 = 1$ and increases continuously for increasing energy. The divergence at $\eta^2 = 1$ can be attributed to the maximum value of $\eta^2$ which preserves the existence of a ground state energy. In all expressions for the density of states, the limit $L_\perp \to 0$ reduces to the free three-dimensional density of states as expected. The bound state density of states in all energy ranges has been calculated using $\alpha = 0.056$ eV nm, $L_\perp = 0.3$ nm and $V_0 = 4.36$ eV which is equal to the work function for Bismuth.

### 4.3.4 Calculation of bound state particle density at the location $z = z_0$

The results for the density of states at the location of the interface are given by

$$\varrho(E, z_0) = \begin{cases} \frac{m^3 L_\perp \alpha (V_0^2 L_\perp^2 + f(E,\eta,V_0))}{\pi\hbar^6 \sqrt{f(E,\eta,V_0)}(1-\eta^2)^2} & E_{min} \leq E \leq -mV_0^2 L_\perp^2/2\hbar^2 \\ \frac{\varrho_{d=2}(K_2)\beta}{L_\perp(1-\eta^2)^2} & -mV_0^2 L_\perp^2/2\hbar^2 \leq E \leq \hbar^2 V_0^2/2m\alpha^2 \\ \frac{mL_\perp g(E,\eta,V_0)}{2\pi\hbar^2\sqrt{f(E,\eta,V_0)}}\left(V_0 + \alpha g(E,\eta,V_0)\right) & E > \hbar^2 V_0^2/2m\alpha^2 \end{cases} \tag{4.41}$$

where

$$g(E,\eta,V_0) = \frac{mV_0\alpha L_\perp^2/\hbar^2 + \sqrt{f(E,\eta,V_0)}}{(\hbar^2/m)(1-\eta^2)}. \tag{4.42}$$

The bound state particle density at the location of the interface is calculated by integrating the density of states up to the Fermi energy $E_F$,

$$n(z_0) = \int_{E_{min}}^{E_F} dE\varrho(E, z_0), \tag{4.43}$$

with the understanding that depending on the location of the Fermi energy, we must sum the corresponding contributions to $n(z_0)$ from Eq. (4.41). For the energy range $E_{min} \leq E_F \leq -mV_0^2 L_\perp^2/2\hbar^2$,

$$\begin{aligned} n(z_0) &= \int_{E_{min}}^{E_F} dE\varrho(E, z_0) \\ &= \frac{\eta\sqrt{\frac{2mE_F L_\perp^2}{\hbar^2}(1-\eta^2) + \beta^2}}{3\pi L_\perp^3 (1-\eta^2)^2}\left(4\beta^2 + \frac{2mE_F L_\perp^2}{\hbar^2}(1-\eta^2)\right), \end{aligned} \tag{4.44}$$

which is displayed in Fig. 4.13. For the energy range $-mV_0^2 L_\perp^2/2\hbar^2 \leq E_F \leq \hbar^2 V_0^2/2m\alpha^2$

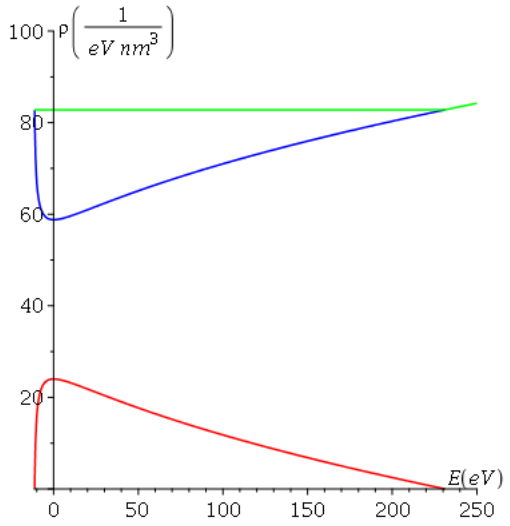


**Figure 4.12:** The spin-split and total bound state density of states at $z = z_0$ for $\alpha = 0.056$ eV nm, $V_0 = 4.36$ eV, $L_\perp = 0.3$ nm and $-mV_0^2L_\perp^2/2\hbar^2 \leq E \leq \hbar^2V_0^2/2m\alpha^2$. The green curve represents the total bound state density of states, while the blue(red) curve corresponds to $\varrho(E_+, z_0)(\varrho(E_-, z_0))$ in Eq. (4.40).

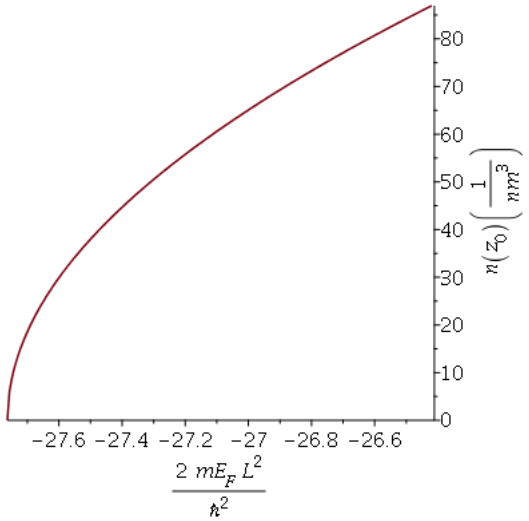


**Figure 4.13:** The total bound state particle density at $z = z_0$ for $\alpha = 0.056$ eV nm, $V_0 = 4.36$ eV, $L_\perp = 0.3$ nm and $E_{min} \leq E_F \leq -mV_0^2L_\perp^2/2\hbar^2$.

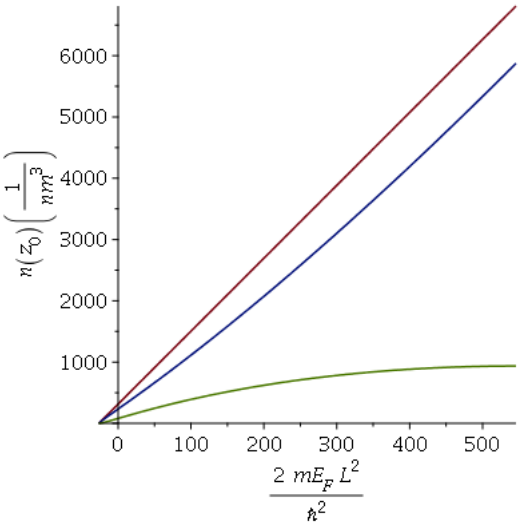


**Figure 4.14:** The spin-split and total bound state particle density at $z = z_0$ for $\alpha = 0.056$ eV nm, $V_0 = 4.36$ eV, $L_\perp = 0.3$ nm and $-mV_0^2L_\perp^2/2\hbar^2 \leq E \leq \hbar^2V_0^2/2m\alpha^2$. The red curve represents the total bound state density of states, while the blue(green) curve corresponds to $n_+(z_0)(n_-(z_0))$ in Eq. (4.45,4.46).

we can calculate the spin-split contributions to $n_\pm(z_0)$ from $\varrho(E_\pm, z_0)$ in Eq. (4.40),

$$\begin{aligned} n_+(z_0) &= \int_{-mV_0^2L_\perp^2/2\hbar^2}^{E_F} dE\varrho(E_+, z_0) \\ &= \frac{1}{12\pi L_\perp^3(\eta^6 - 3\eta^4 + 3\eta^2 - 1)}\left[\eta^4\beta\left(5\beta^2 + 3\left(\frac{2mE_FL_\perp^2}{\hbar^2}\right)\right) + 3\beta^3(2\eta^2 - 1)\right. \\ &\left. - 2\eta\sqrt{\frac{2mE_FL_\perp^2}{\hbar^2}(1-\eta^2) + \beta^2}\left(\frac{2mE_FL_\perp^2}{\hbar^2}(1-\eta^2) + \beta^2 + 3\beta^2\right) - 3\beta\left(\frac{2mE_FL_\perp^2}{\hbar^2}\right)\right], \end{aligned} \tag{4.45}$$

$$\begin{aligned} n_-(z_0) &= \int_{-mV_0^2L_\perp^2/2\hbar^2}^{E_F} dE\varrho(E_-, z_0) \\ &= \frac{1}{12\pi L_\perp^3(\eta^6 - 3\eta^4 + 3\eta^2 - 1)}\left[\eta^4\beta\left(\beta^2 + 3\left(\frac{2mE_FL_\perp^2}{\hbar^2}\right)\right) - 3\beta^3(2\eta^2 + 1)\right. \\ &\left. + 2\eta\sqrt{\frac{2mE_FL_\perp^2}{\hbar^2}(1-\eta^2) + \beta^2}\left(\frac{2mE_FL_\perp^2}{\hbar^2}(1-\eta^2) + \beta^2 + 3\beta^2\right) - 3\beta\left(\frac{2mE_FL_\perp^2}{\hbar^2}\right)\right], \end{aligned} \tag{4.46}$$

which are displayed along with the total particle density in Fig. 4.14. For the energy

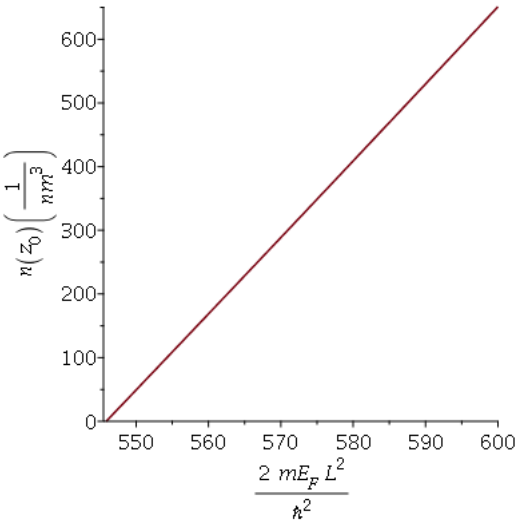


**Figure 4.15:** The total bound state particle density at $z = z_0$ for $\alpha = 0.056$ eV nm, $V_0 = 4.36$ eV, $L_\perp = 0.3$ nm and $E \geq \hbar^2 V_0^2/2m\alpha^2$ corresponding to Eq: (4.47).

range $E_F > \hbar^2 V_0^2/2m\alpha^2$,

$$\begin{aligned} n(z_0) &= \int_{\hbar^2 V_0^2/2m\alpha^2}^{E_F} dE\varrho(E, z_0) \\ &= \frac{1}{12\pi L_\perp^3 \eta^2(\eta^6 - 3\eta^4 + 3\eta^2 - 1)}\left[3\left(\frac{2mE_F L_\perp^2}{\hbar^2}\right)\eta^2\beta(\eta^4 - 1) + \beta^3(-3\eta^4 + 6\eta^2 + 5)\right. \\ &\left. - 2\eta^3\sqrt{\frac{2mE_F L_\perp^2}{\hbar^2}(1-\eta^2) + \beta^2}\left(\frac{2mE_F L_\perp^2}{\hbar^2}(1-\eta^2) + \beta^2 + 3\beta^2\right)\right], \end{aligned} \tag{4.47}$$

which is displayed in Fig. 4.15.

### 4.3.5 Analysis of bound state particle density at the location $z = z_0$

The bound state particle density in the energy range $E_{min} \leq E_F \leq -mV_0^2 L_\perp^2/2\hbar^2$ is plotted in Fig. 4.13. The behaviour in this region is similar to that of the two-dimensional model with RSOC in the region where only one of the energy branches contributes. Figure 4.14 displays the spin-split contributions and total particle density in the energy range $-mV_0^2 L_\perp^2/2\hbar^2 \leq E_F \leq \hbar^2 V_0^2/2m\alpha^2$. In this region the total density of states shows linear behaviour with respect to $E_F$ which suggests behaviour analogous to the free two-dimensional particle density. Figure 4.15 displays the particle density for $E_F \geq \hbar^2 V_0^2/2m\alpha^2$. The behaviour of the particle density is also linear in $E_F$ and therefore we conclude that the particle

density behaves according to the free two-dimensional particle density. In all energy ranges the constraint $\eta^2 \leq 1$ manisfests itself in devergent values for the particle density when $\eta^2 = 1$. The bound state particle density in all energy ranges has been calculated using $\alpha = 0.056$ eV nm, $L_\perp = 0.3$ nm and $V_0 = 4.36$ eV which is equal to the work function for Bismuth.

### 4.3.6 Calculation of free state density of states at the location $z = z_0$

The free state density of states can be calculated using

$$\varrho(E, \boldsymbol{x}) = \int d^2\boldsymbol{k}_\parallel \Theta(E - (\hbar^2 \boldsymbol{k}_\parallel^2/2m)) \frac{\partial k_\perp(E, \boldsymbol{k}_\parallel)}{\partial E} \sum_{\pm} |\langle \boldsymbol{x}|\boldsymbol{k}_\parallel, k_\perp, +\rangle_\pm|^2 \Big|_{k_\perp = k_\perp(E, \boldsymbol{k}_\parallel)}, \quad (4.48)$$

for the density of states at the location of the interface at $z = z_0$. At $z = z_0$ the odd-parity solutions do not contribute to the density of states, and have been neglected from Eq. (4.48). Inserting Eq. (3.26) into Eq. (4.48) yields with $x = k_\parallel L_\perp$

$$\begin{aligned}\varrho(E, z_0) = \frac{m\Theta(E)}{2\pi^2\hbar^2 L_\perp} \int_0^{\sqrt{2mEL_\perp^2}/\hbar} dx \Bigg( & \frac{x\sqrt{2mEL_\perp^2/\hbar^2 - x^2}}{2mEL_\perp^2/\hbar^2 - x^2 + (m/\hbar^2)^2(-V_0 L_\perp + \alpha x)^2} \\ & + \frac{x\sqrt{2mEL_\perp^2/\hbar^2 - x^2}}{2mEL_\perp^2/\hbar^2 - x^2 + (m/\hbar^2)^2(-V_0 L_\perp - \alpha x)^2} \Bigg). \end{aligned} \quad (4.49)$$

Rearranging the integrands using partial fraction decomposition and using $y = x^2$ yields

$$\begin{aligned}\varrho(E, z_0) = & \frac{m\Theta(E)}{4\pi^2\hbar^2 L_\perp(\eta^2 - 1)\sqrt{\beta^2 + (2mEL_\perp^2/\hbar^2)(1 - \eta^2)}} \int_0^{2mEL_\perp^2/\hbar^2} dy \sqrt{2mEL_\perp^2/\hbar^2 - y} \\ & \left[ \frac{\eta\beta + \sqrt{\beta^2 + (2mEL_\perp^2/\hbar^2)(1 - \eta^2)}}{y - \left( \frac{\eta\beta + \sqrt{\beta^2 + (2mEL_\perp^2/\hbar^2)(1-\eta^2)}}{1-\eta^2} \right)^2} + \frac{-\eta\beta + \sqrt{\beta^2 + (2mEL_\perp^2/\hbar^2)(1 - \eta^2)}}{y - \left( \frac{-\eta\beta + \sqrt{\beta^2 + (2mEL_\perp^2/\hbar^2)(1-\eta^2)}}{1-\eta^2} \right)^2} \right], \end{aligned} \quad (4.50)$$

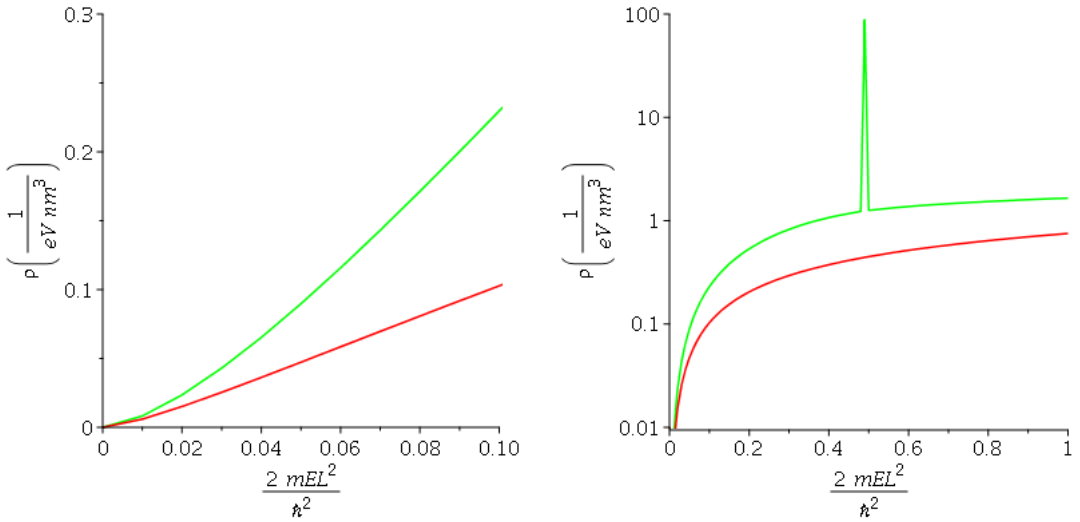


**Figure 4.16:** Free state density of states calculated using $V_0 = 0.3$ eV, $\alpha = 0.4$ eV nm and $L_\perp = 0.3$ nm. (Left) Free state density of states for low-energies. (Right) Free state density of states for high-energies in a logarithmic scale which exhibits a van Hove type singularity at $2mEL_\perp^2/\hbar^2 = \beta^2/\alpha^2$ which corresponds to $k_\parallel = V_0/\alpha$.

which yields a total density of states for energies above and below $2mEL_\perp^2/\hbar^2 = \beta^2/\eta^2$

$$\begin{aligned}\varrho(E, z_0) =& \frac{m\Theta(E)}{2\pi^2\hbar^2 L_\perp(1-\eta^2)\sqrt{d(E,\beta,\eta)}}\Bigg[(\eta\beta + \sqrt{d(E,\beta,\eta)})\Bigg(\sqrt{\frac{2mEL_\perp^2}{\hbar^2}} - \\ &\sqrt{\left(h_+(E,\beta,\eta) - 2mEL_\perp^2/\hbar^2\right.} \arctan\left(\frac{\sqrt{2mEL_\perp^2/\hbar^2}}{\sqrt{h_+(E,\beta,\eta) - 2mEL_\perp^2/\hbar^2}}\right)\Bigg) \\ &+ (-\eta\beta + \sqrt{d(E,\beta,\eta)})\Bigg(\sqrt{\frac{2mEL_\perp^2}{\hbar^2}} - \\ &\sqrt{\left(h_-(E,\beta,\eta) - 2mEL_\perp^2/\hbar^2\right.} \arctan\left(\frac{\sqrt{2mEL_\perp^2/\hbar^2}}{\sqrt{h_-(E,\beta,\eta) - 2mEL_\perp^2/\hbar^2}}\right)\Bigg)\Bigg], \quad (4.51)\end{aligned}$$

where

$$\begin{aligned} d(E,\beta,\eta) &= \beta^2 + \frac{2mEL_\perp^2}{\hbar^2}(1-\eta^2), \\ h_\pm(E,\beta,\eta) &= \left(\frac{\sqrt{d(E,\beta,\eta)} \pm \eta\beta}{1-\eta^2}\right)^2. \end{aligned} \quad (4.52)$$

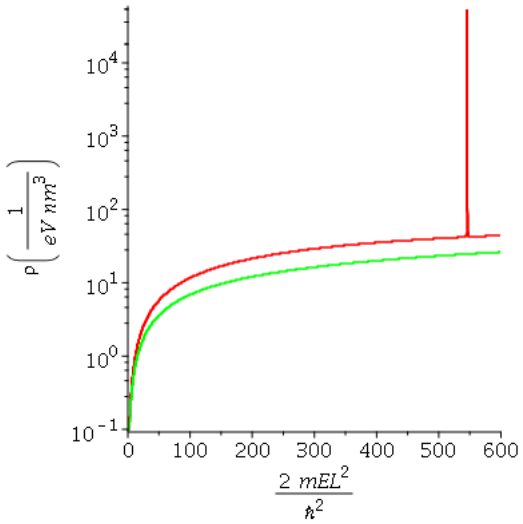


**Figure 4.17:** Free state density of states calculated using $V_0 = 4.36$ eV, $\alpha = 0.056$ eV nm and $L_\perp = 0.3$ nm. Free state density of states in a logarithmic scale which exhibits a van Hove type singularity at $2mEL_\perp^2/\hbar^2 = \beta^2/\alpha^2$ which corresponds to $k_\parallel = V_0/\alpha$.

### 4.3.7 Analysis of free state density of states at $z = z_0$

The spin-split density of states correspond to the $\pm\alpha x$ terms in Eq. (4.49), and are displayed in Fig. 4.16. The resulting spin-split contributions to the total density of states (Eq: (4.51)) contain a term proportional to the free three-dimensional density of states along with energy dependent arctan terms. For small energies the arctan terms play the dominant role as can be seen from inspecting Fig. 4.16, with three-dimensional $\sqrt{E}$ behaviour for larger energies. The $\eta^2 \leq 1$ constraint creates divergent values for the density of states when $\eta^2 = 1$. Figure 4.16 displays the free state density of states for $\alpha = 0.4$ eV nm, $V_0 = 0.3$ eV and $L_\perp = 0.3$ nm, and shows the existence of a van Hove type singularity at $2mEL_\perp^2/\hbar^2 = \beta^2/\alpha^2$ which corresponds to $k_\parallel = V_0/\alpha$, the value at which the $E_-$ contribution to the bound state density of states becomes zero. These values have been chosen for ease in viewing the behaviour of the free state density of states in an energy range which includes the van Hove singularity and three-dimensional behaviour. The origin of the singularity comes from the factor $\partial k_\perp/\partial E \sim 1/k_\perp$ in Eq. (4.48), due to the divergence at $k_\perp = 0$. This shows that the singularity has a van Hove type origin. However, the divergence does not generically generate a singularity in $\varrho(E, z_0)$ because the sum over wavefunctions squared in Eq. (4.48) vanishes sufficiently fast for $k_\perp = 0$. This is exactly the same origin as the van Hove singularity present in

Sec. 4.2.2. When $V_0 - \alpha k_\parallel = 0$ in the $|\langle \boldsymbol{x}_\parallel, z|\boldsymbol{k}_\parallel, k_\perp = 0, +\rangle_-|^2$ term in Eq. (4.48), the sum over wavefunctions squared no longer vanishes for $k_\perp = 0$, and therefore cannot compensate for the divergence from the $\partial k_\perp/\partial E$ factor. This results in a van Hove type singularity for the condition $k_\parallel^2 L_\perp^2 = 2mEL_\perp^2/\hbar^2 = \beta^2/\eta^2$. In particular the second term in Eq. (4.49) written in terms of $k_\perp$ and $k_\parallel$ is given by

$$\varrho(E, z_0)_{+\alpha k_\parallel} = \frac{\Theta(E)}{\pi^2 L_\perp} \int_0^{\sqrt{2mE}/\hbar} k_\parallel dk_\parallel \frac{(mL_\perp^2/\hbar^2 k_\perp)}{1 + (mL_\perp^2/\hbar^2 k_\perp)^2 (V_0 - \alpha k_\parallel)^2}. \tag{4.53}$$

From Ref. [26], the $\delta$-function can be represented in terms of the kernel $\gamma d(\gamma x)$ according to

$$\lim_{\gamma \to \infty} \gamma d(\gamma x) = \delta(x). \tag{4.54}$$

One particular function for $d(x)$ which adheres to Eq. (4.54) is $d(x) = 1/(\pi + \pi x^2)$ [26]. Making the substitution $\gamma = mL_\perp^2/\hbar^2 k_\perp$ and recognizing that $\gamma \to \infty$ as $k_\perp \to 0$ implies

$$\lim_{\gamma \to \infty} \int^{\sqrt{2mE}/\hbar} k_\parallel dk_\parallel \frac{\gamma}{1 + \gamma^2 (V_0 - \alpha k_\parallel)^2} \to \delta(V_0/\alpha - \sqrt{2mE}/\hbar), \tag{4.55}$$

where we have used that $k_\parallel = \sqrt{2mE}\hbar$ corresponds to $k_\perp = 0$. Clearly Eq. (4.55) is less than rigorous for an analytic description of the $\delta$ function behaviour of $\varrho(E, z_0)_{-\alpha k_\parallel}$, however it does motivate a method to calculate the size of the van Hove singularity. Integration of the density of states up to a Fermi energy which contains the singularity would allow us to calculate the effect on the particle density once the proper prefactor in Eq. (4.55) has been determined. The condition for the singularity corresponds to $k_\parallel = V_0/\alpha$ which was the corresponding value of $k_\parallel$ for which the $E_-$ contribution to the bound state density of states became zero. For completeness, Fig. 4.17 shows the van Hove singularity for $V_0 = 4.36$ eV, $\alpha = 0.056$ eV nm and $L_\perp = 0.3$ nm, i.e., the same parameter choices as in the analysis of the bound state solutions. Clearly from the analysis of this model and the model discussed in Sec. 4.2 there is a connection between the end range of values in $k_\parallel$ for bound state solutions and the existence of van Hove type singularities in the free state density of states.

## 4.4 Interdimensional system of quasirelativistic fermions with effective mass interface

### 4.4.1 Results for interdimensional system of quasirelativistic fermions with effective mass interface

Equations (3.35) and (3.39) can be solved analytically for $z = z_0$ and $E \geq mc^2$. The $\boldsymbol{x}$ representation of the energy-dependent fermionic Green function can be found in Appendix E in the form of a Hankel transform,

$$\langle \boldsymbol{x}|S(E)|\boldsymbol{x'}\rangle = \frac{1}{2\pi}\int dk_\parallel k_\parallel J_0(k_\parallel|\boldsymbol{x}-\boldsymbol{x'}|)\langle z|S(k^0,\boldsymbol{k}_\parallel)|z'\rangle|_{E=c\hbar k^0}. \tag{4.56}$$

The solution for $\mathrm{Tr}(\Im\langle \boldsymbol{x}|S(E)|\boldsymbol{x'}\rangle)$ found in the appendix yields the corresponding relation between the energy-dependent fermionic Green function and the interdimensional quasirelativistic density of states upon inserting $\boldsymbol{x} = \boldsymbol{x'}$ into Equation (2.17) for $z = z' = z_0$,

$$\begin{aligned}
\varrho(E,z_0) - \overline{\varrho}(\overline{E},z_0) \;=\; & \frac{\Theta[(k^0)^2-(mc/\hbar)^2]}{(k^0)^2-\boldsymbol{k}_\parallel^2-(mc/\hbar)^2+\ell^2\left(\boldsymbol{k}_\parallel^2+(mc/\hbar)(\Delta mc/\hbar)\right)^2}\Bigg[\frac{E}{\pi^2\hbar^2c^2} \\
& \times \int_0^{\sqrt{(k^0)^2-(mc/\hbar)^2}} dk_\parallel k_\parallel \sqrt{(k^0)^2-\boldsymbol{k}_\parallel^2-(mc/\hbar)^2} \\
& + \frac{E\ell^2(\Delta mc/\hbar)}{2\pi^2\hbar mc^3\sqrt{(k^0)^2-\boldsymbol{k}_\parallel^2-(mc/\hbar)^2}} \\
& \times \int_0^{\sqrt{(k^0)^2-(mc/\hbar)^2}} dk_\parallel k_\parallel \left(\boldsymbol{k}_\parallel^2+(mc/\hbar)^2\right)\left(\boldsymbol{k}_\parallel^2+\frac{(m\cdot\Delta m)c^2}{\hbar^2}\right)\Bigg].
\end{aligned}$$

Evaluation of the two integrals in Equation(4.57) yields

$$\varrho(E,z_0) - \overline{\varrho}(\overline{E},z_0) = \varrho(E,z_0) - \overline{\varrho}(\overline{E},z_0)|_1 + \varrho(E,z_0) - \overline{\varrho}(\overline{E},z_0)|_2,$$

$$\varrho(E,z_0)-\overline{\varrho}(\overline{E},z_0)|_1 = \frac{E\Theta(E^2-m^2c^4)}{2(\pi\hbar c)^2\ell} \times\left[\arctan\left(\frac{\sqrt{E^2-m^2c^4}\ell-\sqrt{g(E,\ell,m,\Delta m)}}{(\hbar c/2)}\right) +\arctan\left(\frac{\sqrt{E^2-m^2c^4}\ell+\sqrt{g(E,\ell,m,\Delta m)}}{(\hbar c/2)}\right)\right] +\frac{E\Theta(E^2-m^2c^4)}{8\ell\pi^2\hbar c\sqrt{g(E,\ell,m,\Delta m)}}\ln\left(\frac{f_-(E,\ell,m,\Delta m)}{f_+(E,\ell,m,\Delta m)}\right), \quad (4.57)$$

$$\varrho(E,z_0)-\overline{\varrho}(\overline{E},z_0)|_2 = \frac{E\ell^2(\Delta m)\Theta(E^2-m^2c^4)}{2\pi^2\hbar^2c^2m} \times\left[\frac{\sqrt{E^2-m^2c^4}}{\hbar c\ell^2} -\frac{2(mc^2)(mc^2-\Delta mc^2)\ell^2+\hbar^2c^2}{8\ell^3\hbar c\sqrt{g(E,\ell,m,\Delta m)}}\ln\left(\frac{f_-(E,\ell,m,\Delta m)}{f_+(E,\ell,m,\Delta m)}\right) -\frac{1}{2\ell^3}\left[\arctan\left(\frac{\sqrt{E^2-m^2c^4}\ell-\sqrt{g(E,\ell,m,\Delta m)}}{(\hbar c/2)}\right) +\arctan\left(\frac{\sqrt{E^2-m^2c^4}\ell+\sqrt{g(E,\ell,m,\Delta m)}}{(\hbar c/2)}\right)\right]\right], \quad (4.58)$$

where $f_\pm(E,\ell,m,\Delta m)=2(E^2-m^2c^4)\ell+(m\cdot\Delta m)c^4\ell\pm 2\sqrt{E^2-m^2c^4}\sqrt{g(E,\ell,m\Delta m)}$, and $g(E,\ell,m,\Delta m)=\ell^2(E^2-m^2c^4+(m\cdot\Delta m)c^4)-(\hbar^2c^2)/4$. Both of the two terms in the interdimensional quasirelativistic density of states remain real for $g(E,\ell,m,\Delta m)<0$. We can further simplify the two terms in the density of states so that they are expressed entirely of real functions. This is accomplished using

$$\frac{1}{i}\ln\left(\frac{x+iy}{x-iy}\right)=2\arctan\left(\frac{y}{x}\right),$$

$$\arctan(x+iy)+\arctan(x-iy)=\arctan\left(\frac{x}{1+y}\right)+\arctan\left(\frac{x}{1-y}\right),$$

and

$$\arctan(p)-\arctan(q)=\arctan\left(\frac{p-q}{1+pq}\right). \quad (4.59)$$

The two terms in the density of states given in terms of entirely real functions are

$$\begin{aligned}\varrho(E,z_0)-\overline{\varrho}(\overline{E},z_0)|_1 &= \frac{E\Theta(E^2-m^2c^4)}{2(\pi\hbar c)^2\ell}\left[\arctan\left(\frac{\ell\sqrt{E^2-m^2c^4}}{\hbar c/2+\sqrt{-g(E,\ell,m,\Delta m)}}\right)\right.\\ &\left.+\arctan\left(\frac{\ell\sqrt{E^2-m^2c^4}}{\hbar c/2-\sqrt{-g(E,\ell,m,\Delta m)}}\right)\right]\\ &+\frac{E\Theta(E^2-m^2c^4)}{4\ell\pi^2\hbar c\sqrt{-g(E,\ell,m,\Delta m)}}\\ &\times\left[\arctan\left(\frac{\ell\sqrt{E^2-m^2c^4}}{\hbar c/2+\sqrt{-g(E,\ell,m,\Delta m)}}\right)\right.\\ &\left.-\arctan\left(\frac{\ell\sqrt{E^2-m^2c^4}}{\hbar c/2-\sqrt{-g(E,\ell,m,\Delta m)}}\right)\right], \end{aligned} \tag{4.60}$$

$$\begin{aligned}\varrho(E,z_0)-\overline{\varrho}(\overline{E},z_0)|_2 &= \left(\frac{\Delta m}{m}\right)\Theta(E^2-m^2c^4)\left[\frac{E\sqrt{E^2-m^2c^4}}{2\pi^2\hbar^3c^3}\right.\\ &-\frac{E\left[2(mc^2)(mc^2-\Delta mc^2)\ell^2+\hbar^2c^2\right]}{8\pi^2\ell\hbar^3c^3\sqrt{-g(E,\ell,m,\Delta m)}}\\ &\times\left[\arctan\left(\frac{\ell\sqrt{E^2-m^2c^4}}{\hbar c/2+\sqrt{-g(E,\ell,m,\Delta m)}}\right)\right.\\ &\left.-\arctan\left(\frac{\ell\sqrt{E^2-m^2c^4}}{\hbar c/2-\sqrt{-g(E,\ell,m,\Delta m)}}\right)\right]\\ &-\left(\frac{E}{4\pi^2\hbar^2c^2\ell}\right)\left[\arctan\left(\frac{\ell\sqrt{E^2-m^2c^4}}{\hbar c/2+\sqrt{-g(E,\ell,m,\Delta m)}}\right)\right.\\ &+\left.\left.\arctan\left(\frac{\ell\sqrt{E^2-m^2c^4}}{\hbar c/2-\sqrt{-g(E,\ell,m,\Delta m)}}\right)\right]\right]. \end{aligned} \tag{4.61}$$

In the case where $\Delta m \ll m$, the term $\varrho(E,z_0)-\overline{\varrho}(\overline{E},z_0)|_2 \ll \varrho(E,z_0)-\overline{\varrho}(\overline{E},z_0)|_1$ and the interdimensional quasirelativistic density of states is given solely by the $\varrho(E,z_0)-\overline{\varrho}(\overline{E},z_0)|_1$ term.

### 4.4.2 Analysis of density of states

To begin analyzing the high-energy and low-energy cases for the interdimensional quasirelativistic density of states, we will set $\Delta mc^2 = 0$. The low-energy limit for the interdimensional quasirelativistic density of states is given by $(m\cdot\Delta m)c^4 \ll E^2-m^2c^4 \ll \hbar^2c^2/4\ell^2$. Given

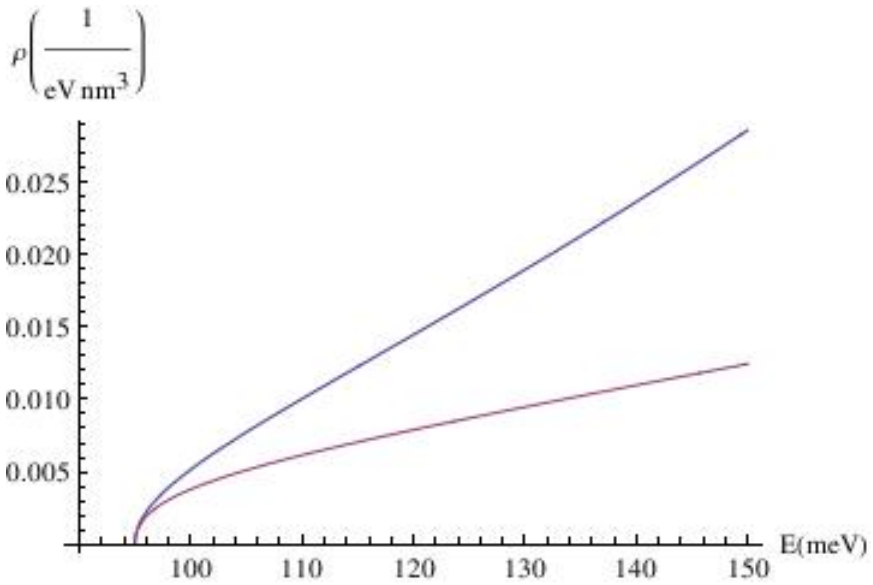


**Figure 4.18:** The upper line is the three-dimensional density of states. The lower line is the density of states in the interface for $\ell = 3$ nm, $\Delta_g = 95$ meV and $\Delta mc^2 = 0$.

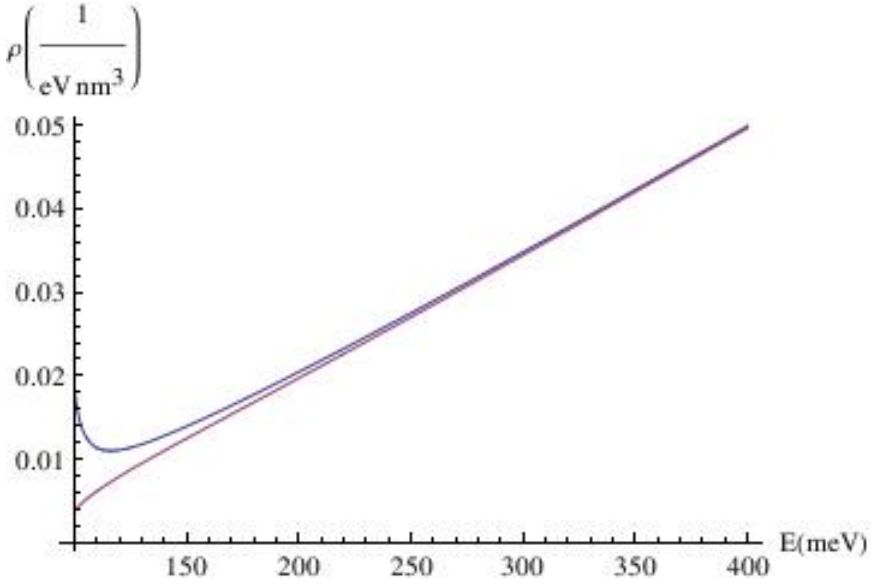


**Figure 4.19:** The upper line corresponds to the two-dimensional limit of the density of states in the interface plus the logarithmic correction. The lower curve is the density of states in the interface for $\ell = 3$ nm, $\Delta_g = 95$ meV and $\Delta mc^2 = 0$.

this inequality, $\sqrt{-g(E,\ell,m,\Delta m)} \to \sqrt{(\hbar c/2)^2} = \hbar c/2$, and the interdimensional quasirelativistic density of states reduces to

$$\begin{aligned} \varrho(E,z_0) - \overline{\varrho}(\overline{E},z_0) &= \frac{\Theta(E^2-m^2c^4)E\sqrt{E^2-m^2c^4}}{\pi^2\hbar^3c^3} \\ &= \left[\varrho(E) - \overline{\varrho}(\overline{E})\right]_{d=3}, \end{aligned} \tag{4.62}$$

where the second equality shows that in the low-energy limit, the interdimensional quasirelativistic density of states reduces to the relaivistic three-dimensional density of states. Following a similar analysis, in the limit that the interface thickness approaches zero ($\ell \to 0$), the interdimensional quasirelativistic density of states again reduces to the relativistic three-dimensional density of states,

$$\begin{aligned} \left[\varrho(E,z_0) - \overline{\varrho}(\overline{E},z_0)\right]_{\ell\to 0} &= \frac{\Theta(E^2-m^2c^4)E\sqrt{E^2-m^2c^4}}{\pi^2\hbar^3c^3} \\ &= \left[\varrho(E) - \overline{\varrho}(\overline{E})\right]_{d=3}. \end{aligned} \tag{4.63}$$

Figure 4.18 displays the free relativistic three-dimensional density of states along with the interdimensional quasirelativistic density of states inside the interface. The high-energy limit is given by $E^2 - m^2c^4 \gg \hbar^2c^2/4\ell^2 - (m\cdot\Delta m)c^4$. Given the inequality, $\sqrt{-g(E,\ell,m,\Delta m)} \to i\ell\sqrt{E^2-m^2c^4}$, this yields for the particle density of states ($E > mc^2$), which shows that in the high-energy limit, the interdimensional quasirelativistic density of states reduces to the two-dimensional relativistic fermionic density of states and a logarithmic correction term,

$$\begin{aligned} \varrho(E,z_0) &= \frac{\varrho(E)_{d=2}}{4\ell} \\ &\quad - \frac{E\Theta(E^2-m^2c^4)}{4\ell^2\pi^2\hbar c\sqrt{E^2-m^2c^4}} \ln\left(\frac{4|\ell|\sqrt{E^2-m^2c^4}}{\hbar c}\right). \end{aligned} \tag{4.64}$$

The two-dimensional density of states term is properly scaled by a factor of interface thickness which reflects the fact this is still a density of states per volume. Figure 4.19 displays the free relativistic two-dimensional density of states with the logarithmic correction term along with the interdimensional quasirelativistic density of states inside the interface. In order to analyze the interdimensional quasirelativistic density of states around the points with energy $E = \Delta_g = mc^2$ for a negative gap shift $\Delta mc^2 < 0$, we must analyze the contributions from both $[\varrho(E,z_0) - \overline{\varrho}(\overline{E},z_0)]_1$ and $[\varrho(E,z_0) - \overline{\varrho}(\overline{E},z_0)]_2$. $2\Delta_g$ represents the energy-gap between

Dirac hyperboloids. We will analyze the two terms in the inter-dimensional density of states separately and then combine our results at the end in order to see the effect on the density of states about the point $E = \Delta_g$ for a negative gap shift. Setting $E = \Delta_g$ and $\Delta mc^2 < 0$ in the first and second terms yields

$$\begin{aligned}
\varrho(\Delta_g, z_0)_1|_{\Delta m<0} &= \frac{\Delta_g \Theta(\Delta_g^2 - m^2c^4)}{2(\pi\hbar c)^2 \ell} \\
&\times \left[ \arctan\left( \frac{\ell\sqrt{\Delta_g^2 - m^2c^4}}{(\hbar c/2) + \sqrt{-g(\Delta_g, \ell, m, \Delta m)}} \right) \right. \\
&\left. + \arctan\left( \frac{\ell\sqrt{\Delta_g^2 - m^2c^4}}{(\hbar c/2) - \sqrt{-g(\Delta_g, \ell, m, \Delta m)}} \right) \right] \\
&+ \frac{\Delta_g \Theta(\Delta_g^2 - m^2c^4)}{4\ell\pi^2\hbar c\sqrt{-g(\Delta_g, \ell, m, \Delta m)}} \\
&\times \left[ \arctan\left( \frac{\ell\sqrt{\Delta_g^2 - m^2c^4}}{(\hbar c/2) + \sqrt{-g(\Delta_g, \ell, m, \Delta m)}} \right) \right. \\
&\left. - \arctan\left( \frac{\ell\sqrt{\Delta_g^2 - m^2c^4}}{(\hbar c/2) + \sqrt{-g(\Delta_g, \ell, m, \Delta m)}} \right) \right], \qquad (4.65)
\end{aligned}$$

$$\begin{aligned}
\varrho(\Delta_g, z_0)_2|_{\Delta m<0} &= \left( \frac{\Delta m}{m} \right) \Theta(\Delta_g^2 - m^2c^4) \left[ \frac{\Delta_g\sqrt{\Delta_g^2 - m^2c^4}}{2\pi^2\hbar^3c^3} \right. \\
&\left. - \frac{\Delta_g\left[2(mc^2)(mc^2 - \Delta mc^2)\ell^2 + \hbar^2c^2\right]}{8\pi^2\ell\hbar^3c^3\sqrt{-g(\Delta_g, \ell, m, \Delta m)}} \right. \\
&\times \left[ \arctan\left( \frac{\ell\sqrt{\Delta_g^2 - m^2c^4}}{\hbar c/2 + \sqrt{-g(\Delta_g, \ell, m, \Delta m)}} \right) \right. \\
&\left. - \arctan\left( \frac{\ell\sqrt{\Delta_g^2 - m^2c^4}}{\hbar c/2 - \sqrt{-g(\Delta_g, \ell, m, \Delta m)}} \right) \right] \\
&- \left( \frac{\Delta_g}{4\pi^2\hbar^2c^2\ell} \right) \left[ \arctan\left( \frac{\ell\sqrt{\Delta_g^2 - m^2c^4}}{\hbar c/2 + \sqrt{-g(\Delta_g, \ell, m, \Delta m)}} \right) \right. \\
&\left. \left. + \arctan\left( \frac{\ell\sqrt{\Delta_g^2 - m^2c^4}}{\hbar c/2 - \sqrt{-g(\Delta_g, \ell, m, \Delta m)}} \right) \right] \right], \qquad (4.66)
\end{aligned}$$

where $g(\Delta_g, \ell, m, \Delta m) = \ell^2(m \cdot \Delta m)c^4 - \hbar^2c^2/4$. The arctan functions in the density of states equation as defined within, follow the inequality $0 \leq \arctan(x) < \pi$. This means that if $x$ is negative, we must add $\pi$ to the value $\arctan(-x)$ to properly ensure the continuity and smoothness properties of the Green function matrix element that was used to derive

the density of states equation. For $E \to \Delta_g = mc^2$, the arguments of the arctan functions approaches zero. Therefore, we must analyze the two different arguments of the arctan functions to evaluate whether or not the arctan fucntion approaches 0 or $\pi$ as their argument approaches zero. For the first arctan argument we have

$$\begin{aligned}
\frac{\ell\sqrt{\Delta_g^2 - m^2c^4}}{(\hbar c/2) + \sqrt{(\hbar c/2)^2 - \ell^2(m\cdot\Delta m)c^4}} &= \sqrt{\Delta_g^2 - m^2c^4} \\
&\times \left[\frac{(\hbar c/2) - \sqrt{(\hbar c/2)^2 - \ell(m\cdot\Delta m)c^4}}{\ell^2(m\cdot\Delta m)c^4}\right] \\
&= \sqrt{\Delta_g^2 - m^2c^4} \\
&\times \left[\frac{-(\hbar c/2) + \sqrt{(\hbar c/2)^2 + \ell^2 m|\Delta m|c^4}}{\ell(m|\Delta m|)c^4}\right] \\
&= \sqrt{\Delta_g^2 - m^2c^4} \\
&\times \left[\frac{-(\hbar c/2) + (\hbar c/2)\sqrt{1 + \frac{4\ell^2 m|\Delta m|c^2}{\hbar^2}}}{\ell(m|\Delta m|)c^4}\right]. \quad (4.67)
\end{aligned}$$

Therefore since $(\ell(m\cdot|\Delta m|c^2)/\hbar^2 > 0$, the term multiplying $\sqrt{\Delta_g^2 - m^2c^4}$ is a positive finite constant. To approximate the limiting value of the arctan function as its argument approaches zero from the positive side we use only the first term from its Taylor series expansion. We have

$$\arctan(\epsilon) = \epsilon \to 0^+,$$

for $\epsilon > 0$. We therefore have determined that this argument in the arctan function adheres to the equation,

$$\lim_{E^2\to\Delta_g^2} \arctan\left(\frac{\ell\sqrt{\Delta_g^2 - m^2c^4}}{(\hbar c/2) + \sqrt{(\hbar c/2)^2 - \ell^2(m\cdot\Delta m)c^4}}\right) \to 0. \quad (4.68)$$

For the second arctan argument we have,

$$\begin{aligned}\frac{\ell\sqrt{\Delta_g^2 - m^2c^4}}{(\hbar c/2) - \sqrt{(\hbar c/2)^2 - \ell^2(m\cdot\Delta m)c^4}} &= \sqrt{\Delta_g^2 - m^2c^4} \\ &\times\left[\frac{(\hbar c/2) + \sqrt{(\hbar c/2)^2 - \ell(m\cdot\Delta m)c^4}}{-\ell^2(m\cdot\Delta m)c^4}\right] \\ &= \sqrt{\Delta_g^2 - m^2c^4} \\ &\times\left[\frac{(\hbar c/2) + \sqrt{(\hbar c/2)^2 + \ell^2 m|\Delta m|c^4}}{-\ell(m|\Delta m|)c^4}\right] \\ &= \sqrt{\Delta_g^2 - m^2c^4} \\ &\times\left[\frac{(\hbar c/2) + (\hbar c/2)\sqrt{1 + \frac{4\ell^2 m|\Delta m|c^2}{\hbar^2}}}{-\ell(m|\Delta m|)c^4}\right]. \quad (4.69)\end{aligned}$$

Therefore since $(-\ell(m\cdot|\Delta m|c^2)/\hbar^2 < 0$, the term multiplying $\sqrt{\Delta_g^2 - m^2c^4}$ is a negative finite constant. Therefore we must add $\pi$ to the value of the arctan function since it has a negative argument. Using the first term in the Taylor series to approximate the arctan function yields

$$\arctan(-\epsilon) = \pi - \epsilon \to \pi, \quad (4.70)$$

for $\epsilon > 0$. We have thus determined that this argument in the arctan function adheres to the equation

$$\lim_{E^2\to\Delta_g^2} \arctan\left(\frac{\ell\sqrt{\Delta_g^2 - m^2c^4}}{(\hbar c/2) - \sqrt{(\hbar c/2)^2 - \ell^2(m\cdot\Delta m)c^4}}\right) \to \pi. \quad (4.71)$$

Applying these results to the density of states equation about the point $E \to \Delta_g = mc^2$ yields

$$\varrho(\Delta_g, z_0)_1|_{\Delta m<0} = \frac{\Delta_g}{2\pi\hbar^2c^2\ell}\left(1 - \frac{\hbar c}{\sqrt{\hbar^2c^2 + 4\ell^2(m|\Delta m|)c^4}}\right), \quad (4.72)$$

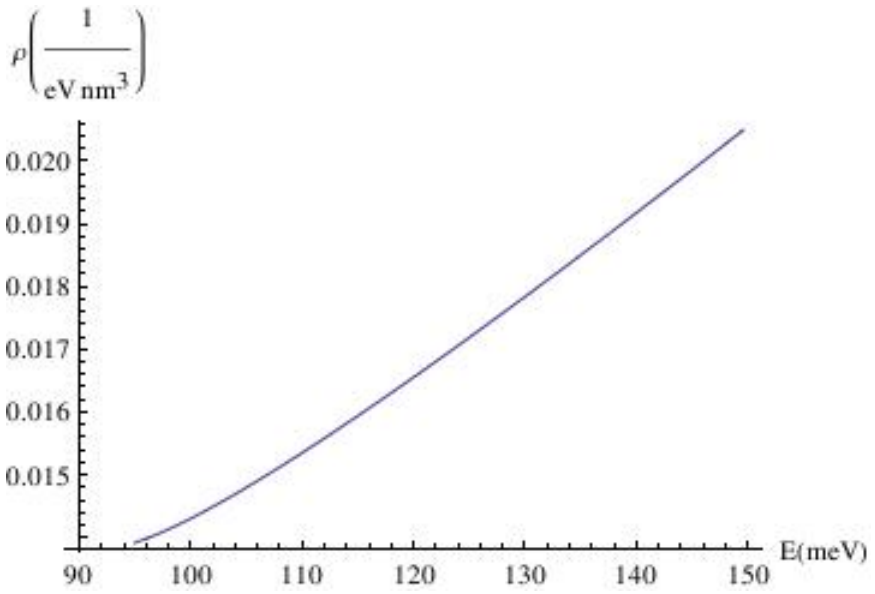


**Figure 4.20:** The density of states in the interface for $\ell = 3$ nm, $E > \Delta_g = 95$ meV, and a bulk gap shift parameter of $\Delta mc^2 = -\Delta_g$.

$$\begin{aligned}\varrho(\Delta_g, z_0)_2|_{\Delta m<0} &= \left(\frac{-|\Delta m|}{m}\right)\left[0 - \frac{\Delta_g[2mc^2(mc^2+|\Delta m|c^2)\ell^2+\hbar^2c^2]}{8\pi^2\ell\hbar^3c^3\sqrt{\hbar^2c^2+4\ell^2(m|\Delta m|)c^4}}(0-\pi)\right. \\ &\quad \left. -\frac{\Delta_g}{4\pi^2\hbar^2c^2\ell}(0+\pi)\right] \\ &= \left(\frac{|\Delta m|}{m}\right)\frac{\Delta_g}{4\pi\ell\hbar^2c^2}\left(1-\frac{\hbar c}{\sqrt{\hbar^2c^2+4\ell^2m|\Delta m|c^4}}\right) \\ &\quad -\left(\frac{|\Delta m|}{m}\right)\frac{\Delta_g mc^2(mc^2+|\Delta m|c^2)\ell\hbar c}{2\pi\hbar^4c^4\sqrt{\hbar^2c^2+4\ell^2m|\Delta m|c^4}}. \end{aligned} \tag{4.73}$$

Combining the above results yields the finite offset in the density of states inside the interface for a negative gap shift $\Delta mc^2$

$$\begin{aligned}\varrho(\Delta_g, z_0)_{1+2}|_{\Delta m<0} &= \frac{\Delta_g}{2\pi\ell\hbar^2c^2}\left(1-\frac{\hbar c}{\sqrt{\hbar^2c^2+4\ell^2m|\Delta m|c^4}}\right) \\ &\quad +\left(\frac{|\Delta m|}{m}\right)\frac{\Delta_g}{4\pi\ell\hbar^2c^2}\left(1-\frac{\hbar^2c^2+2mc^2(mc^2+|\Delta m|c^2)\ell^2}{\hbar c\sqrt{\hbar^2c^2+4\ell^2m|\Delta m|c^4}}\right). \end{aligned} \tag{4.74}$$

Figure 4.20 displays the increase in the interdimensional quasirelativistic density of states inside the interface for a negative gap shift parameter that closes the band gap. The quasirelativistic density of states inside the interface at $z = z_0$ approaches the free three-dimensional

relativistic density of states in the limit that the interface thickness $\ell$ approaches zero. This result is obviously expected as this limit is effectively removing the interface term from the quasirelativistic interdimensional Hamiltonian from which we started our calculation of the density of states. The free three-dimensional relativistic density of states is also found from the limit $|\Delta m|mc^4 \ll E^2 - m^2c^4 \ll \hbar^2c^2/4\ell^2$ of the quasirelativistic density of states. This inequality tells us that for small energies given by $\sqrt{E^2 - m^2c^4}$, the quasirelativistic density of states approaches the three-dimensional limit provided that the change in the bulk gap parameter $|\Delta m|$ is small compared to the particle's energy. This low-energy limit is analogous to the limit $8mE\ell^2 \ll \hbar^2$ used in Ref. [58]. The small-energy limit coincides with states that probed length scales that are larger than the parameter $\ell = Lm/2m_*$ where $L$ is the interface thickness. This can be written in terms of the de Broglie wavelength in the direction perpendicular to the interface. In the non-relativistic case, we can substitute the de Broglie wavelength $\lambda = 2\pi\hbar/p$ into the inequality for three-dimensional behaviour, $8mE\ell^2 \ll \hbar^2$ [58]. Here $E$ is the particle's kinetic energy and is given by $E = \hbar^2\boldsymbol{k}^2/2m = \boldsymbol{p}^2/2m$. Therefore the de Broglie wavelength in terms of the kinetic energy is

$$\begin{aligned} \lambda = \frac{2\pi\hbar}{|\boldsymbol{p}|} &= \frac{2\pi\hbar}{\sqrt{2mE}} \\ &= \frac{\sqrt{2}\pi\hbar}{\sqrt{mE}}. \end{aligned} \tag{4.75}$$

The inequality $8mE\ell^2 \ll \hbar^2$ can be written as

$$\begin{aligned} \sqrt{\ell^2} = \ell &\ll \sqrt{\frac{\hbar^2}{8mE}} \\ &= \frac{\hbar}{2\sqrt{2mE}} \\ &= \frac{\lambda}{4\pi} \end{aligned} \tag{4.76}$$

Thus for low energies that adhere to the inequality $8mE\ell^2 \ll \hbar^2$, the particle's de Broglie wavelength in the direction perpendicular to the interface is much larger compared to the interface thickness, $\ell \ll \lambda/4\pi$. Intuitively this suggests that the particle would see the bulk even though it is located in the interface, and in kind, have a free three-dimensional density of states. We can apply the same kind of analysis to the large-energy inequality, $8mE\ell^2 \gg \hbar^2$. This shows that for high energy, $\ell \gg \lambda/4\pi$. In this limit, the de Broglie wavelength in the

direction perpendicular to the interface is much smaller than the thickness of the interface. It is thus expected that the density of states in the high-energy limit inside the interface resembles the two-dimensional density of states for a free particle.

We can use this argument in the quasirelativistic interdimensional system as well. The de Broglie wavelength equation holds in the relativistic case as long as we use the appropriate expression for momentum $p$. We know that relativistic particles follow the relativistic dispersion relation,

$$E^2 = p^2c^2 + m^2c^4.$$

Solving the equation for $pc$ and inserting that into the definition of the de Broglie wavelength,

$$\lambda = \frac{hc}{pc},$$

results in

$$\lambda = \frac{2\pi\hbar c}{\sqrt{E^2 - m^2c^4}}. \tag{4.77}$$

Setting $|\Delta m| = 0$ in the low energy inequality $|\Delta m|mc^4 \ll E^2 - m^2c^4 \ll \hbar^2c^2/4\ell^2$ allows us to rearrange it in terms of the interface length parameter $\ell$ and the de Broglie wavelength. Isolating for $\ell$ and substituting our expression in the de Broglie wavelength yield

$$\begin{aligned} \ell = \sqrt{\ell^2} &\ll \sqrt{\frac{\hbar^2c^2}{E^2 - m^2c^4}} \\ &= \frac{\hbar c}{\sqrt{E^2 - m^2c^4}} \\ &= \frac{\lambda}{4\pi}. \end{aligned} \tag{4.78}$$

Thus in the low-energy limit, the de Broglie wavelength is much larger than the interface length parameter. In terms of the de Broglie wavelength in the direction perpendicular to the interface, this tells us that the wavelength extends past the edges of the interface into the three-dimensional bulk. It then makes intuitive sense that as the de Broglie wavelength extends into the bulk, the particle effectively sees more bulk than interface, and its density of states in the interface approaches the three-dimensional density of states.

We can apply this reasoning to the high-energy case as well. Once again we will use $|\Delta m| = 0$. The high-energy inequality is given by $E^2 - m^2c^4 \gg \hbar^2c^2/4\ell^2$. Isolating for $\ell$ and

inserting our expression for the de Broglie wavelength yield

$$\begin{aligned} \ell = \sqrt{\ell^2} \quad &>> \quad \sqrt{\frac{\hbar^2 c^2}{E^2 - m^2 c^4}} \\ &= \quad \frac{\hbar c}{\sqrt{E^2 - m^2 c^4}} \\ &= \quad \frac{\lambda}{4\pi}. \end{aligned} \tag{4.79}$$

Therefore in the high-energy limit, the de Broglie wavelength is much smaller than the interface length parameter. Considering the de Broglie wavelength in the direction of the interface thickness, this tells us that the entire de Broglie wavelength of the particle resides inside the interface. It therefore makes intuitive sense that because the de Broglie wavelength is located entirely inside the interface, the density of states of the particle inside the interface would approach the two-dimensional density of states. Our results as presented are in complete agreement with the results found in [61] for interdimensional systems of quasirelativistic bosons, and [58] for interdimensional systems of nonrelativistic electrons. In particular, the nonrelativistic limit of the interdimensional quasirelativistic Dirac Hamiltonian (3.33) is given by

$$\begin{aligned} H = &\int d^3\boldsymbol{x} \left( \frac{\hbar^2}{2m} \boldsymbol{\nabla}\psi^\dagger \cdot \boldsymbol{\nabla}\psi + mc^2 \psi^\dagger \psi \right) \\ &+ \ell \int d^2\boldsymbol{x}_\parallel \left( \frac{\hbar^2}{2m} \boldsymbol{\nabla}_\parallel \psi^\dagger \cdot \boldsymbol{\nabla}_\parallel \psi + (\Delta m) c^2 \psi^\dagger \psi \right), \end{aligned} \tag{4.80}$$

where the mass term ($mc^2$) and mass gap shift term ($\Delta mc^2$) are present because we began with a relativistic Hamiltonian. The nonrelativistic limit of the Dirac field $\Psi$ can be found, for example, in Reference [26]. As well, the nonrelativistic limit of (4.61) yields the correct expression for the free nonrelativistic density of states in the low and high-energy limits respectively.

# 5 Conclusion and Outlook

## 5.1 Conclusion

We have calculated and analyzed interdimensional models in which electron motion is affected due to the presence of a two-dimensional interface or surface. In order to model various materials and heterostructures which are favorable to the field of spintronics, we have included changes in effective mass and RSOC as the mechanisms responsible for the affected electron motion. We have calculated analytic expressions for the density of states and in some cases particle density at the location of the interface. We have analyzed three interdimensional systems which include RSOC along an interface in order to model materials where RSOC effects exist only along an interface.

We have employed the use of interdimensional models to analyze systems of fermions which have novel physical properties along a surface or interface. A preliminary investigation into the effects of RSOC along an interface is conducted using our pure RSOC model. We have derived analytic expressions for the density of states and particle density at the location of the interface. Our results for the density of states and particle density are a superposition of two-dimensional and three-dimensional behaviour. Three-dimensional behaviour originates from free states, while two-dimensional behaviour comes from bound states whose wavefunction is exponentially suppressed perpendicular to the interface. The pure RSOC model presents an example system where the bound state wavenumber depends explicitly on the wavenumber for motion parallel to the interface, i.e., $\kappa = \kappa(k_\parallel)$. Therefore, bound state solutions exist for states whose motion is focused along the interface, as there is no potential for confinement. The bound state dispersion relation requires that $m\alpha L_\perp/\hbar^2 \leq 1$ in order for a ground state energy to exist. At the upper limit of this inequality, $m\alpha L_\perp/\hbar^2 = 1$, the bound state contribution to the density of states has a van Hove singularity. The van Hove singularity

occurs at the minimum energy in the bound state dispersion relation which is analogous to the van Hove singularity present in the original two-dimensional model with RSOC. The van Hove singularity in our interdimensional model does not depend on a particular $k_{\|}$ but rather values of $\alpha$ and $L_{\perp}$. The requirement of a ground state energy limits the RSOC strength for a given interface thickness. Using $L_{\perp} = 0.3$ nm implies that $\alpha \leq 2.54 \times 10^{-10}$ eV m. In the limit of vanishing interface thickness $L_{\perp} \to 0$ or vanishing RSOC strength $\alpha \to 0$, both the density of states and particle density at the location of the interface reduce to the free three-dimensional values respectively.

To study heterostructure systems in which electrons move with a different effective mass in an interface which also has RSOC (Cu/Bi and Ag/Bi bilayer systems), we have studied an interdimensional model with a RSOC and effective mass interface. We have numerically calculated the free state contribution to the density of states at the location of the interface. Comparing the density of states in this model with the density of states for a change in effective mass but no RSOC shows that the density of states exhibits three-dimensional behaviour for low-energies, transitioning to two-dimensional behaviour for high-energies. The system with RSOC plus effective mass interface contains the occurence of a van Hove singularity for the condition $k_{\|}^2\ell^2 = 2mE\ell^2/\hbar^2 = \eta^2$, $k_{\perp} = 0$. Analyzing the calculaltion of the free state density of states shows that the van Hove singularity originates from a term containing the lower energy branch in the two-dimensional model with RSOC. In the two-dimensional model this lower energy branch also contains a van Hove singularity and thus appears to be transferring this property to the free state density of states. The van Hove singularity also occurs at the maximum value of $k_{\|}$ for which bound state solutions exist. The bound state contribution to the density of states is calculated by constructing approximate analytic solutions for $k_{\|}$ that preserve $\kappa > 0$. The bound state contribution to the density of states is proportional to the free two-dimensional density of states. The bound state wavenumber, similar to the the pure RSOC model, is a function of $k_{\|}$ explicitly. The bound states density of states increases with increasing RSOC strength and has the minimum value of 0 at $k_{\|} = 0$ and $k_{\|} = \eta/\ell$. A peak value for the bound state density of states occurs at $E = \eta^2/4$.

To study the Edelstein and inverse Edelstein effect in heterostructures with RSOC along an interface, we have constructed an interdimensional model with an interface term that

contains RSOC and an attractive potential. The inclusion of the attractive potential is the first occurence in our interdimensional models with RSOC where there are two possible values for bound state wavenumbers, and hence we see a spin splitting in the dispersion relation and density of states. This spin-splitting allows for the comparison of our interdimensional results for the Edelstein (and inverse Edelstein) effect with two-dimensional models. An analysis of the dispersion relation for bound states in the interdimensional model shows that the energy branch $E_-$ is constrained to a maximum value of $\hbar^2 V_0^2/2m\alpha^2$. This constraint acts to enhance the Edelstein (and inverse Edelstein) effect because there is no similar constraint on the $E_+$ branch. The bound state contribution to the density of states contains a van Hove singularity at $E_{min} = -mV_0^2 L_\perp^2/2\hbar^2(1-\eta^2)$ similar to the van Hove singularity which occurs at the minimum energy in the two-dimensional RSOC model. In the energy range $-mV_0^2 L_\perp^2/2\hbar^2 \leq E \leq \hbar^2 V_0^2/2m\alpha^2$ the bound state density of states is proportional to the free two-dimensional density of states scaled by the interface thickness $L_\perp$. In this energy range, the $E_-$ contribution to the bound state equals zero at $k_\parallel = V_0/\alpha$. The free state contribution to the density of states contains a term proportional to the free three-dimensional density of states along with energy-dependent arctan terms. The density of states exhibits three-dimensional behaviour for high energies, and a van Hove type singularity with exactly the same type of origin as in the RSOC plus effective mass interface model, but with the condition $k_\parallel^2 L_\perp^2 = 2mEL_\perp^2/\hbar^2 = \beta^2/\eta^2$.

We have constructed a quasirelativistic interdimensional Hamiltonian for fermions which experience different propagation properties and a change in the bulk gap parameter for motion inside an interface. We have calculated the corresponding Green function and density of states for this system, and report that the density of states inside the interface exhibits three-dimensional behaviour for low energies, and two-dimensional behaviour up to a logarithmic correction term for high energies. Our results for the density of states are consistent with the results derived in Ref. [61] for quasirelativistic bosons, and Ref. [58] for nonrelativistic electrons subject to a parabolic band approximation. The interdimensional Hamiltonian agrees with the results derived in Ref. [58] provided that the quasirelativistic low-dimensional $\Delta m$ term is small compared to the kinetic terms for motion in the interface. Our results for the density of states in the interface are analytical, and demonstrate that the presence of

an interface term which does not exert any attractive potential still induces two-dimensional behaviour at high energies. The results also directly translate into corresponding optical properties of Dirac materials through the joint density of states for direct transitions near Dirac points or Dirac hyperboloids in momentum space.

From our analysis of the interdimensional models discussed in this thesis we conclude the following behaviour. Interdimensional systems which model materials with a different effective mass (or gap parameter in the quasirelativistic fermion model) for motion along an interface induce interdimensional behaviour in the density of states at the location of the interface. The interdimensional behaviour in the presence of RSOC still exhibits interpolating behaviour from three-dimensional to two-dimensional for increasing energy. The inclusion of RSOC in the interface term of our interdimensional models in all cases results in the existence of bound state contributions to the density of states at the location of the interface. In all RSOC models the bound state wavenumbers depended on $k_{\|}$ explicitly. Spin-split contributions were only present in bound state solutions once we included an attractive potential term which did not depend on $k_{\|}$. In this model we were able to analyze the spin-split behaviour of the density of states and particle density, as well as an enhancement of the Edelstein effect. In both the attractive potential and effective mass models with RSOC, the bound state and free state density of states are connected. The vanishing of a bound state contribution to the density of states corresponds to a van Hove type singularity in the free state density of states. This interdimensional behaviour is expected to be observable in heterostructure materials in the field of spintronics, specifically Rashba interface systems and surfaces of topological crystalline insulators. A clear extension of our research is the inclusion of spin-orbit coupling into the quasirelativistic fermion model, and will be discussed in the following section.

## 5.2 Future research

Future research with interdimensional models will involve studying interdimensional effects in nonrelativistic and quasirelativistic fermionic systems in which terms responsible for spin-orbit coupling will be included. In the interdimensional nonrelativistic system this will be

accomplished by including kinetic terms which are linear in derivatives in the interface term of the interdimensional Hamiltonian. This is motivated by a Rashba term in which perpendicular fields penetrate the interface [25, 64]. The dispersion relation of Graphene [43, 65] also serves as motivation for the inclusion of kinetic terms which are linear in derivatives. In the interdimensional quasirelativistic system we will include a spin-orbit coupling term [25],[66] in the interface term of the interdimensional Hamiltonian.

Inclusion of spin-orbit coupling in the fermionic systems is motivated by the recent discovery of the so-called topological Dirac semimetals – a natural three-dimensional counterpart of graphene with spin-orbit coupling – such as $Na_3Bi$ [67] and $Cd_3As_2$ [68], in which the conduction and valence bands touch only at discrete Dirac points and disperse linearly along all momentum directions. While the Dirac points in graphene are gapped out by spin-orbit coupling, the Dirac cones in these materials are protected by symmetry and reduced to Weyl nodes that can host massless chiral Weyl fermions as low-energy excitation. It has been found very recently that the highly stable, non-toxic material ZrSiS presents such Dirac and Weyl physics, with the energy range of linear dispersion up to 2 eV [69]. Studying Dirac and Weyl semimetals – in particular, their quasi-relativistic behaviour and surface/interface states – is significant not only from the fundamental point of view, but also for technological applications owing to extremely high mobility and large magnetoresistance.

In both the nonrelativistic and quasirelativistic systems we will work to calculate the Green function and density of states inside the interface. This will provide analytic results which are of importance to the field of condensed matter physics in which materials exhibit technologically useful behavior due to spin-orbit interactions.

# References


[1] M.Z. Hasan and C.L. Kane. Colloquium: Topological insulators. *Rev. Mod. Phys.*, 82:3045–3065, 2010.

[2] K.S. Novoselov et al. Two-dimensional gas of massless Dirac fermions in graphene. *Nature*, 438:197–200, 2005.

[3] B.A. Bernevig, T.L. Huges, and S.C. Zhang. Quantum spin Hall effect and topological phase transition in HgTe quantum wells. *Science*, 314:1757–1761, 2006.

[4] L. Fu, C.L. Kane, and E.J. Mele. Topological insulators in three dimensions. *Phys. Rev. Lett.*, 98:106803, 2007.

[5] J.E. Moore and L. Balents. Topological invariants of time-reversal-invariant band structures. *Phys. Rev. B*, 75:121306, 2007.

[6] R. Roy. Topological phases and the quantum spin Hall effect in three dimensions. *Phys. Rev. B*, 79:195322, 2009.

[7] D. Hsieh et al. A topological Dirac insulator in a quantum spin Hall phase. *Nature*, 452:970–974, 2008.

[8] L. Fu. Topological crystalline insulators. *Phys. Rev. Lett.*, 106:106802, 2011.

[9] T.H. Hsieh et al. Topological crystalline insulators in the SnTe material class. *Natt. Commun.*, 3:982, 2012.

[10] A. Svane et al. Quasiparticle self-consistent gw calculations for PbS, PbSe, and PbTe: Band structure and pressure coefficients. *Phys. Rev. B*, 81:245120, 2010.

[11] T. Liang et al. Evidence for massive bulk Dirac fermions in $Pb_{1-x}Sn_xSe$ from nernst and thermopower experiments. *Natt. Commun.*, 4:2696, 2013.

[12] C. Yan et al. Experimental observation of Dirac-like surface states and topological phase transition in $Pb_{1-x}Sn_xTe(111)$ films. *Phys. Rev. Lett.*, 112:186801, 2014.

[13] M. Sato and Y. Ando. Topological superconductors: a review. *Rep. Prog. Phys.*, 80:076501, 2017.

[14] I. Zeljkovic et al. Dirac mass generation from crystal symmetry breaking on the surfaces of topological crystalline insulators. *Nat. Mat.*, 14:318–324, 2015.

[15] C.M. Polley et al. Observation of topological crystalline insulator surface states on (111)-oriented $Pb_{1-x}Sn_xSe$ films. *Phys. Rev. B*, 89:075317, 2014.

[16] B.M. Wojek et al. Direct observation and temperature control of the surface Dirac gap in a topological crystalline insulator. *Nat. Comm.*, 6:9463, 2015.

[17] M. Neupane et al. Topological phase diagram and saddle point singularity in a tunable topological crystalline insulator. *Phys. Rev. B*, 92:075131, 2015.

[18] I. Pletikosic, G.D. Gu, and T. Valla. Inducing a Lifshitz transition by extrinsic doping of suface bands in the topological crystalline insulator $Pb_{1-x}Sn_xSe$. *Phys. Rev. Lett.*, 112:146403, 2014.

[19] S.A. Wolf et al. Spintronics: A spin-based electronics vision for the future. *Science*, 294:1488, 2001.

[20] I. Zutic, J. Fabian, and S. Das Sarma. Spintronics: Fundamentals and applications. *Rev. Mod. Phys.*, 76:323, 2004.

[21] V.M. Edelstein. Spin polarization of conduction electrons induced by electric current in two-dimensional asymmetric electron systems. *Solid State Commun.*, 73:233, 1990.

[22] A. Soumyanarayanan, N. Reyren, A. Fert, and C. Panagopoulos. Emergent phenomena induced by spin-orbit coupling at surfaces and interfaces. *Nature*, 539:509, 2016.

[23] W. Han, Y.-C. Otani, and S. Maekawa. Quantum materials for spin and charge conversion. *npj Quantum Mat.*, 3:27, 2018.

[24] G. Dresselhaus. Spin-orbit coupling effects in Zinc blende structures. *Phys. Rev.*, 100:580, 1955.

[25] Y.A. Bychkov and E.I. Rashba. Properties of a 2d electron gas with lifted spectral degeneracy. *JETP Lett.*, 39:78, 1984.

[26] R. Dick. *Advanced Quantum Mechanics: Materials and Photons*. Springer, New York, 2012.

[27] R. Winkler. *Spin-Orbit Coupling Effects in Two-Dimensional Electron and Hole Systems*. Springer, Berlin, 2003.

[28] C. Kittel. *Introduction to solid state physics 8th edition*. John Wiley and Sons, Inc., New Jersey, 2005.

[29] A. Manchon, H.C. Koo, J. Nitta, S.M. Frolov, and R.A. Duine. New perspectives for Rashba spin-orbit coupling. *Nat. Mater.*, 14:871, 2015.

[30] H.J. Zhang et al. Charge-to-spin conversion and spin diffursion in Bi/Ag bilayers observed by spin-polarized positron beam. *Phys. Rev. Lett.*, 114:166602, 2015.

[31] W. Zhang, M.B. Jungfleisch, W. Jiang, J.E. Pearson, and A. Hoffmann. Spin pumping and inverse Rashba-Edelstein effect in NiFe/Ag/Bi and NiFe/Ag/Sb. *Appl. Phys.*, 117:17C727, 2015.

[32] M. Isasa et al. Origin of inverse Rashba-Edelstein effect detected at the Cu/Bi interface using lateral spin valves. *Phys. Rev. B*, 93:014420, 2016.

[33] A. Ohtomo and H.Y. Hwang. A high-mobility electron gas at the $LaAlO_3/SrTiO_3$ heterointerface. *Nature*, 427:423, 2004.

[34] H.Y. Hwang et al. Emergent phenomena at oxide interfaces. *Nat. Mater.*, 11:103, 2012.

[35] J. Mannhart and D.G. Schlom. Oxide interfaces - An opportunity for electronics. *Science*, 327:1607, 2010.

[36] S. Okamoto and A.J. Millis. Electronic reconstruction at an interface between a Mott insulator and a band insulator. *Nature*, 428:630, 2004.

[37] S.A. Chambers. Understanding the mechanism of conductivity at the $LaAlO_3/SrTiO_3(001)$ interface. *Surf. Sci.*, 605:1133, 2011.

[38] G. Herranz et al. High mobility in $LaAlO_3/SrTiO_3$ heterostructures: Origin, dimensionality, and perspectives. *Phys. Rev. Lett.*, 98:216803, 2007.

[39] A.D. Caviglia, S. Garglio M. Gabay, N. Reyren, C. Cancellieri, and J.-M. Triscone. Tunable Rashba spin-orbit interaction at oxide interfaces. *Phys. Rev. Lett.*, 104:126803, 2010.

[40] X.-L. Qi and S.-C. Zhang. Topological insulators and superconductors. *Rev. Mod. Phys.*, 83:1057, 2011.

[41] S. Karube, K. Kondou, and Y. Otani. Experimental observation of spin-to-charge current conversion at non-magnetic metal/$Bi_2O_3$ interfaces. *Appl. Phys. Expr.*, 9:033001, 2016.

[42] J. Kim et al. Evaluation of bulk-interface contributions to Edelstein magnetoresistance at metal/oxide interfaces. *Phys. Rev. B*, 96:140409, 2017.

[43] G.W. Semenoff. Condensed-matter simulation of a three-dimensional anomaly. *Phys. Rev. Lett.*, 53:2449–2452, 1984.

[44] A. H. Castro Neto, F. Guinea, N. M. R. Peres, K.S. Novoselov, and A. K. Geim. The electronic properties of graphene. *Rev. Mod. Phys.*, 81:109, 2009.

[45] D. S. L. Abergel, V. Apalkov, J. Berashevich, K. Ziegler, and T. Chakraborty. Properties of graphene: A theoretical perspective. *Adv. Mat.*, 59:261, 2010.

[46] J.C. Rojas-Sánchez, L. Vila, G. Desfonds, S. Gambarelli, J.P. Attané, J.M. De Teresa, C. Magén, and A. Fert. Spin-to-charge conversion using rashba coupling at the interface between non-magnetic materials. *Nat. Commun.*, 4:3944, 2013.

[47] S. Zhang and A. Fert. Conversion between spin and charge currents with topological insulators. *Phys. Rev. B*, 94:184423, 2016.

[48] Q. Song et al. Observation of inverse Edelstein effect in Rashba-split 2DEG between $SrTiO_3$ and $LaAlO_3$ at room temperature. *Sci. Adv.*, 3:e1602312, 2017.

[49] E. Lesne et al. Highly efficient and tunable spin-to-charge conversion through Rashba coupling at oxide interfaces. *Nat. Mater.*, 15:014420, 2016.

[50] Y. Wang et al. Room-temperature giant spin-to-charge conversion at the $SrTiO_3$-$LaAlO_3$ oxide interface. *Nano. Lett.*, 17:7659, 2017.

[51] J.B.S. Mendes et al. Spin-current to charge-current conversion and magnetoresistance in a hybrid structure of graphene and yttrium iron garnet. *Phys. Rev. Lett.*, 115.

[52] S. Dushenko et al. Gate-tunable spin-charge conversion and the role of spin-orbit interaction in graphene. *Phys. Rev. Lett.*, 116:166102, 2016.

[53] D. Xiao, G.-B. Liu, W. Feng, X. Xu, and W. Yao. Coupled spin and valley physics in monolayers of $MoS_2$ and other group-VI dichalcogenides. *Phys. Rev. Lett.*, 108:196802, 2012.

[54] M. He, H. Sun, and Q.-L. He. Topological insulator: Spintronics and quantum computations. *Front. Phys.*, 14:43401, 2019.

[55] K. Kondou et al. Fermi-level-dependent charge-to-spin conversion by Dirac surface states of topological insulators. *Nat. Phys.*, 12:1027, 2016.

[56] Y. Wang et al. Topological surface states originated spin-orbit torques in $Bi_2Se_3$. *Phys. Rev. Lett.*, 114:257202, 2015.

[57] J.C. Rojas-Sánchez et al. Spin to charge conversion at room temperature by spin pumping into a new type of topological insulator: $\alpha$-sn films. *Phys. Rev. Lett.*, 116:096602, 2016.

[58] R. Dick. Dimensional effects on densities of states and interactions in nanostructures. *Nanoscale Res. Lett.*, 5:1546–1554, 2010.

[59] R. Dick. Inter-dimensional effects in nano-structures. *Nanoscale Res. Lett.*, 7:581, 2012.

[60] M. Abramowitz and I.A. Stegun. *Handbook of Mathematical Functions*. Wiley, New York, tenth edition, 1972.

[61] A.C. Zulkoskey, R. Dick, and K. Tanaka. Interdimensional effects in systems with quasirelativistic dispersion relations. *Phys. Rev. A*, 89:052103, 2014.

[62] L. Van Hove. The occurence of singularities in the elastic frequency distribution of a crystal. *Phys. Rev.*, 89:1189, 1953.

[63] P. D. C. King et al. Large tunable Rashba spin splitting of a two-dimensional electron gas in $Bi_2Se_3$. *Phys. Rev. Lett.*, 107:096802, 2011.

[64] S.S. Li and J.B. Xia. Linear rashba model of a hydrogenic donor impurity in gaas/gaalas quantum wells. *Nanoscale Res. Lett.*, 2009:178, 4.

[65] T. Li and Z. Zhang. Snap-through instability of graphene on substrates. *Nanoscale Res. Lett.*, 5:169, 2010.

[66] A. Manchon et. al. New perspectives for Rashba spin-orbit coupling. *Nat. Mat.*, 14:871, 2015.

[67] Z.K. Liu et al. Discovery of a three-dimensional topological Dirac semimetal, $Na_3Bi$. 343:864, 2014.

[68] M. Neupane et al. Observation of a three-dimensional topological Dirac semimetal phase in high-mobility $Cd_3As_2$. *Nat. Comm.*, 5:3786, 2014.

[69] L.M. Schoop et al. Dirac cone protected by non-symmorphic symmetry and three-dimensional Dirac line node in zrsis. *Nat. Comm.*, 7:11696, 2016.

# Appendix A

# Derivation of energy dependent Green function in $\boldsymbol{x}$ representation in the form of a Hankel transform in RSOC systems

The Green function equation corresponding to Eqs. (3.8, 3.21, 3.31) can be concisely written as

$$\left[\frac{2mE}{\hbar^2} + \boldsymbol{\nabla}^2 + \delta(z - z_0)\overset{\leftrightarrow}{N}(\partial_x, \partial_y, \sigma_x, \sigma_y)\right]\langle \boldsymbol{x}|G(E)|\boldsymbol{x'}\rangle = -\delta^3(\boldsymbol{x} - \boldsymbol{x'}), \tag{A.1}$$

where $\overset{\leftrightarrow}{N}$ represents the particular interface matrix present in Eqs. (3.8, 3.21, 3.31) respectively. Substitution of the Fourier transform,

$$\langle \boldsymbol{x}_\parallel, z|G(E)|\boldsymbol{x}'_\parallel, z'\rangle = \frac{1}{4\pi^2}\int d^2\boldsymbol{k}_\parallel \int d^2\boldsymbol{k}'_\parallel \exp[i(\boldsymbol{k}_\parallel \cdot \boldsymbol{x}_\parallel - \boldsymbol{k}'_\parallel \cdot \boldsymbol{x}'_\parallel)]\langle \boldsymbol{k}_\parallel, z|G(E)|\boldsymbol{k}'_\parallel, z'\rangle, \tag{A.2}$$

into Eq. (A.1) yields

$$\begin{aligned}\left[\frac{2mE}{\hbar^2} - \boldsymbol{k}_\parallel^2 + \partial_z^2 - \delta(z - z_0)\overset{\leftrightarrow}{N}(k_x, k_y, \sigma_x, \sigma_y)\right]\langle \boldsymbol{k}_\parallel, z|G(E)|\boldsymbol{k}'_\parallel, z'\rangle \\ = -\delta^2(\boldsymbol{k}_\parallel - \boldsymbol{k}'_\parallel)\delta(z - z')\overset{\leftrightarrow}{1}.\end{aligned} \tag{A.3}$$

Insertion of Eq. (**??**) into Eq. (A.3) yields the condition,

$$\begin{aligned}\left[\frac{2mE}{\hbar^2} - \boldsymbol{k}_\parallel^2 + \partial_z^2 - \delta(z - z_0)\overset{\leftrightarrow}{N}(k_x, k_y, \sigma_x, \sigma_y)\right]\langle z|G(E, \boldsymbol{k}_\parallel)|z'\rangle \\ = -\delta(z - z')\overset{\leftrightarrow}{1}.\end{aligned} \tag{A.4}$$

Fourier transformation with respect to $z$ yields

$$\begin{aligned}&\left(\frac{2mE}{\hbar^2} - \boldsymbol{k}_\parallel^2 - k_\perp^2\right)\langle k_\perp|G(E, \boldsymbol{k}_\parallel)|z'\rangle \\ &- \frac{1}{2\pi}\overset{\leftrightarrow}{N}(k_x, k_y, \sigma_x, \sigma_y)\int d\kappa_\perp \exp[iz_0(\kappa_\perp - k_\perp)]\langle \kappa_\perp|G(E, \boldsymbol{k}_\parallel)|z'\rangle \\ &= -\frac{1}{\sqrt{2\pi}}\exp(-ik_\perp z').\end{aligned} \tag{A.5}$$

Equation (A.5) implies that $\langle k_\perp|G(E,\boldsymbol{k}_\parallel)|z'\rangle$ has the form,

$$\exp(ik_\perp z_0)\langle k_\perp|G(E,\boldsymbol{k}_\parallel)|z'\rangle = \frac{\exp[ik_\perp(z_0-z')]/\sqrt{2\pi}+f(E,\boldsymbol{k}_\parallel,z')}{\boldsymbol{k}_\parallel^2+k_\perp^2-(2mE)/\hbar^2}, \tag{A.6}$$

with the condition that the function $f(E,\boldsymbol{k}_\parallel,z')$ satisfies

$$\begin{aligned} &f(E,\boldsymbol{k}_\parallel,z')+\overleftrightarrow{N}(k_x,k_y,\sigma_x,\sigma_y)\\ &\times\int\frac{d\kappa_\perp}{2\pi}\frac{\exp[i\kappa_\perp(z_0-z')]/\sqrt{2\pi}+f(E,\boldsymbol{k}_\parallel,z')}{\boldsymbol{k}_\parallel^2+\kappa_\perp^2-(2mE)/\hbar^2}=0. \end{aligned} \tag{A.7}$$

The $\kappa_\perp$ integral in Eq. (A.7) is solved using the residue theorem. Recognizing that the denominator contains four simple poles yields

$$\begin{aligned} \int\frac{d\kappa_\perp}{2\pi}\frac{\exp(i\kappa_\perp z)}{\boldsymbol{k}_\parallel^2+\kappa_\perp^2-(2mE)/\hbar^2-i\epsilon} &= i\hbar\frac{\Theta(2mE-\hbar^2\boldsymbol{k}_\parallel^2)}{2\sqrt{2mE-\hbar^2\boldsymbol{k}_\parallel^2}}\exp\Big(i\sqrt{2mE-\hbar^2\boldsymbol{k}_\parallel^2}|z|/\hbar\Big)\\ +\hbar\frac{\Theta(\hbar^2\boldsymbol{k}_\parallel^2-2mE)}{2\sqrt{\hbar^2\boldsymbol{k}_\parallel^2-2mE}}&\exp\Big(-\sqrt{\hbar^2\boldsymbol{k}_\parallel^2-2mE}|z|/\hbar\Big). \end{aligned} \tag{A.8}$$

For brevity, we introduce the substitutions $\gamma=2mE-\hbar^2\boldsymbol{k}_\parallel^2$, $\beta=\hbar^2\boldsymbol{k}_\parallel^2-2mE$, $A=\frac{i\hbar\Theta(\gamma)}{2\sqrt{\gamma}}$ and $B=\frac{\hbar\Theta(\beta)}{2\sqrt{\beta}}$. Making use of these substitutions for the condition on $f(E,\boldsymbol{k}_\parallel,z')$ yields

$$\begin{aligned} \overleftrightarrow{M}\cdot f(E,\boldsymbol{k}_\parallel,z') = -\frac{\overleftrightarrow{N}(k_x,k_y,\sigma_x,\sigma_y)}{\sqrt{2\pi}}\Bigg[&A\exp\Big(i\sqrt{\gamma}|z'-z_0|/\hbar\Big)\\ &+B\exp\Big(-\sqrt{\beta}|z'-z_0|/\hbar\Big)\Bigg], \end{aligned} \tag{A.9}$$

where

$$\overleftrightarrow{M}=\overleftrightarrow{1}+\overleftrightarrow{N}(k_x,k_y,\sigma_x,\sigma_y)(A+B). \tag{A.10}$$

Solving Eq. (A.9) for $f(E,\boldsymbol{k}_\parallel,z')$ yields

$$\begin{aligned} f(E,\boldsymbol{k}_\parallel,z') = &\overleftrightarrow{M}^{-1}\cdot\overleftrightarrow{N}(k_x,k_y,\sigma_x,\sigma_y)\\ &\times\left(\frac{-1}{\sqrt{2\pi}}\right)\Big(A\exp(i\sqrt{\gamma}|z'-z_0|/\hbar)+B\exp(-\sqrt{\beta}|z'-z_0|/\hbar)\Big). \end{aligned} \tag{A.11}$$

In order to Fourier transform Eq. (A.6) with respect to $k_\perp$ it is useful to factor out $1/\sqrt{2\pi}$ from $f(E,\boldsymbol{k}_\parallel,z')$. Therefore we redefine $f(E,\boldsymbol{k}_\parallel,z')$ as

$$f(E,\boldsymbol{k}_\parallel,z')=\frac{1}{\sqrt{2\pi}}Q(E,\boldsymbol{k}_\parallel,z').$$

The Fourier transformation of Eq. (A.6) with respect to $k_\perp$ yields

$$\begin{aligned}\langle z|G(E,\boldsymbol{k}_\parallel)|z'\rangle &= \int \frac{dk_\perp}{2\pi}\frac{\exp[ik_\perp(z-z')]+Q(E,\boldsymbol{k}_\parallel,z')\exp[ik_\perp(z-z_0)]}{\boldsymbol{k}_\parallel^2+k_\perp^2-(2mE)/\hbar^2-i\epsilon}\\ &= A\exp\left(i\sqrt{\gamma}|z-z'|/\hbar\right)+B\exp\left(-\sqrt{\beta}|z-z'|/\hbar\right)\\ &+\left[A\exp\left(i\sqrt{\gamma}|z-z_0|/\hbar\right)+B\exp\left(-\sqrt{\beta}|z-z_0|/\hbar\right)\right]Q(E,\boldsymbol{k}_\parallel,z').\end{aligned} \tag{A.12}$$

# Appendix B

# Approximate analytic solution to $k_{\|}(E)$ in Eq. (4.29)

In order to find approximate analytic expressions for the zeros of

$$\begin{aligned} k_{\|}^4 - \frac{2\eta}{\ell}k_{\|}^3 - \frac{1-\eta^2}{\ell^2}k_{\|}^2 + \frac{2mE}{\hbar^2\ell^2} &= 0 \\ \ell^4 k_{\|}^4 - 2\eta\ell^3 k_{\|}^3 - (1-\eta^2)\ell^2 k_{\|}^2 + g(E,\ell) &= 0, \end{aligned} \tag{B.1}$$

we can iteratively solve Eq. (B.1) numerically for $g(E,\ell) = 2mE\ell^2/\hbar^2 \in [0,\eta^2]$. The restriction for the range of values of $g(E,\ell)$ comes from the permissible range of values for $k_{\|}$ which preserves $\kappa \geq 0$. Using values of $\eta = m\alpha L_{\perp}/\hbar^2 = 0.2$ (which corresponds to $\alpha = 0.5 \times 10^{-11}\text{eV}\cdot\text{m}$, $L_{\perp} = 3\text{nm}$) and $\ell = 40\text{nm}$ yields $g(E,\ell) \in [0, 0.04]$. The numerical solutions for $k_{\|}$ show that Eq. (B.1) can be decomposed according to

$$(k_{\|} + (B-\xi))(k_{\|} + (A+\epsilon))(k_{\|} - (A-\epsilon))(k_{\|} - (B+\xi)) = 0, \tag{B.2}$$

where $A, B, \epsilon$ and $\xi$ are functions of $E, \eta$ and $\ell$ respectively. Expanding Eq. (B.2) yields

$$\begin{aligned} &k_{\|}^4 + 2(\epsilon-\xi)k_{\|}^3 - [(A^2-\epsilon^2) + 4\epsilon\xi + (B^2-\xi^2)]k_{\|}^2 \\ &+ 2k_{\|}[\xi(A^2-\epsilon^2) - \epsilon(B^2-\xi^2)] + (B^2-\xi^2)(A^2-\epsilon^2) = 0. \end{aligned} \tag{B.3}$$

Equating coefficients between Eqs. (B.1,B.3) yields the following system of equations:

$$\xi - \epsilon = \frac{\eta}{\ell}, \tag{B.4}$$

$$(A^2-\epsilon^2) + 4\epsilon\xi + (B^2-\xi^2) = \frac{1-\eta^2}{\ell^2}, \tag{B.5}$$

$$\xi(A^2-\epsilon^2) - \epsilon(B^2-\xi^2) = 0, \tag{B.6}$$

$$(B^2-\xi^2)(A^2-\epsilon^2) = \frac{g(E,\ell)}{\ell^4}. \tag{B.7}$$

Using Eqs. (B.6,B.7) yields

$$A(\epsilon,\xi) = \pm\sqrt{\epsilon^2 \pm \sqrt{\frac{\epsilon g(E,\ell)}{\xi\ell^4}}}, \tag{B.8}$$

$$B(\epsilon,\xi) = \pm\sqrt{\xi^2 \pm \sqrt{\frac{\xi g(E,\ell)}{\epsilon\ell^4}}}. \tag{B.9}$$

Calculating numerical values for $\epsilon, \xi$ for a given value of $g(E,\ell)$ in the numerical solutions shows us that the positive sign inside the square root must be chosen. Using Eqs. (B.8,B.9) in Eq. (B.5) yields

$$\sqrt{\frac{g(E,\ell)}{\ell^4}}\left(\sqrt{\frac{\epsilon}{\xi}}+\sqrt{\frac{\xi}{\epsilon}}\right)+4\epsilon\xi=\frac{1-\eta^2}{\ell^2}. \tag{B.10}$$

Using numerical values for $\epsilon, \xi$ for a given value of $g(E,\ell)$ shows that to a good approximation, the $4\epsilon\xi$ term in Eq. (B.10) can be neglected. Using the substitution $y^2=\epsilon$ yields

$$\sqrt{\frac{g(E,\ell)}{\xi\ell^4}}y^2-\frac{1-\eta^2}{\ell^2}y+\sqrt{\frac{g(E,\ell)\xi}{\ell^4}}=0. \tag{B.11}$$

Solving for $y$ and using $\epsilon=y^2$ yields

$$\epsilon_\pm=\frac{\xi\ell^4}{4g(E,\ell)}\left[\frac{1-\eta^2}{\ell^2}\pm\sqrt{\frac{(1-\eta^2)^2}{\ell^4}-\frac{4g(E,\ell)}{\ell^4}}\right]^2. \tag{B.12}$$

Using numerical values in Eq. (B.12) shows that the negative sign in the $\pm$ term should be chosen. Simplifying Eq. (B.12) and using Eq. (B.4) yields

$$\epsilon=\frac{(\eta/\ell)H(\eta,g(E,\ell))}{1-H(\eta,g(E,\ell))},\quad \xi=\frac{(\eta/\ell)}{1-H(\eta,g(E,\ell))}, \tag{B.13}$$

where $H(\eta,g(E,\ell))=(1/4g(E,\ell))[(1-\eta^2)-\sqrt{(1-\eta^2)^2-4g(E,\ell)}]^2$. Inserting the expressions for $\epsilon,\xi$ in Eq. (B.13) into Eqs. (B.8,B.9) yields approximate analytic solutions to the functions $A, B, \epsilon$ and $\xi$,

$$A=\sqrt{\left[\frac{1-\eta^2-\sqrt{(1-\eta^2)^2-4g(E,\ell)}}{2\ell^2}\right]\left[1+\frac{\eta^2}{2}\frac{1-\eta^2-\sqrt{(1-\eta^2)^2-4g(E,\ell)}}{(1-\eta^2)^2-4g(E,\ell)}\right]}, \tag{B.14}$$

$$B=\sqrt{\left[\frac{2g(E,\ell)}{\ell^2[1-\eta^2-\sqrt{(1-\eta^2)^2-4g(E,\ell)}]}\right]}\times\sqrt{\left[1+\frac{2g(E,\ell)\eta^2}{[(1-\eta^2)^2-4g(E,\ell)][1-\eta^2-\sqrt{(1-\eta^2)^2-4g(E,\ell)}]}\right]}, \tag{B.15}$$

$$\epsilon=\frac{\eta}{\ell}\frac{1-\eta^2-\sqrt{(1-\eta^2)^2-4g(E,\ell)}}{2\sqrt{(1-\eta^2)^2-4g(E,\ell)}}, \tag{B.16}$$

$$\xi = \frac{\eta}{\ell} \frac{2g(E,\ell)}{\sqrt{(1-\eta^2)^2 - 4g(E,\ell)}[1-\eta^2 - \sqrt{(1-\eta^2)^2 - 4g(E,\ell)}]}. \tag{B.17}$$

As an example of the accuracy in our approximate solutions to $A, B, \epsilon$ and $\xi$, for $g(E,\ell) = 0.04$ we have $A = 5.23 \times 10^{-3}\text{nm}^{-1}$ from Eq. (B.14) compared to $A = 5.26 \times 10^{-3}\text{nm}^{-1}$ from the numerical solutions. As previously stated, bound state solutions exist for $k_\parallel \in [0, \eta/\ell)$. Viewing the numerical data, the only solution which adheres to this range of values comes from $k_\parallel = A - \epsilon$. Therefore, we can use Eqs. (B.14,B.16) for $k_\parallel(E)$ in Eq. (4.25) and $k_{\parallel_i}$ in Eq. (4.28) to get approximate analytic solutions for the bound state density of states at the location of the interface.

# Appendix C

# Derivation of energy dependent Green function in $\boldsymbol{x}$ representation in the form of a Hankel transform for quasirelativistic fermion with effective mass system

Substituting the Fourier transform of the Green function matrix element into Eq. (3.35) yields

$$\begin{aligned}
&\left(\gamma^0 k^0 - \boldsymbol{\gamma}\cdot\boldsymbol{k} - \frac{mc}{\hbar}\right)\langle k^0, \boldsymbol{k}_\parallel, k_\perp|S|k'^0, \boldsymbol{k}'_\parallel, z'\rangle \\
+ \;& \frac{\ell}{2\pi}\int d\kappa_\perp \exp\left[iz_0\left(\kappa_\perp - k_\perp\right)\right]\left(-\boldsymbol{\gamma}_\parallel\cdot\boldsymbol{k}_\parallel - \frac{\Delta mc}{\hbar}\right)\langle k^0, \boldsymbol{k}_\parallel, \kappa_\perp|S|k'^0, \boldsymbol{k}'_\parallel, z'\rangle \\
= \;& -\delta^2(\boldsymbol{k}_\parallel - \boldsymbol{k}'_\parallel)\delta(k^0 - k'^0)\frac{\exp(-ik_\perp z')}{\sqrt{2\pi}}. \qquad \text{(C.1)}
\end{aligned}$$

Translational invariance of the Green function matrix element in the $\boldsymbol{x}_\parallel$ and $t$ directions implies

$$\langle k^0, \boldsymbol{k}_\parallel, k_\perp|S|k'^0, \boldsymbol{k}'_\parallel, z'\rangle = \langle k_\perp|S(k^0, \boldsymbol{k}_\parallel)|z'\rangle\delta^2(\boldsymbol{k}_\parallel - \boldsymbol{k}'_\parallel)\delta(k^0 - k'^0).$$

Applying translational invariance to the Fourier transformed Green function equation of motion yields

$$\begin{aligned}
&\left(\gamma^0 k^0 - \boldsymbol{\gamma}\cdot\boldsymbol{k} - \frac{mc}{\hbar}\right)\langle k_\perp|S(k^0, \boldsymbol{k}_\parallel)|z'\rangle \\
+ \;& \frac{\ell}{2\pi}\int d\kappa_\perp \exp\left[iz_0\left(\kappa_\perp - k_\perp\right)\right]\left(-\boldsymbol{\gamma}_\parallel\cdot\boldsymbol{k}_\parallel + \frac{\Delta mc}{\hbar}\right)\langle \kappa_\perp|S(k^0, \boldsymbol{k}_\parallel)|z'\rangle \\
= \;& -\frac{\exp(-ik_\perp z')}{\sqrt{2\pi}}. \qquad \text{(C.2)}
\end{aligned}$$

Multiplying both sides of this equation by $\exp(ik_\perp z_0)$ and rearranging the equation yields

$$\begin{aligned}
\exp(ik_\perp z_0)\langle k_\perp|S(k^0, \boldsymbol{k}_\parallel)|z'\rangle \;&=\; \frac{(mc/\hbar) - \gamma\cdot k}{k^2 + (mc/\hbar)^2 - i\epsilon} \\
&\times\; \left[\frac{\exp[ik_\perp(z_0 - z')]}{\sqrt{2\pi}} + f(k^0, \boldsymbol{k}_\parallel, z')\right], \qquad \text{(C.3)}
\end{aligned}$$

where $f(k^0, \boldsymbol{k}_\parallel, z')$ is given by

$$f(k^0, \boldsymbol{k}_\parallel, z') = -\frac{\ell}{2\pi}\int d\kappa_\perp \exp(i\kappa_\perp z_0)\left(\boldsymbol{\gamma}_\parallel\cdot\boldsymbol{k}_\parallel - \frac{\Delta mc}{\hbar}\right)\langle \kappa_\perp|S(k^0, \boldsymbol{k}_\parallel)|z'\rangle.$$

This implies that that function $f(k^0, \boldsymbol{k}_\parallel, z')$ must satisfy

$$\begin{aligned} f(k^0, \boldsymbol{k}_\parallel, z') \quad &+ \quad \frac{\ell}{2\pi} \int d\kappa_\perp \frac{\left(\boldsymbol{\gamma}_\parallel \cdot \boldsymbol{k}_\parallel + (\Delta mc/\hbar)\right)\left((mc/\hbar) - \gamma \cdot k\right)}{-(k^0)^2 + \boldsymbol{k}_\parallel^2 + \kappa_\perp^2 + (mc/\hbar)^2 - i\epsilon} \\ &\times \quad \left( \frac{\exp[i\kappa_\perp (z_0 - z')]}{\sqrt{2\pi}} + f(k^0, \boldsymbol{k}_\parallel, z') \right) = 0. \end{aligned} \tag{C.4}$$

We can solve the $\kappa_\perp$ integral using the residue theorem. Recognizing the four simple poles in the denominator of the integrand and using $g(\kappa_\perp) = \left(\boldsymbol{\gamma}_\parallel \cdot \boldsymbol{k}_\parallel + (\Delta mc/\hbar)\right)\left((mc/\hbar) - \gamma \cdot k\right)$ for brevity yields the result

$$\begin{aligned} \int \frac{d\kappa_\perp}{2\pi} \frac{\exp(i\kappa_\perp z) g(\kappa_\perp)}{-(k^0)^2 + \boldsymbol{k}_\parallel^2 + \kappa_\perp^2 + (mc/\hbar)^2 - i\epsilon} &= \frac{i\Theta\left[(k^0)^2 - \boldsymbol{k}_\parallel^2 - (mc/\hbar)^2\right]\Theta\left(z_0 - z'\right)}{2\sqrt{(k^0)^2 - \boldsymbol{k}_\parallel^2 - (mc/\hbar)^2}} \\ &\times g\left(\sqrt{\alpha}\right) \exp\left[i(z_0 - z')\sqrt{(k^0)^2 - \boldsymbol{k}_\parallel^2 - (mc/\hbar)^2}\right] \\ &+ \frac{i\Theta\left[(k^0)^2 - \boldsymbol{k}_\parallel^2 - (mc/\hbar)^2\right]\Theta\left(z' - z_0\right)}{2\sqrt{(k^0)^2 - \boldsymbol{k}_\parallel^2 - (mc/\hbar)^2}} \\ &\times g\left(-\sqrt{\alpha}\right) \exp\left[-i(z_0 - z')\sqrt{(k^0)^2 - \boldsymbol{k}_\parallel^2 - (mc/\hbar)^2}\right] \\ &+ \frac{\Theta\left[\boldsymbol{k}_\parallel^2 - (k^0)^2 + (mc/\hbar)^2\right]\Theta\left(z_0 - z'\right)}{2\sqrt{\boldsymbol{k}_\parallel^2 - (k^0)^2 + (mc/\hbar)^2}} \\ &\times g\left(i\sqrt{\beta}\right) \exp\left[-(z_0 - z')\sqrt{\boldsymbol{k}_\parallel^2 - (k^0)^2 + (mc/\hbar)^2}\right] \\ &+ \frac{\Theta\left[\boldsymbol{k}_\parallel^2 - (k^0)^2 + (mc/\hbar)^2\right]\Theta\left(z' - z_0\right)}{2\sqrt{\boldsymbol{k}_\parallel^2 - (k^0)^2 + (mc/\hbar)^2}} \\ &\times g\left(-i\sqrt{\beta}\right) \exp\left[(z_0 - z')\sqrt{\boldsymbol{k}_\parallel^2 - (k^0)^2 + (mc/\hbar)^2}\right], \end{aligned} \tag{C.5}$$

where $\alpha = (k^0)^2 - \boldsymbol{k}_\parallel^2 - (mc/\hbar)^2$ and $\beta = \boldsymbol{k}_\parallel^2 - (k^0)^2 + (mc/\hbar)^2$. Making use of the substitutions $A = \frac{i\ell\Theta(\alpha)\Theta(z_0 - z')}{2\sqrt{\alpha}}$, $B = \frac{i\ell\Theta(\alpha)\Theta(z' - z_0)}{2\sqrt{\alpha}}$, $C = \frac{\ell\Theta(\beta)\Theta(z_0 - z')}{2\sqrt{\beta}}$, $D = \frac{\ell\Theta(\beta)\Theta(z' - z_0)}{2\sqrt{\beta}}$, the condition that

$f(k^0, \boldsymbol{k}_\parallel, z')$ must satisfy takes the form

$$\begin{aligned}
\overleftrightarrow{M} \cdot f(k^0, \boldsymbol{k}_\parallel, z') = &- \left(\boldsymbol{\gamma}_\parallel \cdot \boldsymbol{k}_\parallel + \frac{\Delta mc}{\hbar}\right) \\
&\times \left[A\left(\frac{mc}{\hbar} + \gamma^0 k^0 - \boldsymbol{\gamma}_\parallel \cdot \boldsymbol{k}_\parallel - \gamma_\perp\sqrt{\alpha}\right)\frac{\exp[i\sqrt{\alpha}(z_0 - z')]}{\sqrt{2\pi}}\right. \\
&+ B\left(\frac{mc}{\hbar} + \gamma^0 k^0 - \boldsymbol{\gamma}_\parallel \cdot \boldsymbol{k}_\parallel + \gamma_\perp\sqrt{\alpha}\right)\frac{\exp[-i\sqrt{\alpha}(z_0 - z')]}{\sqrt{2\pi}} \\
&+ C\left(\frac{mc}{\hbar} + \gamma^0 k^0 - \boldsymbol{\gamma}_\parallel \cdot \boldsymbol{k}_\parallel - i\gamma_\perp\sqrt{\beta}\right)\frac{\exp[-\sqrt{\beta}(z_0 - z')]}{\sqrt{2\pi}} \\
&\left.+ D\left(\frac{mc}{\hbar} + \gamma^0 k^0 - \boldsymbol{\gamma}_\parallel \cdot \boldsymbol{k}_\parallel + i\gamma_\perp\sqrt{\beta}\right)\frac{\exp[\sqrt{\beta}(z_0 - z')]}{\sqrt{2\pi}}\right], \qquad \text{(C.6)}
\end{aligned}$$

where

$$\begin{aligned}
\overleftrightarrow{M} &= \overleftrightarrow{1} + \left(\boldsymbol{\gamma}_\parallel \cdot \boldsymbol{k}_\parallel + \frac{\Delta mc}{\hbar}\right) \\
&\times \left[A\left(\frac{mc}{\hbar} + \gamma^0 k^0 - \boldsymbol{\gamma}_\parallel \cdot \boldsymbol{k}_\parallel - \gamma_\perp\sqrt{\alpha}\right)\right. \\
&+ B\left(\frac{mc}{\hbar} + \gamma^0 k^0 - \boldsymbol{\gamma}_\parallel \cdot \boldsymbol{k}_\parallel + \gamma_\perp\sqrt{\alpha}\right) \\
&+ C\left(\frac{mc}{\hbar} + \gamma^0 k^0 - \boldsymbol{\gamma}_\parallel \cdot \boldsymbol{k}_\parallel - i\gamma_\perp\sqrt{\beta}\right) \\
&\left.+ D\left(\frac{mc}{\hbar} + \gamma^0 k^0 - \boldsymbol{\gamma}_\parallel \cdot \boldsymbol{k}_\parallel + i\gamma_\perp\sqrt{\beta}\right)\right]. \qquad \text{(C.7)}
\end{aligned}$$

In order to isolate Eq. (C.6) for $f(k^0, \boldsymbol{k}_\parallel, z')$, we must calculate $\overleftrightarrow{M}^{-1}$. Expanding out the gamma matrice products in $\overleftrightarrow{M}$ and collecting like terms using $\{\gamma^\mu, \gamma^\nu\} = -2\eta^{\mu\nu}$ yields

$$\begin{aligned}
\overleftrightarrow{M} &= \left[1 + (A + B + C + D)\left(\boldsymbol{k}_\parallel^2 + \frac{(m)(\Delta m)c^2}{\hbar^2}\right)\right]\overleftrightarrow{1} \\
&+ \left[\left(\frac{(m - \Delta m)c}{\hbar}\right)(A + B + C + D)\right](\boldsymbol{\gamma}_\parallel \cdot \boldsymbol{k}_\parallel) \\
&+ [A + B + C + D]\left(\boldsymbol{\gamma}_\parallel \cdot \boldsymbol{k}_\parallel + \frac{\Delta mc}{\hbar}\right)(\gamma^0 k^0) \\
&+ \left[(B - A)\sqrt{\alpha} + i\,(D - C)\sqrt{\beta}\right]\left(\boldsymbol{\gamma}_\parallel \cdot \boldsymbol{k}_\parallel + \frac{\Delta mc}{\hbar}\right)\gamma_\perp. \qquad \text{(C.8)}
\end{aligned}$$

Using the substitutions

$$E = \left[1 + (A + B + C + D)\left(\boldsymbol{k}_\parallel^2 + \frac{(m)(\Delta m)c^2}{\hbar^2}\right)\right],$$

$$F = \left[\left(\frac{(m-\Delta m)c}{\hbar}\right)(A+B+C+D)\right],$$

$$G = [A+B+C+D],$$

$$H = \left[(B-A)\sqrt{\alpha} + i\,(D-C)\sqrt{\beta}\right],$$

and recognizing that

$$\boldsymbol{\gamma}_{\parallel}\cdot\boldsymbol{k}_{\parallel} = \begin{pmatrix} 0 & 0 & 0 & (k_1-ik_2) \\ 0 & 0 & (k_1+ik_2) & 0 \\ 0 & (-k_1+ik_2) & 0 & 0 \\ (-k_1-ik_2) & 0 & 0 & 0 \end{pmatrix} \tag{C.9}$$

allows us to write $\overset{\leftrightarrow}{M}$ in the form

$$\overset{\leftrightarrow}{M} = \begin{pmatrix} E+G(k^0)(\Delta mc/\hbar) & H(k_1-ik_2) & H(\Delta mc/\hbar) & (k_1-ik_2)(F-G(k^0)) \\ -H(k_1+ik_2) & E+G(k^0)(\Delta mc/\hbar) & (k_1+ik_2)(F-G(k^0)) & -H(\Delta mc/\hbar) \\ -H(\Delta mc/\hbar) & (-k_1+ik_2)(F+G(k^0)) & E-G(k^0)(\Delta mc/\hbar) & H(k_1-ik_2) \\ (-k_1-ik_2)(F+G(k^0)) & H(\Delta mc/\hbar) & -H(k_1+ik_2) & E-G(k^0)(\Delta mc/\hbar) \end{pmatrix}. \tag{C.10}$$

In order to invert $\overset{\leftrightarrow}{M}$ we use the equation

$$\overset{\leftrightarrow}{M}^{-1} = \frac{1}{Det\overset{\leftrightarrow}{M}} Adj\overset{\leftrightarrow}{M},$$

where $Det\overset{\leftrightarrow}{M}$ is the determinant of $\overset{\leftrightarrow}{M}$, and $Adj\overset{\leftrightarrow}{M}$ is the adjugate matrix of $\overset{\leftrightarrow}{M}$. After computation we have

$$Det\overset{\leftrightarrow}{M} = \left[E^2 + F^2\boldsymbol{k}_{\parallel}^2 + \left(\boldsymbol{k}_{\parallel}^2 + (\Delta mc/\hbar)^2\right)\left(H^2 - G^2(k^0)^2\right)\right],$$

$$Adj\overset{\leftrightarrow}{M} = \begin{pmatrix} E-G(k^0)(\Delta mc/\hbar) & H(-k_1+ik_2) & -H(\Delta mc/\hbar) & (-k_1+ik_2)(F-G(k^0)) \\ H(k_1+ik_2) & E-G(k)(\Delta mc/\hbar) & -(k_1+ik_2)(F-G(k^0)) & H(\Delta mc/\hbar) \\ H(\Delta mc/\hbar) & (k_1-ik_2)(F+G(k^0)) & E+G(k^0)(\Delta mc/\hbar) & H(-k_1+ik_2) \\ (k_1+ik_2)(F+G(k^0)) & -H(\Delta mc/\hbar) & H(k_1+ik_2) & E+G(k^0)(\Delta mc/\hbar) \end{pmatrix}.$$

The matrix $\overset{\leftrightarrow}{M}^{-1}$ can be written more concisely as a product of gamma matrices, similar to Eq. (C.8). Writing $\overset{\leftrightarrow}{M}$ in this way yields

$$\begin{aligned} \overset{\leftrightarrow}{M}^{-1} = \quad & \frac{1}{\left[E^2+F^2\boldsymbol{k}_{\parallel}^2+\left(\boldsymbol{k}_{\parallel}^2+(\Delta mc/\hbar)^2\right)(H^2-G^2(k^0)^2)\right]}\Big[E\overset{\leftrightarrow}{1} - F\left(\boldsymbol{\gamma}_{\parallel}\cdot\boldsymbol{k}_{\parallel}\right) \\ & -G\left(\boldsymbol{\gamma}_{\parallel}\cdot\boldsymbol{k}_{\parallel}+(\Delta mc/\hbar)\right)(\gamma^0 k^0) - H\left(\boldsymbol{\gamma}_{\parallel}\cdot\boldsymbol{k}_{\parallel}+(\Delta mc/\hbar)\right)(\gamma_{\perp})\Big] \end{aligned} \tag{C.11}$$

Multiplying both sides of Eq. (C.6) on the left hand side by Eq. (C.11) yields our expression for $f(k^0, \boldsymbol{k}_\parallel, z')$. In particular we have

$$
\begin{aligned}
f(k^0, \boldsymbol{k}_\parallel, z') = & -\frac{1}{\sqrt{2\pi}} \overleftrightarrow{M}^{-1} \cdot \left(\boldsymbol{\gamma}_\parallel \cdot \boldsymbol{k}_\parallel + (\Delta mc/\hbar)\right) \\
& \times \Bigg[ A \left(\frac{mc}{\hbar} + \gamma^0 k^0 - \boldsymbol{\gamma}_\parallel \cdot \boldsymbol{k}_\parallel - \gamma_\perp \sqrt{\alpha}\right) \exp\left[i(z_0 - z')\sqrt{\alpha}\right] \\
& + B \left(\frac{mc}{\hbar} + \gamma^0 k^0 - \boldsymbol{\gamma}_\parallel \cdot \boldsymbol{k}_\parallel + \gamma_\perp \sqrt{\alpha}\right) \exp\left[-i(z_0 - z')\sqrt{\alpha}\right] \\
& + C \left(\frac{mc}{\hbar} + \gamma^0 k^0 - \boldsymbol{\gamma}_\parallel \cdot \boldsymbol{k}_\parallel - i\gamma_\perp \sqrt{\beta}\right) \exp\left[-(z_0 - z')\sqrt{\beta}\right] \\
& + D \left(\frac{mc}{\hbar} + \gamma^0 k^0 - \boldsymbol{\gamma}_\parallel \cdot \boldsymbol{k}_\parallel + i\gamma_\perp \sqrt{\beta}\right) \exp\left[(z_0 - z')\sqrt{\beta}\right] \Bigg]. \qquad \text{(C.12)}
\end{aligned}
$$

Evaluating the gamma matrix products and collecting like terms yields

$$
\begin{aligned}
f(k^0, \boldsymbol{k}_\parallel, z') &= -\frac{1}{\sqrt{2\pi}} \overleftrightarrow{M}^{-1} \cdot \Bigg[ J \overleftrightarrow{1} + K \left(\boldsymbol{\gamma}_\parallel \cdot \boldsymbol{k}_\parallel\right) + L \left(\boldsymbol{\gamma}_\parallel \cdot \boldsymbol{k}_\parallel + (\Delta mc/\hbar)\right) \left(\gamma^0 k^0\right) \\
&+ N \left(\boldsymbol{\gamma}_\parallel \cdot \boldsymbol{k}_\parallel + (\Delta mc/\hbar)\right) \gamma_\perp \Bigg], \qquad \text{(C.13)}
\end{aligned}
$$

where

$$
\begin{aligned}
J &= \Big[A \exp[i(z_0 - z')\sqrt{\alpha}] + B \exp[-i(z_0 - z')\sqrt{\alpha}] \\
&+ C \exp[-(z_0 - z')\sqrt{\beta}] + D \exp[(z_0 - z')\sqrt{\beta}]\Big] \Big[\boldsymbol{k}_\parallel^2 + ((m)(\Delta m)c^2)/\hbar^2\Big],
\end{aligned}
$$

$$
\begin{aligned}
K &= \Big[A \exp[i(z_0 - z')\sqrt{\alpha}] + B \exp[-i(z_0 - z')\sqrt{\alpha}] \\
&+ C \exp[-(z_0 - z')\sqrt{\beta}] + D \exp[(z_0 - z')\sqrt{\beta}]\Big] \Big[(m - \Delta m)c/\hbar\Big],
\end{aligned}
$$

$$
\begin{aligned}
N &= \Big[A \exp[i(z_0 - z')\sqrt{\alpha}] + B \exp[-i(z_0 - z')\sqrt{\alpha}] \\
&+ C \exp[-(z_0 - z')\sqrt{\beta}] + D \exp[(z_0 - z')\sqrt{\beta}]\Big],
\end{aligned}
$$

$$
\begin{aligned}
L &= \Big[\left(B \exp[-i(z_0 - z')\sqrt{\alpha}] - A \exp[i(z_0 - z')\sqrt{\alpha}]\right)\sqrt{\alpha} \\
&+ i\left(D \exp[-(z_0 - z')\sqrt{\beta}] - C \exp[(z_0 - z')\sqrt{\beta}]\right)\sqrt{\beta}\Big].
\end{aligned}
$$

Inserting our expression for $\overleftrightarrow{M}^{-1}$ yields

$$\begin{aligned} f(k^0, \boldsymbol{k}_\parallel, z') &= -\frac{1}{\sqrt{2\pi}\left[E^2 + F^2\boldsymbol{k}_\parallel^2 + \left(\boldsymbol{k}_\parallel^2 + (\Delta mc/\hbar)^2\right)\left(H^2 - G^2(k^0)^2\right)\right]} \\ &\times \left[E\overleftrightarrow{1} - F\left(\boldsymbol{\gamma}_\parallel \cdot \boldsymbol{k}_\parallel\right) - G\left(\boldsymbol{\gamma}_\parallel \cdot \boldsymbol{k}_\parallel + (\Delta mc/\hbar)\right)\left(\gamma^0 k^0\right)\right. \\ &- \left. H\left(\boldsymbol{\gamma}_\parallel \cdot \boldsymbol{k}_\parallel + (\Delta mc/\hbar)\right)(\gamma_\perp)\right] \\ &\cdot \left[J\overleftrightarrow{1} + K\left(\boldsymbol{\gamma}_\parallel \cdot \boldsymbol{k}_\parallel\right) + L\left(\boldsymbol{\gamma}_\parallel \cdot \boldsymbol{k}_\parallel + (\Delta mc/\hbar)\right)\left(\gamma^0 k^0\right)\right. \\ &+ \left. N\left(\boldsymbol{\gamma}_\parallel \cdot \boldsymbol{k}_\parallel + (\Delta mc/\hbar)\right)\gamma_\perp\right]. \end{aligned}$$

If we decompose $E$ into $E = 1 + E'$ where $E' = (A + B + C + D)\left(\boldsymbol{k}_\parallel^2 + \frac{(m)(\Delta m)c^2}{\hbar^2}\right)$ we can use the similar forms of $E'$ and $J$, $F$ and $K$, $G$ and $L$, $H$ and $L$ to allow for lots of cancellation by inspection in the product of gamma matrix terms in $f(k^0, \boldsymbol{k}_\parallel, z')$. As an example, because of the similar forms stated above, terms of the form $E'K$ and $JF$ can be seen to be equal immediately because we know that the $A$,$B$,$C$, and $D$ terms contain Heaviside functions that cause only terms of the form $A^2$, $B^2$,$C^2$ and $D^2$ after muliplication, up to an exponential term. Using this logic we have

$$\begin{aligned} f(k^0, \boldsymbol{k}_\parallel, z') &= -\frac{1}{\sqrt{2\pi}\left[E^2 + F^2\boldsymbol{k}_\parallel^2 + \left(\boldsymbol{k}_\parallel^2 + (\Delta mc/\hbar)^2\right)\left(H^2 - G^2(k^0)^2\right)\right]} \\ &\times \left[J\overleftrightarrow{1} + K\left(\boldsymbol{\gamma}_\parallel \cdot \boldsymbol{k}_\parallel\right) + L\left(\boldsymbol{\gamma}_\parallel \cdot \boldsymbol{k}_\parallel + (\Delta mc/\hbar)\right)\left(\gamma^0 k^0\right)\right. \\ &+ \left. N\left(\boldsymbol{\gamma}_\parallel \cdot \boldsymbol{k}_\parallel + (\Delta mc/\hbar)\right)\gamma_\perp\right]. \end{aligned}$$

Evaluating the determinant of $\overleftrightarrow{M}$ in terms of $A$,$B$,$C$ and $D$ yields

$$\begin{aligned} f(k^0, \boldsymbol{k}_\parallel, z') &= -\frac{1}{\sqrt{2\pi}\left[1 + 2\left(\boldsymbol{k}_\parallel^2 + \frac{(m)(\Delta m)c^2}{\hbar^2}\right)(A + B + C + D)\right]} \\ &\times \left[J\overleftrightarrow{1} + K\left(\boldsymbol{\gamma}_\parallel \cdot \boldsymbol{k}_\parallel\right) + L\left(\boldsymbol{\gamma}_\parallel \cdot \boldsymbol{k}_\parallel + (\Delta mc/\hbar)\right)\left(\gamma^0 k^0\right)\right. \\ &+ \left. N\left(\boldsymbol{\gamma}_\parallel \cdot \boldsymbol{k}_\parallel + (\Delta mc/\hbar)\right)\gamma_\perp\right]. \end{aligned}$$

Now that we have solved for $f(k^0, \boldsymbol{k}_\parallel, z')$ we can Fourier transform Eq. (C.3) with respect to $k_\perp$. In order to do this efficiently, it is useful to factor out $1/\sqrt{2\pi}$ from $f(k^0, \boldsymbol{k}_\parallel, z')$. Therefore we redefine $f(k^0, \boldsymbol{k}_\parallel, z')$ as

$$f(k^0, \boldsymbol{k}_\parallel, z') = \frac{1}{\sqrt{2\pi}} Q(k^0, \boldsymbol{k}_\parallel, z'),$$

and insert this expression into Eq. (C.3). Fourier transforming Eq. (C.3) with respect to $k_\perp$ yields

$$\begin{aligned}\langle z|S(k^0,\boldsymbol{k}_\parallel)|z'\rangle &= \frac{1}{\sqrt{2\pi}}\int dk_\perp \langle z|k_\perp\rangle\langle k_\perp|S(k^0,\boldsymbol{k}_\parallel)|z'\rangle \\ &= \frac{1}{2\pi}\int dk_\perp \frac{(mc/\hbar)-\gamma\cdot k}{\boldsymbol{k}_\parallel^2+k_\perp^2-(k^0)^2+(mc/\hbar)^2+i\epsilon} \\ &\times \Big[\exp\left[ik_\perp\left(z-z'\right)\right]+\exp\left[ik_\perp\left(z-z_0\right)\right]Q(k^0,\boldsymbol{k}_\parallel,z')\Big],\end{aligned}$$

We recognize that the $k_\perp$ integral can be solved using the residue theorem just as in Eq. (C.5). Therefore after solving the $k_\perp$ integral we have

$$\begin{aligned}\langle z|S(k^0,\boldsymbol{k}_\parallel)|z'\rangle &= \frac{i\Theta(\alpha)\Theta(z-z')}{2\sqrt{\alpha}}\exp\left[i\sqrt{\alpha}\left(z-z'\right)\right]\left((mc/\hbar)\overset{\leftrightarrow}{1}+\gamma^0k^0-\boldsymbol{\gamma}_\parallel\cdot\boldsymbol{k}_\parallel-\gamma_\perp\sqrt{\alpha}\right) \\ &+\frac{i\Theta(\alpha)\Theta(z'-z)}{2\sqrt{\alpha}}\exp\left[-i\sqrt{\alpha}\left(z-z'\right)\right]\left((mc/\hbar)\overset{\leftrightarrow}{1}+\gamma^0k^0-\boldsymbol{\gamma}_\parallel\cdot\boldsymbol{k}_\parallel+\gamma_\perp\sqrt{\alpha}\right) \\ &+\frac{\Theta(\beta)\Theta(z-z')}{2\sqrt{\beta}}\exp\left[-\sqrt{\beta}\left(z-z'\right)\right]\left((mc/\hbar)\overset{\leftrightarrow}{1}+\gamma^0k^0-\boldsymbol{\gamma}_\parallel\cdot\boldsymbol{k}_\parallel-i\gamma_\perp\sqrt{\beta}\right) \\ &+\frac{\Theta(\beta)\Theta(z'-z)}{2\sqrt{\beta}}\exp\left[\sqrt{\beta}\left(z-z'\right)\right]\left((mc/\hbar)\overset{\leftrightarrow}{1}+\gamma^0k^0-\boldsymbol{\gamma}_\parallel\cdot\boldsymbol{k}_\parallel+i\gamma_\perp\sqrt{\beta}\right) \\ &+\Bigg[\frac{i\Theta(\alpha)\Theta(z-z_0)}{2\sqrt{\alpha}}\exp\left[i\sqrt{\alpha}\left(z-z_0\right)\right]\left((mc/\hbar)\overset{\leftrightarrow}{1}+\gamma^0k^0-\boldsymbol{\gamma}_\parallel\cdot\boldsymbol{k}_\parallel-\gamma_\perp\sqrt{\alpha}\right) \\ &+\frac{i\Theta(\alpha)\Theta(z_0-z)}{2\sqrt{\alpha}}\exp\left[-i\sqrt{\alpha}\left(z-z_0\right)\right]\left((mc/\hbar)\overset{\leftrightarrow}{1}+\gamma^0k^0-\boldsymbol{\gamma}_\parallel\cdot\boldsymbol{k}_\parallel+\gamma_\perp\sqrt{\alpha}\right) \\ &+\frac{\Theta(\beta)\Theta(z-z_0)}{2\sqrt{\beta}}\exp\left[-\sqrt{\beta}\left(z-z_0\right)\right]\left((mc/\hbar)\overset{\leftrightarrow}{1}+\gamma^0k^0-\boldsymbol{\gamma}_\parallel\cdot\boldsymbol{k}_\parallel-i\gamma_\perp\sqrt{\beta}\right) \\ &+\frac{\Theta(\beta)\Theta(z_0-z)}{2\sqrt{\beta}}\exp\left[\sqrt{\beta}\left(z-z_0\right)\right]\left((mc/\hbar)\overset{\leftrightarrow}{1}+\gamma^0k^0-\boldsymbol{\gamma}_\parallel\cdot\boldsymbol{k}_\parallel+i\gamma_\perp\sqrt{\beta}\right)\Bigg] \\ &\times Q(k^0,\boldsymbol{k}_\parallel,z'). \qquad \text{(C.14)}\end{aligned}$$

At this point we set $z=z'=z_0$ because we are interested in calculating the interdimensional quasirelativistic density of states inside the interface at $z_0$. In order to make this substitution into Eq. (C.14), we need to discuss how the interface of thickness $\ell$ is situated at the point $z_0$. The interface itself is situated symmetrically about the point $z_0$, so that the upper edge of the interface is located at $z=z_0+\ell/2$, and the lower edge at $z=z_0-\ell/2$. The small, but nonzero interface thickness requires us to use an analytic approximation to the Heaviside function as defined in [60]. This is accomplished through the use of a logistic function as an approximation for the Heaviside function. In general, the approximate form for the Heaviside function is given by

$$\Theta(x)\approx\frac{1}{1+e^{-2kx}}, \qquad \text{(C.15)}$$

where $k$ is a measure of the steepness of the logistic function as it goes from 1 to 0 about the point $x = 0$. Therefore, because the thickness of the interface is symmetrically placed about the point $z_0$, the steepness is given by $1/\ell$ and the approximate form for the Heaviside function is given by

$$\Theta(z - z') = \frac{1}{1 + e^{-2(z-z')/\ell}} \tag{C.16}$$

At $z = z' = z_0$, the Heaviside functions in Eq. (C.14) take the value 1/2. Recalling our definitions for $A, B, C$, and $D$ yields for $z = z' = z_0$

$$A = B = \frac{i\ell\Theta(\alpha)}{4\sqrt{\alpha}}, \tag{C.17}$$

$$C = D = \frac{\ell\Theta(\beta)}{4\sqrt{\beta}}. \tag{C.18}$$

Applying this to $Q(k^0, \boldsymbol{k}_\parallel, z')$ yields

$$\begin{aligned} Q(k^0, \boldsymbol{k}_\parallel, z') &= \frac{-1}{1 + \left(\frac{i\ell\Theta(\alpha)}{\sqrt{\alpha}} + \frac{\ell\Theta(\beta)}{\sqrt{\beta}}\right)\left(\boldsymbol{k}_\parallel^2 + (mc/\hbar)(\Delta mc/\hbar)\right)} \Bigg[ \left(\frac{i\ell\Theta(\alpha)}{2\sqrt{\alpha}} + \frac{\ell\Theta(\beta)}{2\sqrt{\beta}}\right) \\ &\times \Bigg( \left(\boldsymbol{k}_\parallel^2 + (mc/\hbar)(\Delta mc/\hbar)\right) \overset{\leftrightarrow}{1} + \left((mc/\hbar) - (\Delta mc/\hbar)\right)\left(\boldsymbol{\gamma}_\parallel \cdot \boldsymbol{k}_\parallel\right) \\ &+ \left(\boldsymbol{\gamma}_\parallel \cdot \boldsymbol{k}_\parallel + (\Delta mc/\hbar)\right)\left(\gamma^0 k^0\right) \Bigg) \Bigg] \end{aligned} \tag{C.19}$$

The relation between the interdimensional quasirelativistic density of states and the energy-dependent Green function matrix element is given by

$$\varrho(E) - \overline{\varrho}(\overline{E}) = \frac{E}{\pi\hbar mc^3} Tr\Big[\Im\langle \boldsymbol{x}|S(E)|\boldsymbol{x}\rangle\Big]. \tag{C.20}$$

Therefore, we only need to keep the terms in $\langle z_0|S(k^0, \boldsymbol{k}_\parallel)|z_0\rangle$ that are imaginary and have nonzero trace. The gamma matrices have the trace properties

$$Tr(\gamma^\mu) = 0, Tr(\gamma^\mu\gamma^\nu) = 4\eta^{\mu\nu} = 0, \mu \neq \nu, \tag{C.21}$$

implying that the only terms in Eq. (C.14) that survive are those that are imaginary and proportional to the identity matrix $\overset{\leftrightarrow}{1}$. Putting this all together yields

$$\begin{aligned} \langle z_0|S(k^0, \boldsymbol{k}_\parallel|z_0\rangle &= \frac{i\Theta(\alpha)}{2\sqrt{\alpha}}\Big(\frac{mc}{\hbar}\Big)\overset{\leftrightarrow}{1} + \frac{\ell\Theta(\alpha)}{4\alpha\left[1 + (i\Theta(\alpha)/\sqrt{\alpha})(\boldsymbol{k}_\parallel^2 + (mc/\hbar)(\Delta mc/\hbar))\right]} \\ &\times \left[\frac{mc}{\hbar}\left(\boldsymbol{k}_\parallel^2 + \left(\frac{mc}{\hbar}\right)\left(\frac{\Delta mc}{\hbar}\right)\right) + \boldsymbol{k}_\parallel^2\left(\frac{mc}{\hbar} - \frac{\Delta mc}{\hbar}\right)\right], \end{aligned} \tag{C.22}$$

$$Tr[\Im\langle z_0|S(k^0,\boldsymbol{k}_\parallel)|z_0\rangle] = \frac{\Theta(\alpha)}{2\sqrt{\alpha}\left(\alpha+\ell^2(\left(\boldsymbol{k}_\parallel^2+(mc/\hbar)(\Delta mc/\hbar)\right)^2\right)}\Bigg[4\alpha(mc/\hbar) + 2\ell^2(\Delta mc/\hbar)\left(\boldsymbol{k}_\parallel^2+(mc/\hbar)^2\right)\left(\boldsymbol{k}_\parallel^2+(mc/\hbar)(\Delta mc/\hbar)\right)\Bigg] \quad \text{(C.23)}$$

Inserting $\alpha = (k^0)^2 - \boldsymbol{k}_\parallel^2 - (mc/\hbar)^2$ and splitting $Tr[\Im\langle z_0|S(k^0,\boldsymbol{k}_\parallel)|z_0\rangle]$ into terms proportional to $(mc/\hbar)$ and terms proportional to the gap shift parameter $(\Delta mc/\hbar)$ yields

$$\begin{aligned} Tr[\Im\langle z_0|S(k^0,\boldsymbol{k}_\parallel)|z_0\rangle] = & \frac{\Theta((k^0)^2-\boldsymbol{k}_\parallel^2-(mc/\hbar)^2)}{(k^0)^2-\boldsymbol{k}_\parallel^2-(mc/\hbar)^2+\ell^2\left(\boldsymbol{k}_\parallel^2+(mc/\hbar)(\Delta mc/\hbar)\right)^2} \\ & \times\Bigg[2\left(\frac{mc}{\hbar}\right)\sqrt{(k^0)^2-\boldsymbol{k}_\parallel^2-(mc/\hbar)^2} \\ & + \frac{\ell^2(\Delta mc/\hbar)\left(\boldsymbol{k}_\parallel^2+(mc/\hbar)^2\right)\left(\boldsymbol{k}_\parallel^2+(mc/\hbar)(\Delta mc/\hbar)\right)}{\sqrt{(k^0)^2-\boldsymbol{k}_\parallel^2-(mc/\hbar)^2}}\Bigg]. \end{aligned} \quad \text{(C.24)}$$